# UC Berkeley

## UC Berkeley Electronic Theses and Dissertations

**Title**

Heterogeneity in Drosophila Signaling Systems

**Permalink**

https://escholarship.org/uc/item/0t25p4rs

**Author**

Agarwal, Gautam

**Publication Date**

2009

Peer reviewed|Thesis/dissertation

Heterogeneity in *Drosophila* Signaling Systems

by

Gautam Agarwal


A dissertation submitted in partial satisfaction of the

requirements for the degree of

Doctor of Philosophy

in

Neuroscience

in the

Graduate Division

of the

University of California, Berkeley


Committee in charge:

Professor Ehud Y. Isacoff, Chair
Professor Kristin Scott
Professor Mu-ming Poo
Professor Michael Gastpar


Fall 2009

Abstract

Heterogeneity in *Drosophila* Signaling Systems

by

Gautam Agarwal

Doctor of Philosophy in Neuroscience

University of California, Berkeley

Professor Ehud Y. Isacoff, Chair

Many biological systems are composed of heterogeneous elements. This work analyzes the heterogeneities found in signaling systems within the *Drosophila* nervous system, focusing on the neuromuscular junction and the antennal lobe. The variations found within each system are used to understand some aspect of its organization.

At the *Drosophila* larval neuromuscular junction (NMJ), a motor neuron releases glutamate from many boutons onto the muscle it innervates. A post-synaptically localizing calcium sensor was developed to visualize the distribution of synaptic strength across boutons. While the $Ca^{2+}$ signals were uniform within a given connection (*i.e.*, bouton and postsynapse pair), they differed considerably among connections of an NMJ. A gradient of transmission strength was observed along axonal branches, from weak proximal connections to strong distal ones. Presynaptic imaging revealed a matching axonal gradient, with higher $Ca^{2+}$ influx and exocytosis at distal boutons. The results suggest that transmission strength is mainly determined presynaptically at the level of individual boutons, possibly by one or more factors existing in a gradient.

The antennal lobe (AL) is a structure that processes odors. It is partitioned into glomeruli, each of whose inputs detect unique chemical features. How specialized is the circuitry of each glomerulus to operate on its inputs? We utilize a methodology that allows a simultaneous, unbiased comparison of the functional organization of many glomeruli. We find that the glomerulus DA1, which is selectively activated by a single pheromone, is organized differently than glomeruli that are activated by many different odorants. In contrast to what is seen in other glomeruli, ipsilateral and contralateral stimuli elicit distinct spatial patterns of activity within DA1. DA1 experiences greater and more rapid inhibition than other glomeruli, allowing it to report slight inter-antennal delays in stimulus onset in a  winner-take-all  manner. We propose that DA1's specializations help the fly localize and orient with respect to pheromone sources. Our results show how homologous circuits reflect the unique contingencies of their inputs.

Together, these works show how the heterogeneity found within diverse systems can provide a basis for understanding their organization.

To my extended family

# Table of Contents

# Acknowledgments

As with its objects of study, this work is the product of specialized roles operating as part of an irreducible group. Each person involved contributed invaluably at some phase, from the inception, to the development, to the communication of the work. For the work on the neuromuscular junction, Giovanna Guerrero was responsible for the sensor development and signal interpretation that provided the direction for the data visualization and analysis I performed. For the Shaker channel work, several graduate students collected data over many years which I consolidated and performed initial analysis on. This was incorporated into a much larger scale analysis of Shaker channel motion, made possible by collaborations initiated by Medha Pathak. My experiences as part of these two projects shaped my approach when studying the specialization of the antennal lobe.

Udi has been very supportive in allowing me to pursue a project that is outside of his and the lab's expertise. Nonetheless, he has constantly provided very incisive feedback that has made my work much more structurally sound and meaningful. He encouraged me personally and scientifically to persevere when I had doubts about my project's success. His passion for diverse areas of biology and his ability to excite undergraduate classrooms about enzymes has never ceased to inspire me.

My labmates were always very friendly and helpful. They have offered invaluable advice to help me overcome many experimental hurdles. I have learned much from seeing their dedication and hard work, as well as their individual approaches to scientific research. My labmate Claire Wyart has given priceless personal perspectives on experimental design and communication of results.

My graduate program has been very effective at bringing together people interested in all aspects of the brain. It has also been a very wonderful social environment. Our program administrator, Kati Markowitz, has been very helpful and kind to me. I was fortunate to get to know and learn with colleagues who share common interests.

My parents have done everything to make sure my brother and I had every educational opportunity available to us. I surely would not be here without their constant support and sacrifice. I hope that one day I can be as nurturing as they have been. Seeing my little brother become my academic peer has been amazing.

Being a student at UC Berkeley has been endlessly enriching. Every week there are great lectures by scholars and every semester there are great classes by brilliant professors. It has been a privilege being able to attend an institution that is able to provide a world-class yet economical

education in so many departments. In light of its current economic bind, I sincerely hope it continues to provide affordable quality education to a diverse student body. My interactions with such gifted students from all walks has been an integral part of my education here.

For the last four years, I have lived in a graduate student cooperative house with 56 housemates. Through this house I have met graduate students from every department on campus. Cooking each other's meals, cleaning each other's dishes, and celebrating together, we have come to know each other very well. The house has fostered intimate collaborations at all levels, and I hope to continue its tradition when I leave it.

Living in the Bay Area, I have been fortunate to meet a diverse range of self-motivated, creative, talented, and idealistic people who create new realities. Some of these meetings have developed into very close friendships. Bonding with my friends over numerous nerdy late night conversations has been endlessly nourishing and formative. In this regard, I am particularly indebted to Joshua Sorkin and Clifford Anderson, two of my oldest Bay Area friends, who live every moment engaging the world with a playful, analytic, and undying curiosity. Finally, I am very lucky to have my girlfriend Daria. Her gentle, penetrating sincerity has unlocked new realms of experience within me. I look forward to our future journey.

# Preface

Scientific works are usually presented as linear chains of logical inference. Beneath this narrative is the personal, often accidental, flow of the investigators' experiences. What follows is the series of events that led to the works presented in my thesis.

## Joining the Isacoff Laboratory

I rotated in the Isacoff lab to continue a project I had started as an undergraduate in the labs of Dr. Nigel Atkinson and Dr. Thomas Knopfel. It was to design a fluorescent protein that could report the membrane potential of a cell. Once developed, this sensor would enable the simultaneous measurement of the activity of a genetically defined population of neurons. Analyzing and interpreting the structure of interactions within such neural networks may one day help us understand the mechanisms underlying cognition.

Our approach was to fuse a fluorescent protein (FP) with a voltage-sensitive potassium channel. A channel in this family has the ability to sense a change in the membrane potential and tranduce this change into a force that opens the channel. We reasoned that attaching an FP at a position near the voltage-sensing part of the channel would divert this opening force into a contortion of the FP, leading to a detectable change in fluorescence. Unfortunately, our constructs failed to transport to the plasma membrane, largely being retained intracellularly. These and other attempts have motivated a larger-scale hunt for viable constructs, leading to the use of screens and of other families of voltage-sensing proteins. Both of these approaches have generated constructs that traffic to the plasma membrane effectively, yet their responses are too small to be practically used for high-precision measurement of population activity. Future optimizations will undoubtedly alleviate this limitation.

My second rotation in Dr. Mu-ming Poo's laboratory exposed me to electrophysiology. Seeing the subtle fluctuations of electrical activity in a neuron was an exhilarating experience. Nonetheless, this technique would not allow me to witness activity simultaneously across a neural population. Furthermore, I realized the discomfort I felt with working with neurons that were harvested from animal systems.

This motivated me to join Dr. Dave Schaffer's laboratory, which focuses on neural stem cell research. I hoped to maintain an immortal colony of stem cells that could be harvested and induced to form neural networks in a dish when needed. However, I quickly learned the limitations of this idea. The degree to which neurons generated in the dish represent those generated within the animal is unclear. Furthermore, neural stem cells last only 50 generations,

necessitating further use of animals.

My most realistic option at this point was to work on the simplest animal I could find. Several graduate students in the Isacoff lab were using fluorescent calcium sensors to study the neuromuscular junction in the fruit fly. I proposed to Dr. Isacoff to extend this project to study synaptic activity in the central nervous system (CNS) of the fruit fly. I saw this as an opportunity to study the organization of brain circuits, with the possibility of analyzing population dynamics. He supported the idea and I joined the lab.

**Studies of the neuromuscular junction**

As I joined the lab, the neuromuscular junction (NMJ) was producing a lot of data. One curious feature was that while the response of a given synaptic connection within the NMJ was similar across stimulations, the responses of different synapses differed significantly from each other. The biological basis of this variability remained elusive. I decided to analyze this data set using Matlab, a computational analysis software that I had picked up as an undergraduate researcher in Dr. Zach Mainen's lab. My goal was to make maps of synaptic strength to allow us to directly visualize the variability that until now had been manually quantified by marking synapses of interest. Unfortunately, the images were too noisy (Appendix 2); averaging five stimulations was not sufficient to generate clean maps of activity.

This led us to design a protocol allowing the presentation of one hundred stimulations. To circumvent the problem of photobleaching of dye, we automated a system to illuminate the preparation only during stimulations, thus leaving it in the dark for the majority of an experiment and keeping the fluorescent reporter bright. However, the muscle would contract and shift over these longer recording sessions. To correct for this, algorithms were adapted to detect different strings of synapses within the image, and correct each string's drift from stimulation to stimulation. The result was a motionless average of 100 stimulations. The maps immediately revealed a striking spatial pattern that governed the organization of synaptic strength: synapses at the end of a string were stronger than those at the beginning, and the strength of interaction was constant within the boundary of each connection.

This phenomenon is presented in Chapter 1, and raises a host of questions that merit future study. What are the factors that govern this spatial organization? One interesting clue comes from the exceptions to the rule. In the few cases where strong synapses are seen in the middle of a string, they occur at a point where the axon abruptly turns. This supports the idea that synapse strength may correlate with a presynaptic structural element. Work by Dr. Robin Ball has since shown that stronger synapses contain loops of microtubules. Is the greater average strength of a synapse due

to greater or to more probable activation of single active zones? Dr. Einat Peled is addressing this question using a new generation of calcium sensor that can accurately report responses to single stimulations (Appendix 2). What is the function of this gradient given the relatively simple morphology and much larger spatial extent of its target muscle? Analogous gradients have been reported in evolutionarily distant creatures. At the same time, the gradient is known not to exist in certain muscles nearby to the one studied here. Perhaps sensitive measurement of the spread of contraction and force through the muscle upon activation, or the measurement of activity at strong and weak synapses in response to a range of physiologically relevant temporal patterns of stimulation, would lead to insight into this question.

My experiences with this project got me very excited to extend these techniques to the fly brain. In a network where the structure of cellular processes relates critically to network function, I was sure to find such spatial patterns of synaptic strength.

**Studies of the Shaker potassium channel**

I soon found myself doing analysis for another project regarding the mechanism by which the Shaker potassium channel opens in response to membrane depolarization. The lab had approached this question by tagging single residues on the surface of the channel with a fluorescent marker; when the channel opened, the environment of the dye molecule would shift, causing a change of fluorescence. Over the prior seven years, such data had been collected for many residues within the channel, and in parallel another lab had determined the crystal structure of the channel at angstrom resolution. By mapping our fluorescence data upon the structure of the channel, we hoped to develop a model of channel opening that would be consistent with the changes in fluorescence measured at single sites.

After the process of excavating data from boxes and old hard drives, I wrote scripts to pull out the relevant information from the files and encode these as colors within the PDB text files of channel structure. Much information was available from the data files: the amplitudes and time constants of channel opening (fast) and inactivation (slow), for the channel current, as well as the changes in fluorescence. Comparing the time constants of fluorescence change and current flow could theoretically reveal the temporal order in which residues moved during activation and inactivation. However, the activation was too fast to reliably resolve and the slow inactivation contained an unexplained variability: for certain residues, repeating the experiment in different cells revealed cases where the residue moved faster than the inactivation, and others where it moved slower. So the analysis was based exclusively on the amplitudes of fluorescence change, resulting in each site being characterized by four magnitudes of fast and slow opening and closing. What was clear was that residues within the voltage sensor moved the most. However,

we were unable to reconstruct channel motion, partially because the positive and negative changes in fluorescence could not be related to specific environmental changes. This motivated collaborations with theoreticians that were modeling the energetics of channel motion, the fluorescence data providing useful constraints upon the final model.

There were a few observations that remain unaccounted for. Sites closer to the outer surface of the channel tended to have positive changes in fluorescence, while those below often had negative changes. Furthermore, there was a strong correlation between changes associated with activation and inactivation, in sign as well as magnitude. It is unclear how to interpret these results. However, the latter observation suggests that inactivation may be an extension of activation. Alternatively, these observations may relate to a region-specific bias in the behavior of the dye used.

**Studies of the antennal lobe**

I returned to my goal of mapping synaptic variation in the fly CNS. I decided to do so within the antennal lobe, as it was the best-characterized region in terms of anatomy, genetics, and function. I planned on duplicating the methodology established to study single synapses at the NMJ. I expressed our synaptically localizing calcium reporter, Synapcam, in the output neurons of the antennal lobe. However, the sensor was unable to localize selectively at synapses, most likely because the signals that allowed synaptic localization at the glutamatergic neuromuscular junction were unrecognized by the cholinergic antennal lobe synapses. Furthermore, the response within the glomerulus was largely homogeneous in magnitude, possibly due to the sensor's sensitivity to non-synaptic, voltage-sensitive calcium currents. This led me to shift my focus away from synaptic variation within glomeruli (the information channels within the antennal lobe), to variability of excitation among glomeruli.

The best known calcium sensor used in the fly antennal lobe at the time was GCaMP. However, newer versions of GCaMP had been introduced in the meantime. I got a fly line expressing GCaMP 1.6 and made lines with cytosolic as well as membrane-bound GCaMP 2. Neither version of GCaMP2 improved signal quality. However, when the membrane-bound sensor was expressed at the NMJ by Dr. Einat Peled, she found it could detect single synaptic release events (Appendix 2). I used GCaMP 1.6, which surprisingly outperformed GCaMP 2 (partially due to the latter's apparent toxicity), unlike what had been reported in mammals. GCaMP 3, reported two weeks ago (Tian et al. *Nature Methods* Nov. 8, 2009), appears to vastly outperform GCaMP 1.6 in the antennal lobe.

I started analyzing spatial variations among glomeruli, which I simultaneously activated using

electrical stimulation. While there was no clear pattern among glomerular responses to single stimuli, comparing different types of stimulation (left vs. right antennal nerve, $1^{st}$ vs. $2^{nd}$ stimulus) appeared to reveal a gradient of response types, from lateral glomeruli to medial ones. While this was intriguing, it lacked a functional significance, both in terms of the identities of the glomeruli, as well as the meaning of the stimulation paradigms. Over a long time, I explored many types of perturbations that would disrupt the gradient or otherwise reveal interesting patterns upon analysis. This occurred until one year ago, when I attempted to consolidate my results into an outline of a manuscript (Appendix 4). Over the next year, through the input of Dr. Isacoff, my thesis committee, Dr. Claire Wyart, the conceptual approach revealed in reports by Dr. Rachel Wilson's lab, and preparation for the Keystone Symposium on Chemical Senses, this diffuse outline crystallized into the completely different product seen in Chapter 2.

My work in the antennal lobe has been a profound learning experience. When I started, I thought that as long as I developed a system that produced a large amount of data, interesting patterns would emerge with sufficient analysis. This did not turn out to be the case. The variability of the preparation, the limitations of signal measurement, and the lack of functional correlates all made it difficult to develop far-reaching conclusions. Thus as open-minded data analysis is critical for discovery, so is a clearly developed conceptual model that guides the dissection of the wonderfully complex systems that we study.

# Introduction

A brain performs many remarkable operations that rapidly orient its owner to accommodate a constantly changing and often ambiguous environment. Its sophisticated function is supported by an immensely complex network of interactions taking place within and across many layers of organization. A fundamental challenge in neuroscience is to understand how processes occurring at the small scale cooperate to generate larger scale phenomena: from molecules to neurons, from neurons to neural networks, and from neural networks to brains.

Specialization is a hallmark of complex systems. One manifestation of this principle in the brain is the differentiation of regions dedicated to performing different behavioral functions, generating sights, smells, memories, and decisions. All of these brain regions share chemical, cellular, and circuit elements, which support a common language that facilitates rapid communication among regions. At the same time, the particular configuration of elements is unique to each region, enabling it to efficiently perform its specific function. How any brain region performs a task remains mysterious. This is because every task simultaneously activates many densely interacting neural elements, confounding attempts to reduce the system to its subcomponents. Mapping the specializations within a system provides a mechanism for assigning functions to specific system elements, within the context of the much larger set of similarities that bind the elements into a whole.

The goal of this work is to develop techniques to identify and interpret the specializations of the elements that compose various neural signaling systems in order to gain insight into their function. The systems described here are from the model organism *Drosophila melanogaster*: the synapses of the neuromuscular junction (Chapter 1), the glomeruli of the antennal lobe (Chapter 2), and the residues of Shaker potassium channel (Appendix 1). Together they represent signaling systems across a range of organizational scales within the nervous system of the fly. Each is characterized by heterogeneities that hint at functional specialization among its elements. This characterization was a two-stage process, consisting of 1) the development of an experimental methodology to observe the system's behavior, and 2) the development of software to visualize and quantify functional variations across the system.

The behavior of each system was observed using optical imaging, which relies on the use of a reporter whose light-emission characteristics correlate with the state of the system. By recording the light emitted throughout a region of space, one can simultaneously measure activity across many elements of the system, allowing one to directly witness the features that distinguish different elements. For the neuromuscular junction and the antennal lobe, this depended upon the use of fluorescent proteins that report the level of intracellular calcium, an ion that plays a critical

role in many aspects of neural signaling. Characterization of the Shaker channel was based upon a different approach, in which the behavior of each residue on the channel was measured separately, and the results for all residues were combined into a virtual model of the channel, enabling the simultaneous comparison of residues.

The specialization of each system was visualized and analyzed using computer software. This included the development of a system to organize and query data files as well as scripts to mine these files in order to generate visualizations and quantitative comparisons (Appendix 3). Visualization of each system enabled the authors to discover spatial patterns that hinted at the organizing principles that produced variations within the system. Semiautomatic mining of data enabled the rapid testing of hypotheses regarding the ways in which elements differed from each other. For the potassium channel and antennal lobe, this facilitated the interpretation of how the specialization of elements relates to their function within the system.

Interpreting heterogeneity in terms of functional specialization requires the convergence of multiple forms of evidence. For the antennal lobe, the unique response properties of a particular glomerulus could be interpreted within the context of its known role in detecting pheromones. For the Shaker channel, large changes in S4's fluorescence were meaningful in light of its previously established role as the voltage-sensing domain. There is currently no known correlate of the variation we find at the neuromuscular junction, and hence the role of the reported gradient of synaptic strength remains obscure.

What follows is an in-depth description and interpretation of the heterogeneity found across multiple scales within the *Drosophila* nervous system.

# Chapter 1

## Heterogeneity in synaptic transmission along a *Drosophila* larval motor axon

This chapter is from the publication: Giovanna Guerrero, Dierk F Rieff, Gautam Agarwal, Robin W Ball, Alexander Borst, Corey S Goodman & Ehud Y Isacoff. Heterogeneity in synaptic transmission along a *Drosophila* larval motor axon. Nature Neuroscience. 2005 Sep;8(9): 1188-96.

## Summary

At the *Drosophila* larval neuromuscular junction (NMJ), a motor neuron releases glutamate from 30-100 boutons onto the muscle it innervates. How transmission strength is distributed among the boutons of the NMJ is unknown. To address this, we created SynapCam, a version of the $Ca^{2+}$ reporter Cameleon. SynapCam localizes to the postsynapse and selectively reveals $Ca^{2+}$ influx through glutamate receptors (GluRs) with single-impulse and single-bouton resolution. GluR-based $Ca^{2+}$ signals were uniform within a given connection (*i.e.*, bouton and postsynapse pair), but differed considerably among connections of an NMJ. A steep gradient of transmission strength was observed along axonal branches, from weak proximal connections to strong distal ones. Presynaptic imaging revealed a matching axonal gradient, with higher $Ca^{2+}$ influx and exocytosis at distal boutons. The results suggest that transmission strength is mainly determined presynaptically at the level of individual boutons, possibly by one or more factors existing in a gradient.

## Introduction

Neurons form synaptic connections with one, a few, or hundreds of postsynaptic cells, and an individual neuron may make single or multiple connections with a postsynaptic partner. These connections can change in number, strength, and properties of short and long-term plasticity, both during development and as a consequence of experience in the mature nervous system (1-4). Classically, transmission has been measured electrophysiologically, enabling an assessment of the overall strength of transmission between a pair of cells, but without knowledge of the number of connections between them. For simplicity, it has usually been assumed that all connections between two cells share similar properties. With advances in imaging, it has become feasible to selectively measure transmission at individual connections, either by following the presynaptic release of FM dyes during transmitter exocytosis or by monitoring the rise in postsynaptic $Ca^{2+}$ due to influx via transmitter-gated receptors, voltage-gated $Ca^{2+}$ channels, or transmitter-triggered release from intracellular stores (5-8), and to test whether or not synaptic connections between a presynaptic cell and a postsynaptic partner have equal strength. This question has not

yet been extensively addressed, but elegant evidence has been obtained that $Ca^{2+}$ dynamics, release probability, and short-term plasticity may vary across the different connections from one presynaptic cell (8-10). Here we investigate how transmission is distributed among the multiple connections between a presynaptic neuron and its muscle partner in the developing NMJ of the *Drosophila* larva, a synapse that can be readily accessed for electrophysiology and easily imaged in a semi-intact preparation. The *Drosophila* larval NMJ shares important structural and molecular properties with mammalian CNS synapses. It is glutamatergic, with non-NMDA-type ionotropic glutamate receptors, and both the presynaptic active zones and postsynaptic specializations are organized through PDZ interactions in similar fashion to mammalian synapses (11,12). In addition, as in certain CNS synapses such as hippocampal CA1 inputs (13), the NMJ involves multiple neuronal connections onto the postsynaptic muscle. The NMJ also exhibits structural and functional plasticity. During larval development, muscle size increases more than 100-fold, causing a decrease in input resistance. To effectively depolarize and contract the muscle, synaptic currents must also increase as the larva grows. Two general mechanisms upregulate synaptic currents during development: one that regulates presynaptic structure and another that regulates transmission strength. During larval development the degree of axonal branching as well as the number of boutons and active zones increase (14,15). Nascent boutons emerge either *de novo* or by budding from pre-existing boutons, and come equipped with vesicles and active zones (16). A muscle-secreted BMP is essential for this developmental growth (17) and its presynaptic receptor, Wishful thinking (Wit) (18,19), has been implicated both in the structural growth of the NMJ as well as in the retrograde signaling that strengthens synaptic transmission (20). It is not known how synaptic strength is distributed at this multisynaptic connection or how the mechanisms that regulate its growth and transmission may help to establish and maintain this distribution.

To clarify this, we compared transmission from different connections of an individual neuron in the *Drosophila* NMJ using a novel optical approach. A genetically-encoded fluorescent $Ca^{2+}$ reporter was used to detect postsynaptic $Ca^{2+}$ flux through GluRs, which in *Drosophila* are permeable to $Ca^{2+}$ (21). Versions of the fluorescence resonance energy transfer (FRET)-based reporter Cameleon (22,23) were targeted to postsynaptic sites via fusion to the single-pass transmembrane domain of CD8, as well as to the C-terminal PDZ-interaction domain of the Shaker $K^+$ channel (16). These genetic chimeras (SynapCams) were localized to the muscle's subsynaptic reticulum (SSR, *i.e.*, postsynaptic membrane folds that envelop presynaptic boutons), through the interaction of the Shaker C-terminus with the PDZ protein Discs large (Dlg) (11,12). This targeting, combined with the lower $Ca^{2+}$ affinity of a mutated version of the fluorescent reporter, allowed simultaneous monitoring of synaptic transmission across a population of

connections in response to single action potentials. We found that transmission strength varies among connections in a gradient along the length of axonal branches, with distal connections making stronger functional associations. We consider mechanisms that may be responsible for generating this gradient.

## Results

### Synapcam design: a postsynaptically targeted cameleon

We measured synaptic activity at the Drosophila larval NMJ electrically using voltage-clamp and optically with genetically encoded $Ca^{2+}$ sensors whose expression was driven in muscles by the myosin heavy chain promoter (MHC) (24). Various versions of the FRET-based $Ca^{2+}$ sensor Cameleon (22, 23) were used to construct reporters, which we called synapcams, that were localized to the postsynaptic cell membrane. The reporters were targeted to the muscle plasma membrane by the heterologous transmembrane protein CD8 and to the SSR by the PDZ interaction domain of the Shaker C terminus (Fig. 1a), as done previously (16) for the targeting of a green fluorescent protein (GFP). The attachment of CD8 was necessary for efficient targeting. Fusion to the Shaker C terminus without CD8 produced weaker accumulation at postsynaptic sites (data not shown). Synapcams, however, were mostly localized at postsynaptic sites that surround presynaptic boutons (that is, postsynapse), with lower levels in the nonsynaptic muscle membrane (Fig. 1b). These reporters thus permitted vital imaging of the subsynaptic structure. Muscle 6, the muscle used in these experiments, is innervated by type Ib boutons (3−8 μm) from motor neuron RP3, and type Is boutons from motor neuron 6/7b (1−3 μm) (15, 25). Synapcam fluorescence was greater at type Ib postsynapses, presumably because these are enveloped with more extensive SSR (14, 16, 26). We thus focused our analysis on type Ib postsynapses.

Expression of synapcams did not affect muscle viability, nor did it affect NMJ morphology. In addition, the localization of synaptic proteins such as GluRs, Dlg or synaptotagmin (Syt) (Fig. 1c −f) as well as physiological parameters such as the resting membrane potential and the amplitudes of spontaneous and evoked junctional potentials (EJPs) and currents (EJCs) in *synapcam$^{+/+}$* larvae were indistinguishable from wild-type larvae (Fig. 1g,h and Supplementary Table 1). Thus, expression of synapcams did not interfere with synaptic transmission or perturb the development of the NMJ.

### Synapcam reports on glutamate neurotransmission

Cameleon is a ratiometric reporter that makes use of fluorescence resonance energy transfer (FRET) (22). When the calmodulin domain of cameleon binds $Ca^{2+}$, the protein undergoes a conformational change that increases the efficiency of FRET between the cyan fluorescent protein (CFP) and yellow fluorescent protein (YFP) fluorophores, producing a decrease in CFP

emission and an increase in YFP emission. Single stimulation of the motor axon resulted in reciprocal changes in the CFP and YFP intensities of postsynaptic areas expressing synapcam (Fig. 2a,b) indicating an increase in FRET efficiency. Nonsynaptic muscle regions of *synapcam* $^{+/+}$ larvae (Fig. 2a,b) and muscle fibers expressing cytosolic Cam2.1 or CD8-Cam2.1 showed few or no fluorescence changes in response to axon stimulation (data not shown).

We created two different synapcam constructs and compared their optical responses. *synapcam2.1* retains all four $Ca^{2+}$ binding sites of calmodulin, and *synapcam3.1* encodes a mutation (E104Q) that abolishes one binding site in the N-terminal lobe (22). We found that both reporters showed significant changes in FRET ($\Delta$FRET) at postsynaptic regions (Fig. 2c). FRET began increasing 20 ms after the postsynaptic current and reached a peak within 120 ms for *synapcam3.1* and within 200 ms for *synapcam2.1*. The mean peak response for *synapcam2.1* was 18.18% greater than that for *synapcam3.1* (0.385 ± 0.138 and 0.315 ± 0.120, respectively), and the decay of the response was slower ($\tau$ = 192.63 ms ± 5.95 and  $\tau$ = 599.65 ± 11.04, respectively). These results were consistent with the greater $Ca^{2+}$ affinity of Cameleon2.1 (refs. 22, 23). Because the rise phases overlapped for synapcam2.1 and 3.1, the earlier peaking of synapcam3.1 is likely attributable to a faster recovery rate. Rapid kinetics and a lower $Ca^{2+}$ affinity made synapcam3.1 a more attractive reporter for subsequent experiments.

Although results strongly suggested that synapcams functioned in Drosophila muscle as synaptic $Ca^{2+}$ sensors, it remained possible that the GFP variants were in part responding to changes in pH or halides. Synapses expressing synapcamNull, a reporter with all four $Ca^{2+}$ binding sites abolished by mutation (Fig. 1a), showed no fluorescence change in response to neurotransmission (Fig. 2d, green trace). This result demonstrated that $\Delta$FRET was indeed reporting an increase in postsynaptic $Ca^{2+}$ resulting from neurotransmission.

To focus exclusively on $Ca^{2+}$ influx through GluRs, $Ca^{2+}$ from internal stores was depleted with thapsigargin (27) while residual $Ca^{2+}$ efflux from the stores was blocked with ryanodine (28). In addition, the interrogated muscle was voltage clamped to prevent activation of voltage-gated $Ca^{2+}$ channels. Under these conditions, desensitization of GluRs by bath-applied glutamate abolished both the FRET response and the EJC (current 94 ± 5%, fluorescence 88 ± 9% decrease, three NMJs, three traces each; Fig. 2d, red trace), demonstrating that GluR-derived currents were necessary for the optical response of synapcam. Depolarizing voltage jumps designed to open voltage-gated $Ca^{2+}$ channels did not induce $\Delta$FRET (Fig. 2d, gray trace),

4

indicating that voltage-gated $Ca^{2+}$ channels did not contribute detectable synaptic $Ca^{2+}$ under our recording conditions. Thus, synapcams provided a selective optical report of postsynaptic currents generated entirely from activated GluRs.

**Heterogeneous transmission among connections of the NMJ**
To assess the contribution of individual connections to overall transmission at the NMJ, discrete postsynaptic areas under presynaptic boutons were individually analyzed (Fig. 3a). Each postsynapse measured (801 in 65 NMJs from 62 larvae) showed a ΔFRET in response to axon stimulation (that is, no silent connections were observed, consistent with previous results from focal electrophysiological recordings (29). However, postsynaptic ΔFRETs sometimes fluctuated in amplitude during repetitive presynaptic stimulation (Fig. 3b). These fluctuations were independent of fluctuations occurring at other postsynapses, including close neighbors (Fig. 3b, compare green postsynapse versus blue postsynapse). Similarly, there was no pairwise correlation between the ΔFRET response of a postsynapse and the distance separating it from another postsynapse (Fig. 3c). These observations indicated that $Ca^{2+}$ influx at one postsynapse did not activate sensor readout at a nearby postsynapse, thus providing single postsynapse (that is, single-bouton) resolution.

The magnitude of ΔFRET differed considerably among postsynapses of a single axon (Fig. 3a,b). Of 65 NMJs tested, the amplitudes differed two- to 14-fold among postsynapses of the same NMJ. This observed heterogeneity in FRET might stem from biological variation, such as presynaptic differences in transmitter release or differences in postsynaptic sensitivity. Alternatively, it could arise from differences between postsynapses in synapcam numbers or readout. However, there was no correlation between relative reporter quantity and ΔFRET (Fig. 4c) and moreover, ΔFRET responses peaked sharply, arguing against saturation of synapcam (Fig. 3). This possibility was tested directly by comparing the ΔFRET response after a single stimulus against the response to a pair of stimuli given in rapid succession. If small FRET changes were due to saturated postsynapses, stimulus pairs would not be expected to have an increased FRET response.

Stimuli were separated by 10 ms and produced two separate EJCs. Although the current amplitude of the second pulse was depressed by approximately 28% (first pulse, -363.8 ± 18.5 nA; second pulse, -261.9 ± 8.4 nA), as expected for the $Ca^{2+}$ concentration used, the stimulus pair produced '' FRET amplitudes larger than a single stimulus, owing to summation of the synapcam responses (Fig. 4a). Taken together, 41 boutons from five NMJs showed linear increases in the FRET response to the stimulus pair as compared with the single stimulus (Fig. 4b), indicating that for single pulses at low frequency, as used throughout our analysis, the

reporter is not saturated at any boutons along the axon, whether they are proximal or distal or their responses large or small. The ratio of ΔFRET from a pulse pair relative to the response for single pulse (mean of 1.84 ± 0.05) showed a slight negative dependence on the '' FRET after a single stimulus (Supplementary Fig. 1). This dependence could be due to presynaptic depression, as the EJC showed a similar trend (Supplementary Fig. 1). Taken together, the results indicate that heterogeneity in ΔFRET stems from biological variation in neurotransmission.

**Active zone or GluR numbers do not determine heterogeneity**

Because synapcam responds to $Ca^{2+}$ influx through GluRs, the inhomogeneity in synaptic transmission might arise from differences among the postsynaptic sites in the number of GluRs. Alternatively, $Ca^{2+}$ influx might also be affected by GluR subunit composition. Five GluRs are expressed in the muscles of Drosophila larvae (30, 31, 32). DGluRIIA and DGluRIIB compete with each other for assembly with the other subunits and for membrane expression (31, 32). In addition, DGluRIIB desensitizes more rapidly than DGluRIIA, leading to reduced macroscopic currents in muscles overexpressing DgluRIIB (33). Differences between postsynapses in the numbers of DGluRIIB subunits and DGluRIIA subunits might thus affect $Ca^{2+}$ influx. To test these possibilities, NMJs were fixed immediately after imaging synapcam and stained with antibodies against DGluRIIA and DGluRIIB. The amplitude of the ΔFRET signals showed very weak correlation or no correlation to DGluRIIA or DGluRIIB staining or to the ratio of the number of DGluRIIA to DGluRIIB subunits (Supplementary Fig. 2). On average, postsynapses that differed by no more than 50% in number of GluRs could differ in ΔFRET amplitude by as much as 1000% (Supplementary Fig. 2). Thus, inhomogeneity in synapcam responses among postsynapses of an NMJ could not be attributed to differences in the number or composition of GluRs.

Transmission heterogeneity might also stem from presynaptic differences among boutons. Type Ib boutons contain multiple active zones (14), and larger boutons tend to contain more active zones. We tested if differences in the number of active zones accounted for the observed transmission inhomogeneity. There was no correlation between the amplitude of ΔFRET response and the size of the presynaptic bouton (Fig. 4d). Moreover, immunostaining with the antibody Nc82, which stains presynaptic active zones opposite postsynaptic patches of GluRs (ref. 34; Fig. 1b), showed that neither the immunofluorescence intensity nor the density of Nc82 puncta per bouton correlated with the ΔFRET from individual boutons (Supplementary Fig. 3).

**A gradient of transmission strength along axonal branches**
To describe the spatial distribution of synaptic transmission across the connections of the motor axon, continuous imaging (Figs. 2, 3, 4) was replaced by episodic imaging (Fig. 5a; see Methods)

to minimize photobleaching and allow the acquisition of data for hundreds of events. FRET images of the synaptic region (Fig. 5b), averaged from responses to 50−300 stimuli, provided high signal-to-noise ΔFRET measurements from type Ib boutons and also enabled optical detection of transmission from type Is boutons (Fig. 5e). However, because the type Is boutons were more difficult to identify in the YFP images, we did not pursue them at this stage.

Pronounced differences were observed in the potency of postsynapses. Although there was some variation between individual stimuli, strong postsynapses tended to stay strong throughout the trial (Fig. 5c). We never observed a drastic change in the transmission distribution across postsynapses. ΔFRET images from type Ib boutons showed that adjacent postsynapses of similar size, reporter expression, and resting FRET (rFRET) could differ markedly in transmission strength (Fig. 5e), confirming results from single stimulation that suggest $Ca^{2+}$ entry is confined to the physical limits of a postsynapse and that reporter expression or rFRET did not determine a postsynapse's ΔFRET.

Our analysis of 440 postsynapses from 91 axonal branches showed that strong and weak synaptic connections were not randomly distributed throughout the motor axon, but rather were organized in a gradient along the length of axonal branches (Fig. 6). Horseradish peroxidase (HRP)-specific staining after imaging traced the axon branches from the first point of muscle contact, to secondary branch points, to terminal boutons (Fig. 6a). Postsynapses at the ends of branches consistently showed the greatest ΔFRET responses (Fig. 6c,d,f–i), whereas postsynapses at the origins of branches were always among the weakest. The ΔFRET gradient was not due to differences in the amount of synapcam, because rFRET (Fig. 6b) did not show consistent trends in intensity along a branch (Fig. 6e,j). ΔFRET decreased linearly with greater distance from the end of a branch and with the connection position along an axonal branch (Fig. 6j,k). This distal-to-proximal gradient of transmission strength, from strong distal connections to weak proximal ones, was observed in both simple and complex branching patterns (Fig. 6h). Terminal postsynapses from different branches within the same NMJ also differed significantly in terms of transmission potency (Fig. 6i). The gradient in transmission strength was not dependent upon the relative location of the axon branch along the muscle surface. Transmission at terminal connections was always stronger regardless of location along the length of the muscle fiber. Moreover, the gradient was also independent on branch orientation, whether the branch ran parallel, perpendicular to, or obliquely across the muscle fiber (Fig. 6h,i). These observations suggested that the gradient in transmission strength was not a function of postsynaptic polarity but instead depended solely on the location of a bouton relative to the axon branch.

Two exceptions were found which disrupted the commonly seen gradient of transmission strength. One of these was at boutons that were budding-off from established boutons. Budding

boutons at the terminus of a branch had lower transmission strength than mature boutons from which they budded (Fig. 6d, lower green bouton budding from yellow bouton). A second exception occurred when an axon branch had a sharp kink. Boutons located on the proximal side of the bend had higher ΔFRET values than boutons following it, as if they were terminal boutons (Fig. 6g). The dependence of transmission strength on fine axon morphology supported the idea that the gradient is established presynaptically.

**Presynaptic release is stronger at end boutons**

We have documented a gradient in synaptic transmission that makes the connections of distal boutons stronger than proximal ones along the length of the motor axon. These measurements were made postsynaptically, but the lack of correlation to GluR levels and the dependence on axon morphology suggested that the locus of the gradient was presynaptic. To test this idea, presynaptic fluorescent reporters were used to measure $Ca^{2+}$ influx and synaptic vesicle fusion at each bouton. Presynaptic $Ca^{2+}$ was monitored with a version of cameleon, Cam2.3 (ref. 35), expressed pan-neuronally. Motor axons were subjected to 40-Hz trains of stimuli, a frequency that, in this preparation, does not saturate the reporter (36). Larger rises in $Ca^{2+}$ were observed at distal boutons than at boutons 2−3 positions from the end (Fig. 7a,b), indicating greater $Ca^{2+}$ influx and suggesting greater transmitter release at the ends of axons. This finding led us to assay vesicle release directly. This was done in flies expressing superecliptic Synapto-pHluorin (SpH), a GFP-based sensor that reports vesicle fusion by exploiting differences in pH between the intravesicular and extracellular space (37). A greater activity-dependent increase in fluorescence, indicating greater exocytosis, was observed at distal boutons than at boutons 2−3 positions from the end (Fig. 7c). This provided direct evidence for greater release from distal boutons. Thus, transmission at the Drosophila NMJ seemed to be greater at the ends of axonal branches, and this gradient seems to be due in part to greater $Ca^{2+}$ influx and vesicle fusion presynaptically.

## Discussion

By targeting a genetically encoded $Ca^{2+}$ sensor to postsynaptic sites, near $Ca^{2+}$-permeant GluRs, we have monitored glutamatergic transmission optically with single-bouton resolution at the Drosophila larval NMJ. While highly responsive to $Ca^{2+}$ influx through GluRs, the sensor is relatively blind to influx through voltage-gated $Ca^{2+}$ channels (Fig. 2), and in response to a presynaptic action potential, the ΔFRET at one postsynapse is independent of ΔFRET at an adjacent postsynapse (Figs. 3 and 5). As a result, synapcam enables the simultaneous examination of transmission at multiple synaptic connections in response to single presynaptic action potentials. This approach is promising in that similar targeting of low-affinity optical

$Ca^{2+}$ sensors to specific $Ca^{2+}$ channels such as NMDA and IP3 receptors or to voltage-gated $Ca^{2+}$ channels in mammalian neurons could enable visualization in dendrites of the spatial spread of the $Ca^{2+}$ fluctuations that trigger long-lasting changes in synaptic strength.

Although all connections at the Drosophila NMJ participated in neurotransmission, the strength of transmission was found to vary greatly from bouton to bouton. The position of a particular synaptic connection with respect to the origin of a branch or sub-branch determines its transmission potency. Distal boutons are the strongest, with a progressive decline in transmission strength in boutons nearer to the origin of the axon branch (Fig. 6). Although this type of organized transmission heterogeneity has never before been documented for the Drosophila NMJ, transmission gradients have been observed before at crayfish, frog and mouse NMJs (38, 39, 40, 41). These studies used serial single-bouton or single-muscle fiber recordings to compare proximal and distal connections. The targeting of a $Ca^{2+}$ fluorescent reporter to postsynaptic sites made it possible for us to capture the same kind of information in parallel in single snapshots. In those earlier NMJ studies, differences in release probability, the size of SSR folds, or failure of action potential propagation were proposed to explain the gradients (42, 43). Action potential propagation failure cannot explain our observation of stronger transmission at distal connections in Drosophila larvae. In addition, we do not observe a gradient in either postsynapse size or quantity of synapcam along the synaptic connections made by an axon (Fig. 4), arguing against systematic differences in the SSR. Finally, the quantity of GluRs and the molecular identity of the GluR subunits at a postsynapse are not organized in a gradient (Supplementary Fig. 2). Notably, in addition to receptor quantity and subunit composition, the phosphorylation state of GluRs has been shown to affect quantal size at the NMJ (44). Although we did not investigate the phosphorylation state of the GluRs at each bouton, the effect of phosphorylation on GluRs cannot quantitatively account for the gradient observed. At most phosphorylation decreases quantal size by 60% (ref. 44). This cannot account for the 1,000% differences that we observe. In summary, we have not found a strong postsynaptic correlate for the establishment of a transmission gradient. However, we did find increased presynaptic $Ca^{2+}$ and vesicle fusion at distal boutons (Fig. 7) indicating that a presynaptic mechanism that controls transmitter release has a major role in the establishment of the transmission gradient. Although release probability was not measured directly in this study, the number of active zones was not organized in a spatial gradient along the boutons of an NMJ (Supplementary Fig. 3). Still, from earlier work at the Drosophila and Crayfish NMJs, it seems that more efficient transmitter release occurs at active zones that are associated with electron dense specializations known as 'T-bars' (20, 42, 45, 46). Hence, it is conceivable that more distal boutons have larger numbers of T-bars. Alternatively, differences in several other parameters that regulate release probability or the mode of release could have a role.

We find that the gradient in transmission strength does not depend on the relative position of a bouton on the muscle surface, suggesting it is determined presynaptically by the polarity of the axon. This idea is supported by our finding of greater $Ca^{2+}$ influx and vesicle fusion at distal boutons. In principle, this finding is consistent with either a positive regulator of transmission that is preferentially concentrated at the ends of axon branches, or a negative regulator of transmission that is delivered in limiting amounts and accumulates more in the first boutons it reaches during anterograde transport (Supplementary Fig. 4). Because bouton addition occurs throughout the length of the axon, not only at the ends of branches but also between previously established boutons (16), a proximal-distal gradient in a bouton's developmental age is not likely to fully explain the gradient in transmission strength. Notably, a gradient has been observed in the arrangement of the microtubule associated protein 1B (MAP1B) along microtubules in the presynaptic terminal. Immunofluorescent mapping of MAP1B shows tight bundles of microtubules along axon branches with a higher incidence of microtubule 'loops' at branch points and branch ends, as well as disarrayed microtubule patterns at the most distal boutons (47, 48). It is possible that as well as promoting the growth of the presynaptic terminal, microtubules may also have a role transporting components needed for synaptic transmission down the length of axon branches. Perhaps microtubule loops in axon kinks and at the end of branches, as well as microtubule disarray at the most distal boutons, favor the deposition of positive regulatory factors that increase transmission strength. It will be interesting in the future to examine the role of microtubules in determining transmission strength and to identify any regulatory factors existing in an axonal gradient.

## Methods

### DNA constructs and flies.

*Yellow cameleon* (*cam*) *3.1* (gift from R.Y. Tsien, University of California San Diego) was converted to *cam2.1* by reverting the Q104E mutation through site-directed mutagenesis (Quickchange, Stratagene). *cam-null* was derived from *cam3.1* by mutations E31Q, E67Q and E140Q, which abolish the $Ca^{2+}$ binding sites. To target cameleon variants to the synapse (in other words, to create the *synapcam* construct), *cam2.1*, *cam3.1* and *cam-null* were amplified with *Spe*I primers (5'-GG ACT AGT GCC GCC ACC ATG GTG AGC-3' and 5'-GG ACT AGT GCA GAA TTC CTT GTA CAG-3') and inserted into the *Spe*I sites of the CD8-GFP-Sh construct (16), exchanging GFP for each *cam* variant. The genetic chimeras were placed under control of the MHC promoter (24). Transgenic flies were made using standard germline transformation by embryo injection. Single insertions on the X chromosome were identified by orange eye color and confirmed by segregation analysis. Female larvae were used in all experiments.

For presynaptic exocytosis and calcium imaging, respectively, UAS-SpH (37) and UAS-Cam2.3 (ref. 36) were driven pan-neuronally with *elav^C155-Gal4*. UAS-monomeric-DsRed flies were a gift from G. Tavosanis, European Molecular Biology Laboratory. The genotype of animals expressing SpH and mDsRed was *elavc155-Gal4^{+/-}*, *UAS-SpH^{+/-}*, *UAS-mDsRed^{+/-}*.

**Immunohistochemistry and analysis.**
Larvae were fixed immediately after physiological recordings, either with Bouin's fixative for 5 min (DGluRIIA and DGluRIIB) or with 4% formaldehyde for 30 min (Nc82, Syt, HRP). The following primary antibodies were used: mouse anti-DGluRIIA (1:100) (31), mouse anti-Syt (1:5), mouse anti-Dlg (1:100), mouse anti-HRP (1:100; Sigma), rabbit anti-DGluRIIB (1:2,500) (31) and NC-82 (1:100, gift from E. Buchner, University of Wurzburg). Alexa 647–conjugated goat anti-mouse and Cy3-conjugated goat anti-rabbit secondary antibodies were used for double-labeling experiments (Molecular Probes).

Metamorph (Universal Imaging) was used to calculate the intensities of YFP, GluRs and Nc82 staining from confocal images. Because GluRs and Nc82 antibodies label in a punctal pattern, images were thresholded in Metamorph to discard grey levels below minimal staining. Total intensity was calculated for values above threshold within each postsynaptic terminal. The density of staining was taken as the percentage of area above threshold for a postsynaptic terminal.

**Electrophysiology.**
Two-electrode voltage clamp recordings were done with an AxoClamp 2B amplifier (Axon Instruments) on Drosophila muscle 6 at segments A2 or A3 of third instar larvae. Unless otherwise stated, recording solution consisted of physiological saline HL3 (ref. 49) containing 1.5 mM $Ca^{2+}$, 20 mM $Mg^{2+}$, 2 M thapsigargin and 500 M ryanodine. For presynaptic imaging, 7 mM glutamate was added to prevent muscle contraction during high-frequency stimulation. Recording electrodes contained 3 M KCl and had resistances between 10–20 M. Only muscles with a resting membrane potential below -60 mV were chosen for study. For EJC studies, the nerve was stimulated at 0.1 Hz and muscles clamped at -80 mV. During image acquisition, muscles were held at -100 mV. The more negative holding potential (-100 mV) improved cameleon signaling, presumably by increasing the $Ca^{2+}$ driving force. Data were filtered at 1 KHz and recorded using a Digidata 1200A/B board and Clampex 8.0 software (Axon Instruments). mEJCs were analyzed with MiniAnalysis software (Synaptosoft), and other electrophysiological data were analyzed with Clampfit 8.0 (Axon Instruments).

**Optical recording of FRET.**

Larvae were imaged with an ORCA-ER charge-coupled device (CCD) camera (Hamamatsu) and an Olympus BX-50WI microscope (Olympus) with a 75-W Xenon lamp and a 60x 0.9NA objective (Olympus). Excitation was at $434 \pm 10$ nm using a 460-nm dichroic filter. Emission wavelengths were separated with a dual-emission beam splitter (Optical Insights) with a 510 nm dichroic filter and $480 \pm 20$ nm and $535 \pm 20$ nm emission filters. Images were collected with SimplePCI software (Compix) at either 53 or 35 frames/s (8x8 or 4x4 binning, respectively). For presynaptic vesicle fusion experiments, mDsRed was excited at 550 nm with Q585LP and HQ620/60 filters, and SpH was excited at 470 nm with a Q480LP and a HQ535/50 band pass. All filters and dichroics were from Chroma Technology.

To obtain an accurate representation of amplitude and spatial distributions of transmission across synapses, the initial continuous imaging (Figs 2, 3, 4) was substituted with episodic imaging, thereby minimizing photobleaching and allowing more responses to be measured. A pair of CCD images was acquired per stimulus, one before stimulation (baseline) and one 100 ms after stimulation (around the peak of the synapcam response; Fig. 5a). Under these conditions, the synapse could be imaged for up to 30 min while recording hundreds of responses. Responses were sub-saturating at all boutons (Fig. 4a), with a similar doubling of ΔFRET at distal (1.98 ± 0.15) and proximal (1.96 ± 0.8) postsynaptic terminals in response to a pulse pair.

**Image analysis.**

Image analysis (Figs. 2, 3, 4) was performed with Bouton Project, software that enables overlaying CFP and YFP data, defining regions of interest and quantifying fluorescence change over time (D. Raymond, University of California Berkeley, personal communication). For extended experiments where two frames were acquired before and after stimulation (Figs. 5, 6, 7), images were analyzed in Matlab 7.0 (Mathworks). Details about image analysis are described in Supplementary Methods.

## Acknowledgments

## Supporting Information

Supporing information is available at
http://www.nature.com/neuro/journal/v8/n9/suppinfo/nn1526_S1.html

## References

1. Hua JY, Smith SJ. Neural activity and the dynamics of central nervous system development. Nat. Neurosci. 2004;7:327 332.

2. Constantine-Paton M, Cline HT. LTP and activity-dependent synaptogenesis: the more alike they are, the more different they become. Curr. Opin. Neurobiol. 1998;8:139 48.

3. Turrigiano GG, Nelson SB. Hebb and homeostasis in neuronal plasticity. Curr. Opin. Neurobiol. 2000;10:358 64.

4. Liu G. Presynaptic control of quantal size: kinetic mechanisms and implications for synaptic transmission and plasticity. Curr. Opin. Neurobiol. 2003;13:324 31.

5. Oertner TG. Functional imaging of single synapses in brain slices. Exp. Physiol. 2002;87:733 6.

6. Fetcho JR, O'Malley DM. Imaging neuronal networks in behaving animals. Curr. Opin. Neurobiol. 1997;7:832 8.

7. Murthy VN. Optical detection of synaptic vesicle exocytosis and endocytosis. Curr. Opin. Neurobiol. 1999;9:314 20.

8. Koester HJ, Johnston D. Target Cell-Dependent Normalization of Transmitter Release at Neocortical Synapses. Science. 2005;308:863 866.

9. Murthy VN, Sejnowski TJ, Stevens CF. Heterogeneous release properties of visualized individual hippocampal synapses. Neuron. 1997;18:599 612.

10. Koester HJ, Sakmann B. Calcium dynamics associated with action potentials in single nerve terminals of pyramidal cells in layer 2/3 of the young rat neocortex. J. Physiol. 2000;529(Pt 3): 625 46.

11. Zito K, Fetter RD, Goodman CS, Isacoff EY. Synaptic clustering of Fasciclin II and Shaker: Essential targeting sequences and role of Dlg. Neuron. 1997;19:1007 1016.

12. Tejedor FJ, et al. Essential role for dlg in synaptic clustering of shaker K+ channels in vivo. J. Neurosci. 1997;17:152 159.

13. Sorra KE, Harris KM. Occurrence and three-dimensional structure of multiple synapses between individual radiatum axons and their target pyramidal cells in hippocampal area CA1. J. Neurosci. 1993;13:3736 48.

14. Atwood HL, Govind CK, Wu C-F. Differential ultrastructure of synaptic terminals on ventral longitudinal abdominal muscles in *Drosophila* larvae. J. Neurobiol. 1993;24:1008 1024.

15. Schuster CM, Davis GW, Fetter RD, Goodman CS. Genetic dissection of structural and functional components of synaptic plasticity. I. Fasciclin II controls synaptic stabilization and growth. Neuron. 1996;17:641 54.

16. Zito K, Parnas D, Fetter RD, Isacoff EY, Goodman CS. Watching a synapse grow: Noninvasive confocal imaging of synaptic growth in Drosophila. Neuron. 1999;22:719 729.

17. McCabe BD, et al. The BMP homolog Gbb provides a retrograde signal that regulates synaptic growth at the Drosophila neuromuscular junction. Neuron. 2003;39:241 54.

18. Aberle H, et al. wishful thinking encodes a BMP type II receptor that regulates synaptic growth in Drosophila. Neuron. 2002;33:545 58.

19. Marques G, et al. The Drosophila BMP type II receptor Wishful Thinking regulates neuromuscular synapse morphology and function. Neuron. 2002;33:529 43.

20. Haghighi AP, et al. Retrograde control of synaptic transmission by postsynaptic CaMKII at the Drosophila neuromuscular junction. Neuron. 2003;39:255 67.

21. Chang H, Ciani S, Kidokoro Y. Ion permeation properties of the glutamate receptor channel in cultured embryonic Drosophila myotubes. J. Physiol. 1994;476:1 16.

22. Miyawaki A, et al. Fluorescent indicators for Ca2+ based on green fluorescent proteins and calmodulin. Nature. 1997;388:882 887.

23. Miyawaki A, Griesbeck O, Heim R, Tsien RY. Dynamic and quantitative Ca2+ measurements using improved cameleons. Proc. Natl. Acad. Sci. U. S. A. 1999;96:2135 2140.

24. Chiba A, Snow P, Keshishian H, Hotta Y. Fasciclin III as a synaptic target recognition molecule in Drosophila. Nature. 1995;374:166 8.

25. Johansen J, Halpern ME, Johansen KM, Keshishian H. Stereotypic morphology of glutamatergic synapses on identified muscle cells of Drosophila larvae. J. Neurosci. 1989;9:710 25.

26. Jia XX, Gorczyca M, Budnik V. Ultrastructure of neuromuscular junctions in Drosophila: comparison of wild type and mutants with increased excitability. J. Neurobiol. 1993;24:1025 44.

27. Treiman M, Caspersen C, Christensen SB. A tool coming of age: thapsigargin as an inhibitor of sarcoendoplasmic reticulum Ca2+-ATPases. Trends Pharmacol. Sci. 1998;19:131 135.

28. Sullivan KMC, Scott K, Zuker CS, Rubin GM. The ryanodine receptor is essential for larval development in Drosophila melanogaster. Proc. Natl. Acad. Sci. U. S. A. 2000;97:5942 5947.

29. Davis GW, Goodman CS. Synapse-specific control of synaptic efficacy at the terminals of a single neuron. Nature. 1998;392:82 6.

30. Petersen SA, Fetter RD, Noordemeer JN, Goodman CS, DiAntonio A. Genetic analysis of glutamate receptors in *Drosophila* reveals a retrograde signal regulating presynaptic transmitter release. Neuron. 1997;19:1237 1248.

31. Marrus SB, Portman SL, Allen MJ, Moffat KG, DiAntonio A. Differential localization of glutamate receptor subunits at the Drosophila neuromuscular junction. J. Neurosci. 2004;24:1406 15.

32. Qin G, et al. Four Different Subunits Are Essential for Expressing the Synaptic Glutamate Receptor at Neuromuscular Junctions of Drosophila. J. Neurosci. 2005;25:3209 3218.

33. DiAntonio A, Petersen SA, Heckmann M, Goodman CS. Glutamate Receptor Expression Regulates Quantal Size and Quantal Content at the Drosophila Neuromuscular Junction. J. Neurosci. 1999;19:3023 3032.

34. Wucherpfennig T, Wilsch-Brauninger M, Gonzalez-Gaitan M. Role of Drosophila Rab5 during endosomal trafficking at the synapse and evoked neurotransmitter release. J. Cell Biol. 2003;161:609 624.

35. Griesbeck O, Baird GS, Campbell RE, Zacharias DA, Tsien RY. Reducing the environmental sensitivity of yellow fluorescent protein. Mechanism and applications. J. Biol. Chem. 2001;276:29188   94.

36. Reiff DF, et al. In vivo performance of genetically encoded indicators of neural activity in flies. J. Neurosci. 2005;25:4766   78.

37. Miesenbock G, De Angelis DA, Rothman JE. Visualizing secretion and synaptic transmission with pH-sensitive green fluorescent proteins. Nature. 1998;394:192   195.

38. Atwood HL. Variation in physiological properties of crustacean motor synapses. Nature. 1967;215:57   8.

39. Lavidis NA, Bennett MR. Probabilistic secretion of quanta from visualized sympathetic nerve varicosities in mouse vas deferens. J. Physiol. 1992;454:9   26.

40. Bennett MR, Jones P, Lavidis NA. The probability of quantal secretion along visualized terminal branches at amphibian (Bufo marinus) neuromuscular synapses. J. Physiol. 1986;379:257   74.

41. Bittner GD. Differentiation of Nerve Terminals in the Crayfish Opener Muscle and Its Functional Significance. J. Gen. Physiol. 1968;51:731   758.

42. Cooper RL, Harrington CC, Marin L, Atwood HL. Quantal release at visualized terminals of a crayfish motor axon: intraterminal and regional differences. J. Comp. Neurol. 1996;375:583   600.

43. Robitaille R, Tremblay JP. Non-uniform responses to Ca2+ along the frog neuromuscular junction: effects on the probability of spontaneous and evoked transmitter release. Neuroscience. 1991;40:571   85.

44. Davis GW, DiAntonio A, Petersen SA, Goodman CS. Postsynaptic PKA controls quantal size and reveals a retrograde signal that regulates presynaptic transmitter release in Drosophila. Neuron. 1998;20:305   15.

45. Reiff DF, Thiel PR, Schuster CM. Differential Regulation of Active Zone Density during Long-Term Strengthening of Drosophila Neuromuscular Junctions. J. Neurosci. 2002;22:9399   9409.

46. Quigley PA, Msghina M, Govind CK, Atwood HL. Visible evidence for differences in synaptic effectiveness with activity-dependent vesicular uptake and release of FM1-43. J. Neurophys. 1999;81:356   370.

47. Roos J, Hummel T, Ng N, Klambt C, Davis GW. Drosophila Futsch regulates synaptic microtubule organization and is necessary for synaptic growth. Neuron. 2000;26:371   82.

48. Ruiz-Canada C, et al. New synaptic bouton formation is disrupted by misregulation of microtubule stability in aPKC mutants. Neuron. 2004;42:567   80.

49. Stewart BA, Atwood HL, Renger JJ, Wang J, Wu C-F. Improved stability of *Drosophila* larval neuromuscular preparations in haemolymph-like physiological solutions. J. Comp. Phys. 1994;175:179   191.

## Figures

**Figure 1. Synapcam expression has no affect on NMJ development or physiology.**

**Figure 2. Synapcams report Ca$^{2+}$ flux through GluRs as an increase in FRET.**

**Figure 3. Synapcam reveals transmission heterogeneity at the Drosophila NMJ.**

**Figure 4. Synapcam3.1 is not saturated by single stimuli to the motor axon.**

**Figure 5. Prolonged imaging shows the distribution of transmission strength of an NMJ.**

**Figure 6. A proximal-distal gradient in transmission strength.**

**Figure 7. Presynaptic contribution to the gradient of transmission strength.**

**Figure 1**
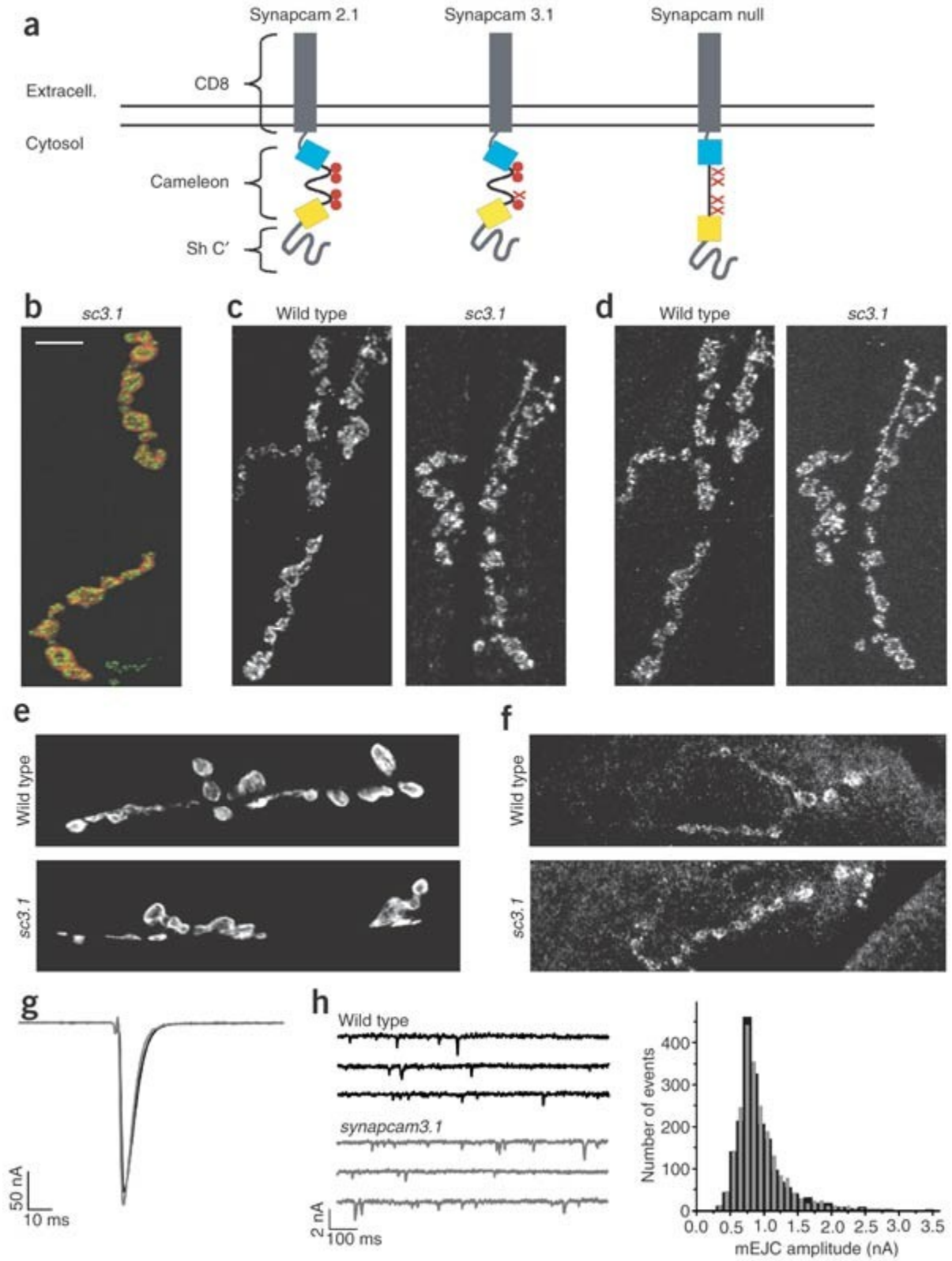
**Figure 1. Synapcam expression has no affect on NMJ development or physiology.**

**(a)** Synapcams are cameleons with CD8 at the N terminus and the PDZ interaction domain of the Shaker K$^+$ channel at the C terminus. Three versions of cameleon, differing in their sensitivity to Ca$^{2+}$ ions (red circles), were used: synapcam2.1, with all four Ca$^{2+}$ binding sites intact; synapcam3.1, with one site mutated to reduce Ca$^{2+}$ affinity and synapcamNull, with all four sites mutated to serve as a Ca$^{2+}$-insensitive control. **(b)** When expressed under the control of the MHC promoter, synapcam3.1 (shown in red, indicating YFP fluorescence) localized to muscle sites underlying presynaptic terminals of type Ib boutons (shown in green, stained with anti-Nc82, an active zone marker). **(c–e)** Flies expressing synapcam3.1 (*sc3.1*) showed no observable differences in the levels or localization of pre- or postsynaptic markers when compared to control larvae (wild type). Glutamate receptor subunits DGluRIIA and DGluRIIB **(c,d)**, Dlg **(e)** and Syt **(f)** were not perturbed by expression of synapcam3.1. All images shows muscles 6/7, except for f, which shows muscle 8. Scale bar: 10 μm. **(g,h)** Physiological parameters were also unaffected. Neither EJCs (g, *n* = 10 NMJs) nor the amplitude distribution of spontaneous miniature quantal events (mEJCs, h) were affected by expression of synapcam3.1 or the experimental conditions (2 μM thapsigargin and 500 μM ryanodine) that prevented muscle contraction. The histogram in h depicts six NMJs and 1,953 events for *w1118* (black), and nine NMJs and 2,191 events from *synapcam3.1* (gray). The holding potential for g and h was -80 mV.
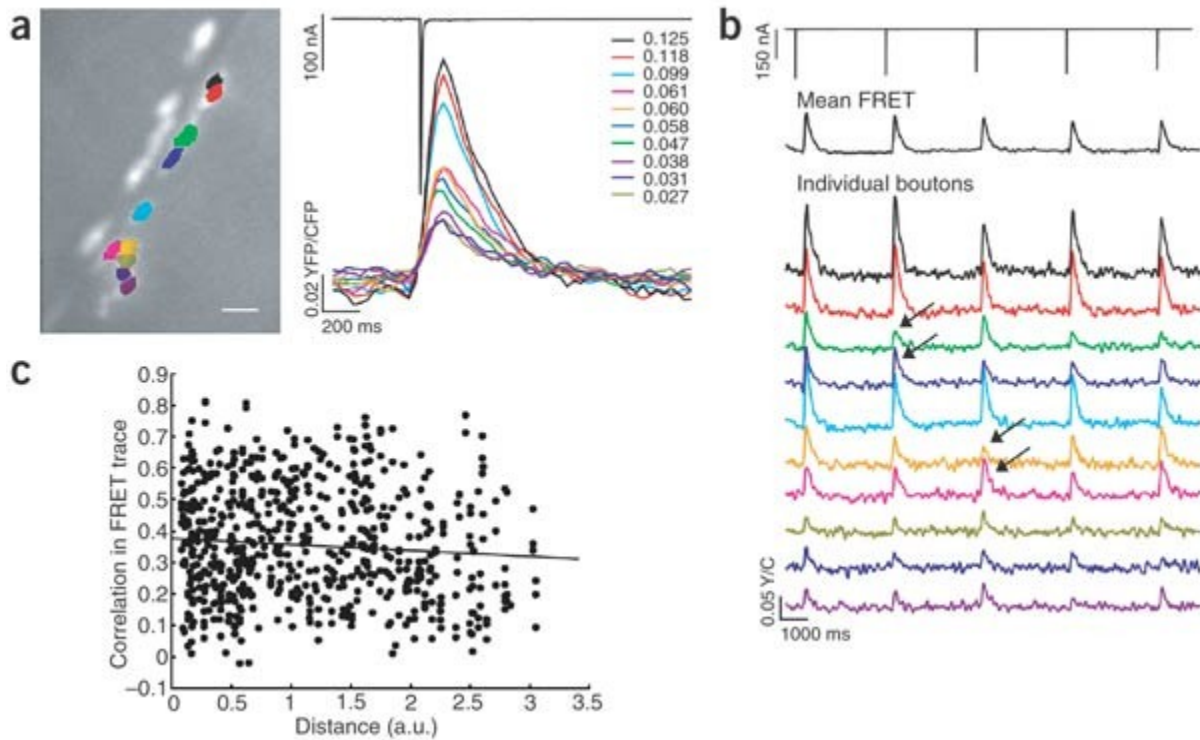
**Figure 2**
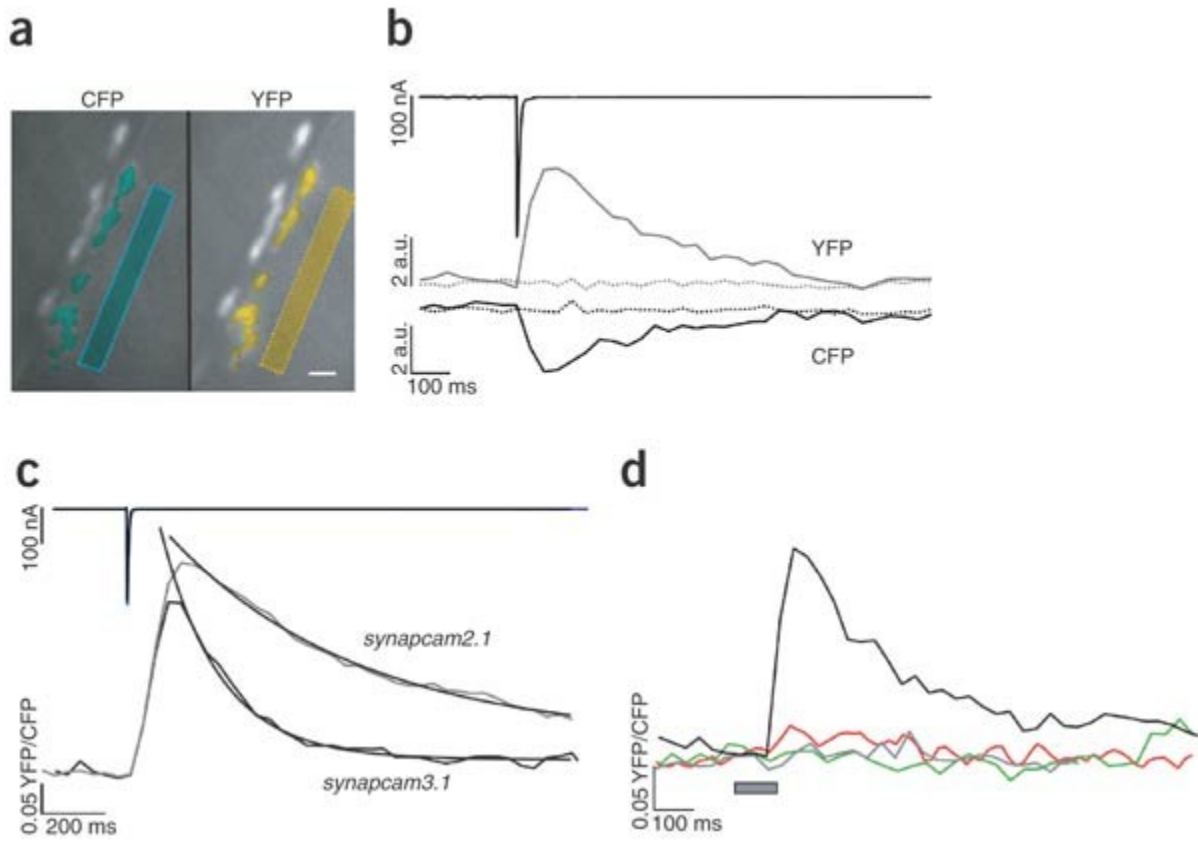
**Figure 2. Synapcams report Ca$^{2+}$ flux through GluRs as an increase in FRET.**

**(a)** An NMJ at muscle 6 during nerve stimulation. Synaptic and non-synaptic (boxes) areas expressing synapcam3.1 were selected for analysis (in blue for CFP and yellow for YFP). Scale bar: 10 μm. **(b)** The total fluorescence of synaptic regions showed reciprocal CFP (black traces at bottom) and YFP (gray) intensity changes following stimulation of the motor axon (EJC, black trace at top). Nonsynaptic areas (dotted lines) did not show fluorescent changes. Fluorescence levels for nonsynaptic areas were adjusted to synaptic levels for display purposes. a.u., arbitrary units. **(c)** Fluorescence changes were indicative of an increase in FRET between CFP and YFP upon synaptic transmission. Single stimuli to the motor axon evoked large FRET (YFP/CFP) changes measured from the entire synaptic area for both *synapcam3.1* (lower black trace, 16 NMJs) and *synapcam2.1* (gray, 13 NMJs). The *synapcam2.1* ΔFRET was on average 18% greater than the *synapcam3.1* response. FRET changes had a rapid onset (peak intensity reached after <200 ms) and a gradual offset, which was fit with a first-order exponential, with synapcam2.1 showing a slower decay lasting up to 2 s. **(d)** FRET increases (black, single response for the synapse in a) were induced by Ca$^{2+}$ transients, dependent on GluR activity, and synapcams did not report voltage-dependent Ca$^{2+}$ influx. The Ca$^{2+}$-insensitive synapcamNull showed no change in FRET (green, six NMJs). FRET changes were abolished upon application of desensitizing concentrations of glutamate (1.5 mM; red, three NMJs). A voltage step from -80 to 0 mV (gray bar) did not elicit a change in FRET (gray trace, three NMJs).
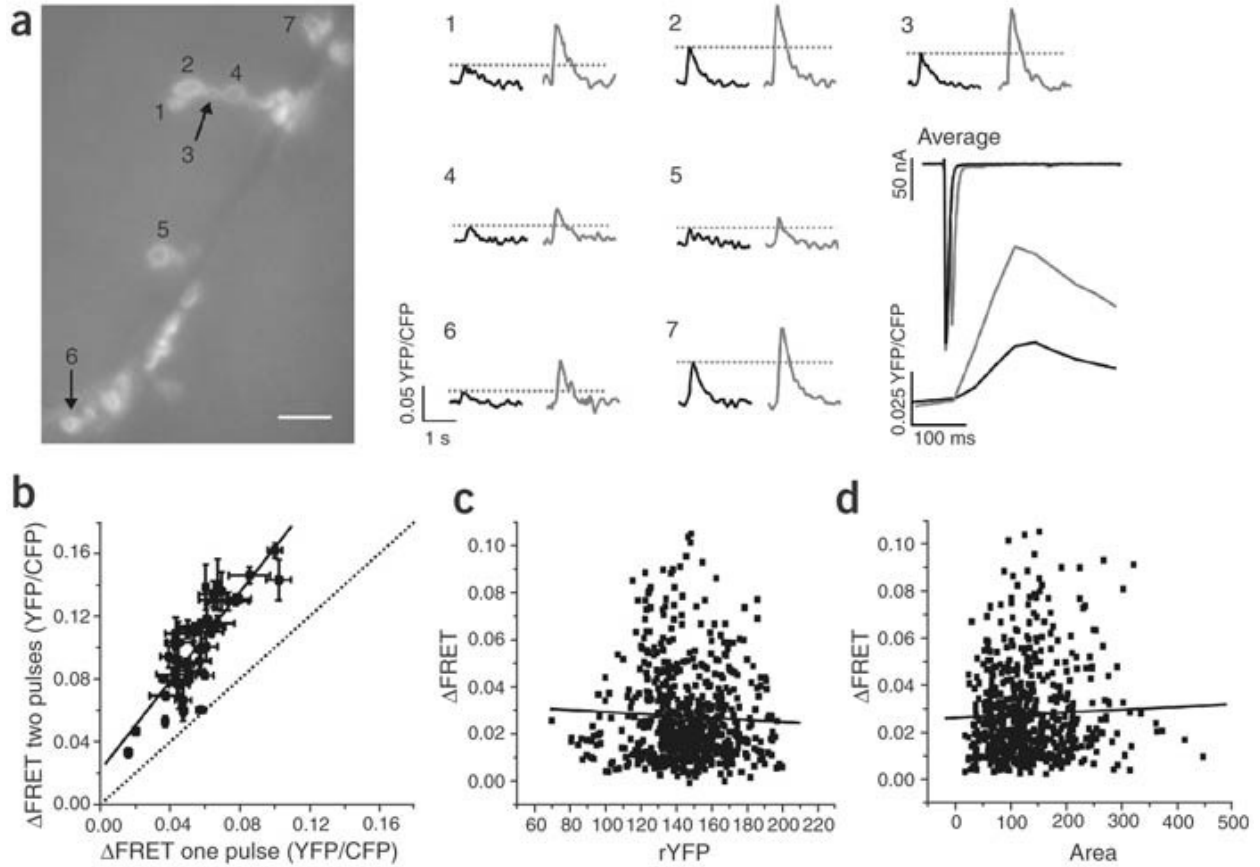
**Figure 3**



**Figure 3. Synapcam reveals transmission heterogeneity at the Drosophila NMJ.**
(**a**) Muscle sites postsynaptic to individual boutons were analyzed for $Ca^{2+}$-dependent FRET changes in response to a single motor axon stimulus. Each color represents a different postsynaptic region highlighted in the CCD image. The colors in the FRET trace at right correspond to the colors in the image at left. ΔFRET values for each region are shown. A 4.6-fold difference of ΔFRET magnitudes was observed for the NMJ displayed, with a mean difference of 5.3-fold for all experiments. Scale bar: 10 μm. (**b**) In addition to a small decrease in ΔFRET as a result of depression, small fluctuations (arrows) in the magnitude of ΔFRET were observed within single postsynapses upon repeated stimulation (0.25 Hz). These fluctuations however were not observed in the average response for the entire postsynapse (mean FRET trace, black). Fluctuations in ΔFRET were independent of the performance of other postsynapses despite physical proximity. For example, at two pairs of postsynapses (green and blue, or pink and yellow), FRET changes showed different fluctuation behavior, regardless of proximity. Therefore, the ΔFRET for a single postsynapse is not influenced by FRET changes at other postsynapse. (**c**) Comparison of FRET response for postsynapse pairs against the distance between pairs shows no correlation (156 trials, 61 boutons, six NMJs, $r = 0.009$). Distance is the pythagorean distance between postsynapse centers.

21

**Figure 4**



**Figure 4. Synapcam3.1 is not saturated by single stimuli to the motor axon.**
(**a**) Example NMJ that was subjected to trials of single stimulation (FRET responses are black traces) and trials where two stimuli were separated by 10 ms (gray traces). Although currents were depressed after the second pulse, the magnitude of ΔFRET was higher for dual stimulation recordings in all boutons imaged as a result of $Ca^{2+}$ summation in the synapcam response. Scale bar: 10 μm. Numbers identify single postsynapses. Numbers in image correspond with numbers above traces. (**b**) This increase was observed in all boutons of five NMJs tested. When compared with the response after a single pulse, the pooled responses for two stimuli showed on average an 83.1 ± 5.3% increase, and the responses were fit by linear regression ($r = 0.897$, $P < 0.0001$), indicating a lack of saturation, even for boutons that responded strongly to a single stimulus. ΔFRET numbers in **b** are the mean ± s.e.m. of three single stimulation and three double stimulation trials for each NMJ. (**c**) No correlation was found between the level of reporter expression, as assayed by the average resting levels of sensitized YFP (rYFP) and the FRET response of the postsynaptic terminal (black line: linear fit, $r = -10.047$, $P = 0.25$). (**d**) No correlation was observed between the size of a bouton and the FRET response (black line: linear fit, $r = 0.032$, $P = 0.33$). For **c** and **d**, $n = 625$ boutons and 45 NMJs.
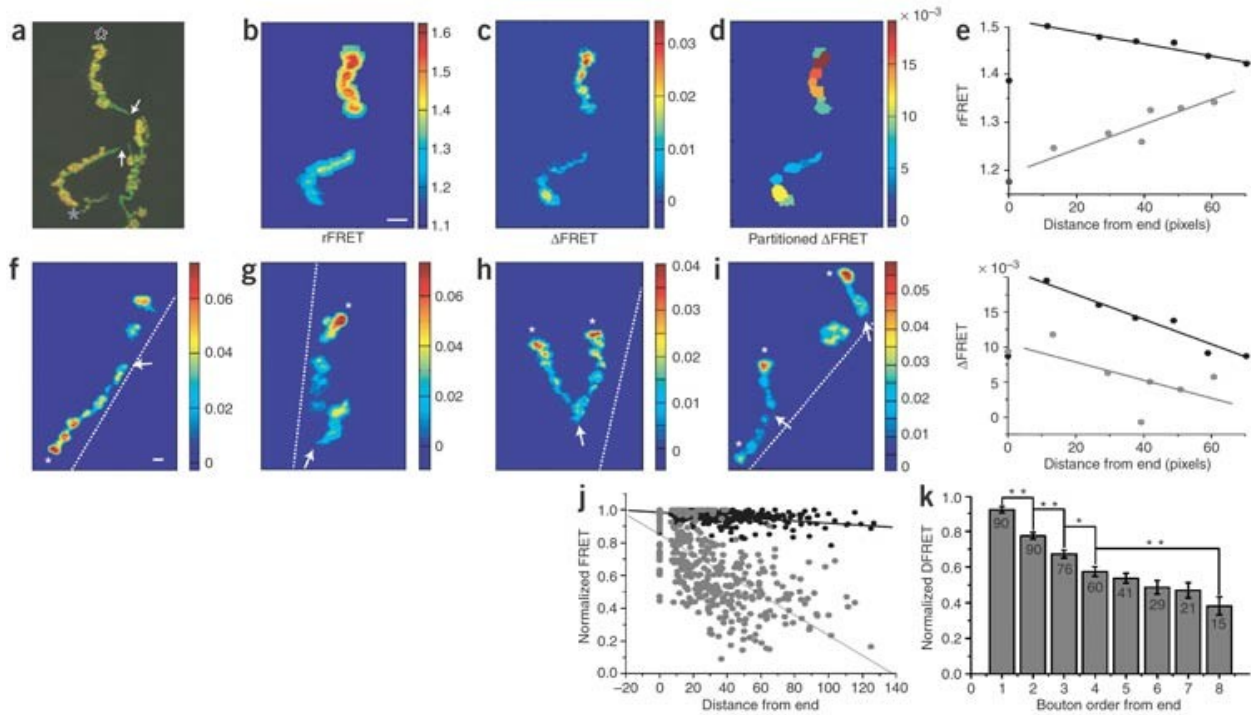
**Figure 5**
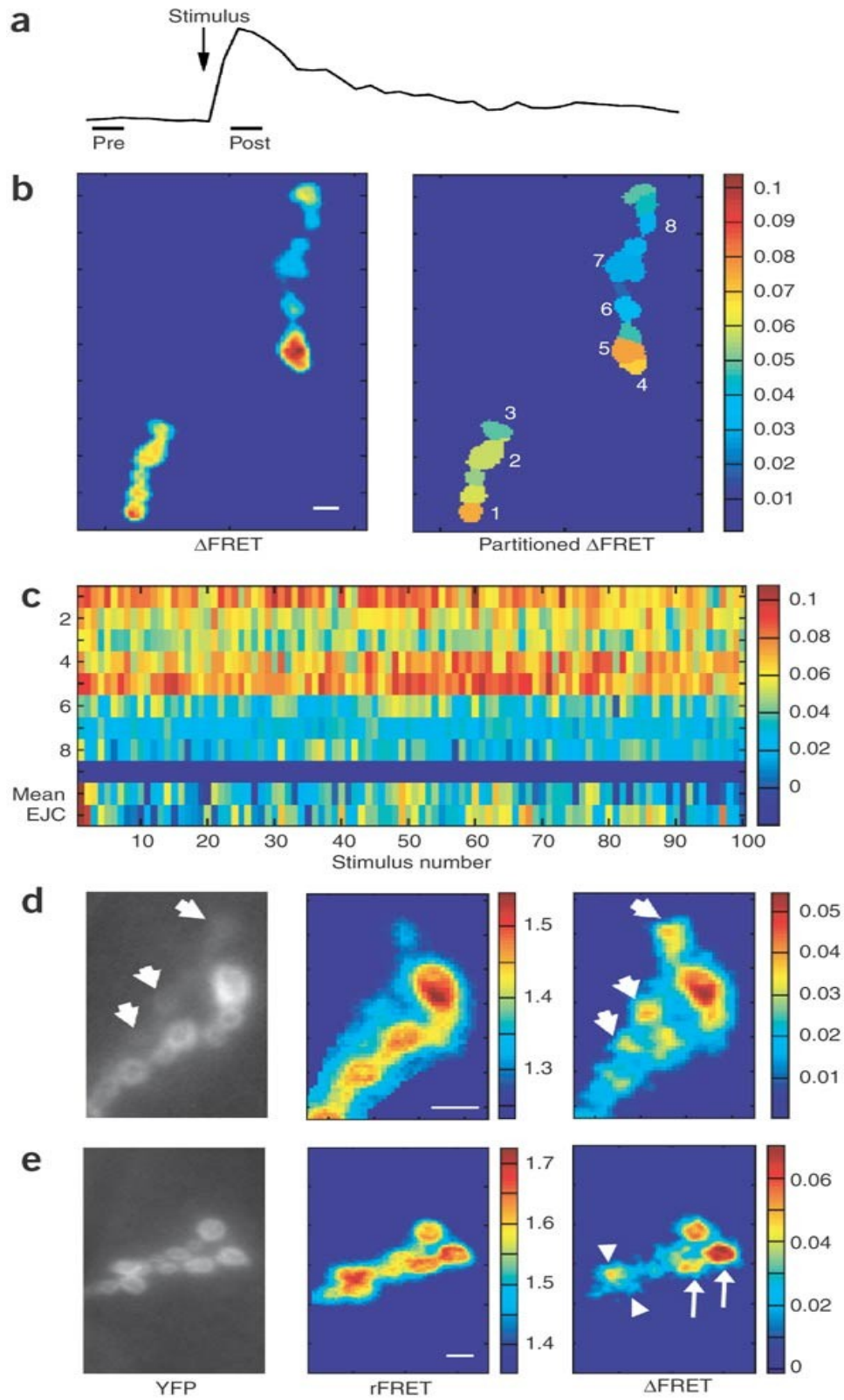
**Figure 5. Prolonged imaging shows the distribution of transmission strength of an NMJ.**

**(a)** Imaging conditions were optimized to allow extended imaging of the NMJ. One frame was acquired 200 ms before, and another 100 ms after nerve stimulation (0.125 Hz). Each frame represents 50 ms of exposure. The protocol was repeated for at least 30 trials, but more typically for 100−200 trials. **(b)** Image analysis produced mean ΔFRET scans of the entire synaptic region (left) and scans where the NMJ was partitioned into postsynaptic regions of interest with mean ΔFRET values for each postsynapse (right). **(c)** Array of 100 ΔFRET responses for the eight postsynapses numbered in b. The *y*-axis reflects postsynapse identity. The last two rows (separated by a blue bar) are mean ΔFRET for all postsynapses and EJC responses for each stimulus. (d,e) YFP, mean rFRET and mean ΔFRET images of two different NMJs. **(d)** FRET changes were sometimes observed for type Is postsynapses (short arrows), even though reporter localization at these sites was low (see YFP image). **(e)** Adjacent postsynapses of similar YFP and rFRET values frequently produced different FRET changes (two examples, white arrowheads and arrows) indicating that the mean ΔFRET of a postsynapse was not determined by reporter expression or rFRET values. The scale bar for all images is 8 μm.
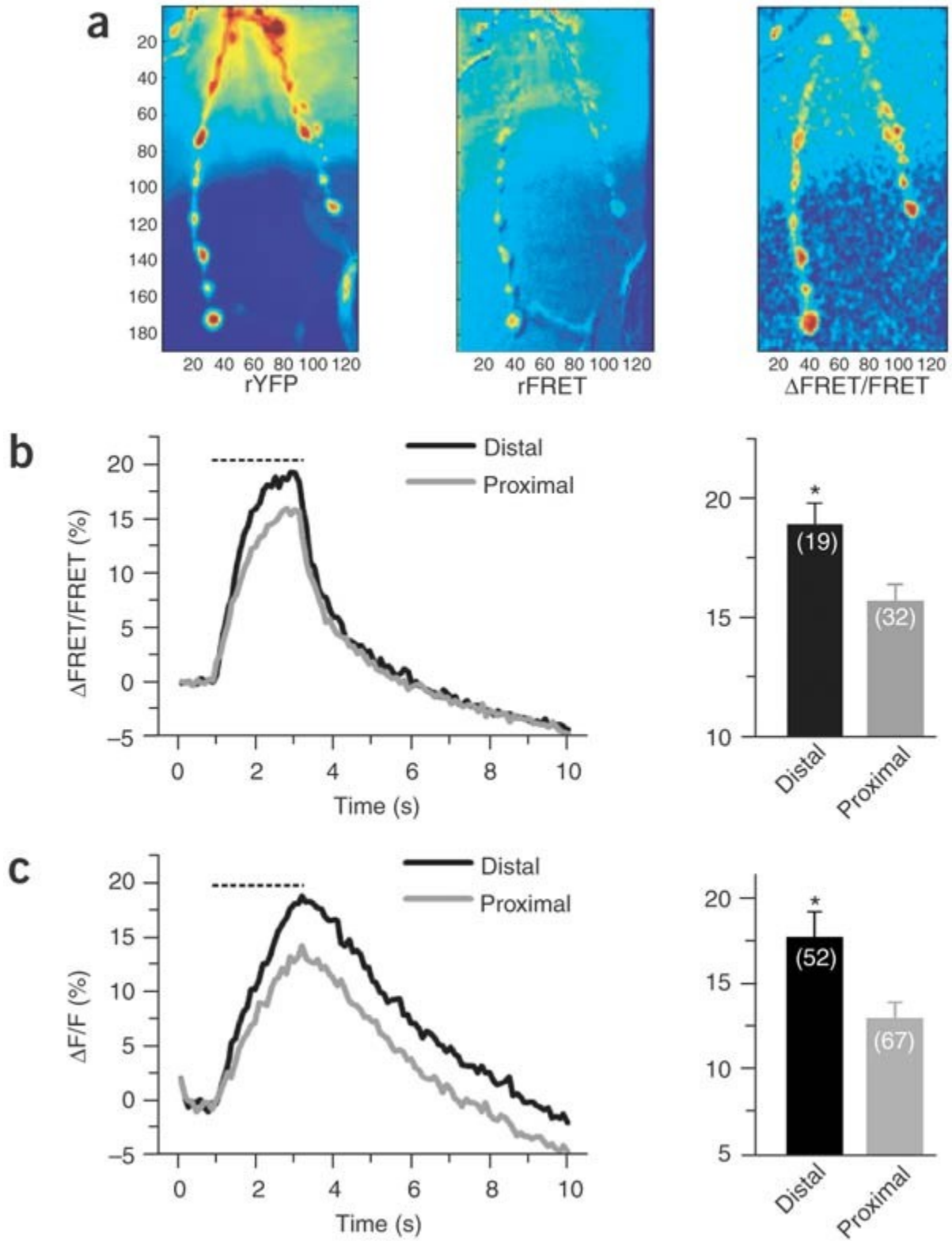
**Figure 6**



**Figure 6. A proximal-distal gradient in transmission strength.**
**(a)** HRP staining (green), overlaid on a synapcam3.1 YFP image (red), confirms the origin and termini of two branches (black and gray asterisks). **(b–d)** Mean rFRET **(b)**, mean ΔFRET **(c)** and ΔFRET partitioned and averaged within each synapse **(d)** for the NMJ in a. **(e)** Scatter plots of the mean rFRET (top) or ΔFRET (bottom) of each postsynapse against its distance from the end of a branch for the NMJ depicted in a–d. Black and gray corresponds to color of asterisks in a, and lines are fits to depict trend. **(f–i)** Additional examples of the transmission strength gradient along the length of axonal branches. Branch ends are marked with asterisks, branch origins are marked with arrows, and muscle border is depicted by a dashed white line. Color bars represent rFRET for b and ΔFRET for all other images. Scale bar for all images is 8 μm. **(j)** Pooled data of all postsynapses ΔFRET (gray) and rFRET (black) values against the distance from the branch's end show a stronger correlation for ΔFRET values. Linear fits, ΔFRET: $r = -0.649$, $P < 0.0001$; rFRET: $r = -0.461$, $P < 0.0001$. **(k)** Postsynapses at the branch end (first column) give on average greater ΔFRET than the postsynapses that follow them (to the right). Numbers within bars are number of postsynapses averaged, mean ± s.e.m., $^{**} P < 0.001$, $^{*} P < 0.005$ independent $t$-test. For j and k, FRET values were normalized to the highest value within each branch for $n = 440$ postsynapses, 90 branches, 34 NMJs.

**Figure 7**

**Figure 7. Presynaptic contribution to the gradient of transmission strength.**

(**a**) Axons expressing cytoplasmic Cam2.3 were subjected to 2.2 s of 40-Hz stimuli (dashed lines in **b** and **c**). Before stimulation, no axonal gradient was detected either in the amount of Cam2.3 at the synapse (rYFP) or the resting FRET (rFRET). However, during stimulation, boutons at the ends of axonal branches showed higher ΔFRET responses than more proximal boutons. (**b**) Average ΔFRET traces show higher presynaptic $Ca^{2+}$ increase for end boutons than for those 2−3 boutons away (ΔFRET/FRET = 18.95 ± 0.88 distal, 15.69 ± 0.73 proximal, $P < 0.005$, independent $t$-test). Data from 19 distal and 32 proximal boutons from19 axonal branches of seven NMJs. (**c**) Vesicle fusion was examined in animals expressing SpH and mDsRed (to aid in visualization of the axonal arbor) presynaptically. Distal boutons showed bigger fluorescent changes upon 40-Hz stimulation indicative of higher exocytosis (ΔF/F = 17.97 ± 1.49 distal, 13.20 ± 0.91 proximal; $P < 0.005$, independent $t$-test). Data from 52 axonal branches in 14 NMJs, including 52 distal and 67 proximal boutons.

# Chapter 2

# Specializations of a Pheromonal Glomerulus in the *Drosophila* Olfactory System

## Abstract

Insect pheromonal glomeruli are thought to track the fine spatiotemporal features of one or a few odorants to aid conspecific localization. However, it is not clear whether they function differently from generalist glomeruli, which respond to many odorants. In this study we test how DA1, a model pheromonal glomerulus in the fruit fly, represents the spatial and temporal properties of its input, in comparison to other glomeruli. We utilize a methodology that allows a simultaneous, unbiased comparison of the functional organization of many glomeruli. In contrast to what is found in other glomeruli, we find that ipsilateral and contralateral stimuli elicit distinct spatial patterns of activity within DA1. DA1 shows a greater preference for ipsilateral stimuli in males than in females. DA1 experiences greater and more rapid inhibition than other glomeruli, allowing it to report slight inter-antennal delays in stimulus onset in a   winner-take-all   manner. DA1's ability to encode spatiotemporal input features distinguishes it from other glomeruli in the fruit fly antennal lobe, but relates it to pheromonal glomeruli in other insect species. We propose that DA1 is specialized to help the fly localize and orient with respect to pheromone sources.

## Introduction

The antennal lobe is a brain network that guides olfactory behaviors in insects. It is partitioned into globular neuropil called glomeruli, each of which responds to a unique set of odorants. Glomeruli can be classified as generalists or specialists based on the selectivity of their responses. The majority of glomeruli are generalists; they respond to many odorants, and their population activity can combinatorially encode a large variety of odorants. Interactions between glomeruli of the generalist subsystem may aid the computation of odor identity, robust to variations in odor concentration and the presence of background odors (Stopfer et al., 2003; Brody and Hopfield, 2003). In contrast, some glomeruli are specialists; when activated by specific chemicals, they can trigger innate behaviors (Suh et al., 2004). One well-studied class of specialist glomeruli responds to pheromones, chemicals emitted by individuals that serve as species-specific social cues. A large part of a male insect's olfactory system may be devoted to processing a small number of pheromones, hinting at the unique challenges faced by this system (King et al., 2000). By encoding spatial (Ai and Kanzaki, 2004; Heinbockel and Hildebrand, 1998) and temporal (Lei et al., 2009) variations in odor concentration, the pheromonal subsystem may aid odor source localization over potentially long distances in turbulent environments (Vickers et al., 2001). Thus, odor processing by pheromonal and generalist glomeruli may exhibit fundamental differences; however, the physiological underpinnings of such differences remain to

be identified. Indeed, the structural and functional similarities in the circuitry of the two subsystems bring into question the utility of this dichotomy (Christensen and Hildebrand, 2002).

In this study, we explicitly assess the functional specialization of DA1, a model pheromonal glomerulus in *Drosophila melanogaster*. Unlike most glomeruli in the fruit fly AL, DA1 responds selectively to a single odorant, the male pheromone cis-vaccenyl acetate (cVA) (Ha and Smith, 2006; Schlief and Wilson, 2007). This simple response profile is contrasted by a greater anatomical complexity: while most glomeruli are innervated by ~2-3 similar projection neurons (PNs), the output cells of the antennal lobe, DA1 is innervated by ~8 PNs with distinctive features (Marin et al., 2002). The projection pattern of the axons of these PNs differs between males and females, possibly relating to the sex-specific behaviors elicited by cVA (Datta et al., 2008).

We compare the response properties of DA1 to those of generalist glomeruli, in the context of mechanisms that may aid source localization. We combine electrical stimulation and calcium imaging to probe activity throughout the antennal lobe, enabling an unbiased comparison across a large population of glomeruli. We find that DA1's unique input organization and inhibitory circuitry enable it to discriminate fine spatial and temporal variations in its input. DA1 recapitulates the defining features of pheromonal glomeruli found in other insects, and these features distinguish DA1 from generalist glomeruli within the fruit fly antennal lobe. Our findings support the view that pheromonal and generalist subsystems process their inputs differently.

## Methods

### Fly lines

Flies expressing UAS-GCaMP 1.6 (Reiff et al., 2005) on the $2^{nd}$ chromosome were crossed with GH146-Gal4 (for PNs) and OR83b-Gal4 (for ORNs). Flies were homozygous for both Gal4 and UAS constructs. For experiments comparing pre vs. postsynaptic activity (Fig. 3C and Suppl Fig. 3), flies expressed both GH146 and OR83b-Gal4.

### Recordings

1-3 day old flies were briefly anesthetized with $CO_2$ and decapitated. Imaging was done on an isolated brain preparation (Wang et al., 2003). Antennae were cut with micro-scissors (FST) and cuticle was pulled apart with a pair of forceps. Dissection was done in saline with .1 mM $Ca^{++}$ (adapted from (Silbering and Galizia, 2007). Brain was transferred to a glass slide with .5 mL 2mM $Ca^{++}$ saline (Silbering and Galizia, 2007). The anterior surface of the brain faced upward and the brain was lightly pressed with forceps so that it adhered to the glass. Glass pipettes were

pulled with a micropuller (Sutter) and fire-polished to match the diameter of the antennal or maxillary nerve. Pipettes were secured onto electrode holders that were attached to micromanipulators. Electrical stimuli were delivered using a Master-8 stimulator (AMPI, Jerusalem, Israel), triggered by pClamp software. Acquisition was triggered on a Zeiss LIVE confocal microscope. Frame rate was 20Hz, with a 488 nm diode laser and a 495 nm long-pass filter. Objective was 60x, .95NA.

Two nerves (either 2 antennal or 1 antennal and 1 maxillary nerve) (Fig. 1) were suctioned into 1 electrode each. Care was taken to have both antennal lobes visible at a similar cross-sectional depth; suction electrodes were slightly adjusted in the z-direction if needed to achieve this. Stimuli were .1-.3 ms, 10V electrical pulses. Pulse trains were 100 Hz. Inter-trial interval was 30s; each trial consisted of a 1.5-second acquisition, stimuli being presented at .5 sec. For stimulation of ventromedial glomeruli (Fig. 6Cii), ventromedial neuropil was suctioned into electrode and stimulated with a single 10V, .4 ms pulse. This resulted in selective, bilaterally symmetric activation of ventromedial glomeruli, due to the activation of bilaterally projecting ORNs.

**Pharmacology**

Excitation was blocked using 40 uM mecamylamine (Kazama and Wilson, 2008). Stock solution was 10mM in 10% DMSO. GABAa was blocked using 20 uM picrotoxin; GABAb was blocked using 50 uM CGP54626 (Wilson and Laurent, 2005). Drugs were added to preparation with a micropipette, taking care not to move the preparation. There was a 5-minute wait before acquisition was resumed.

To isolate pre- and postsynaptic activity within a single preparation, brains from UAS-G-CaMP1.6,GH146-Gal4;OR83b-Gal4 flies were stimulated with a single pulse to evoke a postsynaptic response. Under normal conditions, this protocol minimally evokes a change in presynaptic fluorescence. This was proceeded by a blockade of excitation using mecamylamine. This prevented activation of PNs as well as inhibitory circuitry, disinhibiting the presynaptic response. A 30-pulse, 100 Hz stimulus was then used to evoke presynaptic activity.

**Map generation**

LSM image stacks were imported into Matlab using DIPimage (www.diplib.org). To make maps of evoked activity, the average of 10 frames post-stimulus was subtracted from the average 10 frames pre-stimulus (Fig. 1D). To remove the effect of dark-state conversion of G-CaMP1.6 that occurs during illumination, the resultant map was subtracted from a control map generated for a no-stimulus condition. To correct for drift of preparation between trials, each antennal lobe was aligned to the resting fluorescence image from the initial trial using DIPimage. All ΔF/F images

shown in figures were processed as such: 1) the region surrounding glomeruli is masked to eliminate background noise from image, and 2) image is smoothed with a gaussian filter, $\sigma = .75\text{-}1$ pixels.

**Analysis**

For ROI analysis, glomeruli were manually selected. They were identifiable in activation maps as contiguous, round regions of relatively uniform intensity. DA1 was identifiable by its distinct morphology and location in the dorsolateral region. To generate average maps of activity across preps, each AL was morphed into a 300-point circle consisting of 10 radial and 30 angular coordinates (Suppl. Fig. 1). Each pixel was binned according to its distance from the boundary of the antennal lobe, and its angle from the center of the antennal lobe. Bins were averaged and plotted in polar coordinates  and interpolated to generate a smoothed, circular map (using PolarToIm.m, posted on Matlab Central by P. Manandhar).

To enhance color contrast of two-color images (e.g. Fig. 2B), each pixel was assigned a z-score (# standard deviations from the mean) corresponding to the log ratio of intensities in the two channels. This ratio was exaggerated using the hyperbolic tangent function and was used to generate new values for the two channels, keeping the cumulative intensity across the two channels constant (Suppl. Fig. 2).

To calculate the difference in spatial extent of activation by ipsilateral vs. contralateral stimulation (e.g. Fig. 2D) for a given glomerulus, we calculated the mean distance of pixels from the center of the response, weighted by the per-pixel $\Delta F/F$, for both ipsilateral and contralateral stimulation. We used this to calculate $\Delta$Extent, the log ratio of ipsilateral extent to contralateral extent. To generate figure 2D, $\Delta$Extent was calculated and assigned to the entire ROI of each glomerulus. The resulting maps were then standardized (Suppl. Fig. 1) and combined to generate an average map.

To determine DA1 boundaries within average maps (e.g. Fig. 2D), DA1 was manually identified in single preparations and its region of interest was assigned a value of 1. The resulting maps were standardized (Suppl. Fig. 1), averaged, and the region whose intensity exceeded 50% of maximum was demarcated as DA1 within average maps. Regions activated by local stimulation (Fig. 6C) were delineated by generating average maps of responses to local stimulation, and thresholding the resultant map at 50% of maximum response. To visualize the medial region activated by maxillary nerve stimulation (Fig. 6Ci), a threshold of 30% was needed.

To plot PN response in time (Fig. 7, Suppl. Fig. 6), the time course of the average fluorescence in a region of interest was bleach-corrected by subtracting time course of fluorescence in a no-

stimulus control movie. The resultant trace was normalized and deconvolved with an exponential with a time constant τ = 363 ms, the time constant of fluorescence decay calculated in PNs in response to a single pulse. This corrected for the slow decay intrinsic to the response of GCaMP 1.6.

To test significance, the two-tailed, two-sample t-test was used; the one-sample (paired) t-test was used when the comparison utilized pairs of measures taken from the same sample (Figs. 4D, 5B, 6D, 7C).

## Results
### DA1 Encodes Spatial Information
The bilateral comparison of olfactory stimuli aids source localization in many species (Porter et al., 2007; Rajan et al., 2006), including fruit flies (Borst and Heisenberg, 1982; Duistermars et al., 2009). Most glomeruli in the fruit fly antennal lobe are innervated by olfactory receptor neurons (ORNs) originating from both the ipsilateral and contralateral antennae (Stocker et al., 1990). We investigated how these two ORN populations activate DA1 and other glomeruli by visualizing the response to electrical stimulation of either the left or the right antennal nerve (Fig. 2A). We imaged either presynaptic activity in ORN terminal axons (Fig. 2B), or postsynaptic activity in PN dendrites (Fig. 2C). The responses of ventro-lateral glomeruli, in ORNs as well as in PNs, were largely ipsilateral (Fig. 2B,C; Suppl. Fig. 3A). The rest of the glomeruli responded bilaterally: imaging the ORN terminal axons of these glomeruli revealed interlaced regions that responded to either ipsilateral or contralateral stimulation (Fig. 2B).

Unlike their input population, the PNs of each bilaterally responsive glomerulus exhibited virtually identical spatial patterns of activity in response to ipsilateral and contralateral stimulation (Fig 2C, white regions; Suppl. Fig. 4). However, this was not the case for the PN population innervating DA1; ipsilateral stimulation activated a larger region within this glomerulus than did contralateral stimulation (Fig. 2D). The appearance of distinct spatial patterns within DA1 is not simply a byproduct of DA1's large size, as this property is also apparent in DL3 (arrowheads in Fig. 2C, D), a smaller, cVA-responsive pheromonal glomerulus (van der Goes van Naters and Carlson, 2007) dorsal to DA1.

The larger spatial extent of ipsilateral activation within DA1 PNs complements the distribution of ORN inputs, which exhibit a concordant difference in spatial extent (Suppl. Fig. 5). For other glomeruli, the spatial extent of the activation by the two sides was much more similar in ORNs and was identical in PNs (Suppl. Fig. 3B). We aligned 16 DA1's mapped to polar coordinates and plotted the average relative response of each subregion (30 angular x 10 radial bins; see Image Analysis section in Methods) to ipsilateral and contralateral stimuli. The ventro-medial region

had a relatively large response to ipsilateral stimulation, while a more contralaterally-responsive region was centered on a dorso-lateral locus (Fig. 2F).

Thus, DA1 PNs respond differentially to activation of ORNs originating from the left and right antennae, a feature not seen in the PNs of generalist glomeruli.

**DA1's Spatial Response is Sexually Dimorphic**
Since DA1 activation triggers sex-specific behaviors in Drosophila (Kurtovic et al., 2007), we looked for differences in the side-specific responses of male and female DA1s. In males, DA1 had a stronger response to ipsilateral stimulation (Fig. 3A), while female DA1's showed similar magnitudes of response to ipsilateral and contralateral stimulation (Fig. 3B), and in some cases an even stronger response to contralateral stimulation (e.g. female AL in Fig. 2C). This difference could not be explained by the relative density of presynaptic innervation, since both male and female DA1 ORN responses were largely ipsilateral (Fig. 3C).

The difference between males and females in ipsilateral preference of DA1 PNs was seen across the range of stimulus durations tested. Longer trains resulted in a greater ipsilateral preference in both males and females, in DA1 as well as in other glomeruli (Fig 3D). This was the result of the ipsilateral response having a sustained component to prolonged stimuli that was absent in contralateral responses (Suppl. Fig. 6). The sexual dimorphism in ipsilateral bias seen in DA1 was small or undetectable in other glomeruli (Fig. 3D, Suppl. Fig. 7).

**DA1's Responsivity Rapidly Decreases Upon Activation**
The ability of pheromonal PNs to report rapid fluctuations in odor concentration is critical for localizing odor sources (Lei et al., 2009). We therefore investigated the specialization in the response dynamics of DA1 PNs relative to the PNs of other glomeruli. The activation of ORNs triggers excitatory and inhibitory interactions within and among glomeruli that together transform the output of PNs (Olsen et al., 2007; Olsen and Wilson, 2008). We developed a protocol to measure the net impact of circuit interactions on PN excitability in the moments following initial activation. We stimulated one antennal nerve to activate excitatory and inhibitory neurons across the antennal lobe, and then stimulated the contralateral nerve with varying delays to map time-sensitive variations in the ability of the ORNs to excite the PNs in wake of the prior stimulation (Suppl. Fig. 8, Movie S1). Introducing a delay in the $2^{nd}$ pulse attenuated its contribution to the total evoked response, due to the predominance of inhibition evoked by the $1^{st}$ pulse (See below). We visualized this attenuation within different glomeruli by superimposing the response to simultaneous inputs and 25-ms-staggered inputs (Fig. 4B, C). Compared to other glomeruli, DA1 showed a decrease in its response to stimuli delayed by as little as 5 ms (Fig. 4D); this decrease was more than 4x larger for a delay of 25 ms. Plotting the

33

per-pixel response to simultaneous vs. staggered inputs showed linear distributions of pixels belonging to DA1 or neighboring glomeruli (Fig. 4E). The linear and bimodal clustering of these pixels indicates that the decrease is uniform and confined within DA1.

## GABA-a Mediates Rapid Inhibition in DA1

In moths, the ability to track pheromone dynamics relies on GABAergic inhibition (Lei et al., 2009), an interaction that is pronounced in the fruit fly antennal lobe (Root et al., 2008; Olsen and Wilson, 2008). We pharmacologically assessed how GABA shapes the spatiotemporal response properties of DA1 PNs. Block of either GABA-a or GABA-b receptors increased the response of DA1 PNs (Fig. 5D); normalizing these responses allowed us to assess how each pathway shaped the temporal dynamics of input integration in DA1. Block of GABA-a receptors eliminated the relatively rapid decrease in DA1's responsivity (Fig. 5A, B), unmasking an excitatory interaction that peaked at the 10 ms inter-pulse interval. Interestingly, removing fast inhibition induced a complementary increase in late-phase inhibition (Fig. 5A), suggesting a greater activation of inhibitory local neurons. Block of GABA-b receptors decreased the late phase of the delay-dependent response attenuation, although the effect was variable enough as to not be statistically significant for any single time point (p = .055 at 250 ms inter-pulse interval) (Fig. 5A). Only fast GABA-a inhibition shaped the spatial extent of DA1 activation (Fig. 5C). This was apparent in the distribution of activity along the proximal-distal axis (relative to PN output, see Fig. 5C) of DA1 PN dendrites. Whereas the activity profile scaled linearly upon blocking GABA-b receptors, GABA-a receptor block preferentially disinhibited the proximal dendrites of DA1 PNs (Fig. 5D). The results show that fast inhibition is evoked strongly and rapidly enough to restrict the spread of activity, as well as the influence of slow inhibition, within the PNs of DA1.

## Intra-glomerular Inhibition in DA1

The greater inhibition that we find in DA1 could arise from intra-glomerular or inter-glomerular interactions, both of which would be triggered by our antennal nerve stimulation protocol (Fig. 4A). To localize the origin of DA1's inhibition, we delivered the initial stimulus to the maxillary nerve instead of the antennal nerve (Fig. 6A). Since the two nerves activate different sets of glomeruli (Rajashekar and Shamprasad, 2004), any decrease in DA1's response should result exclusively from inter-glomerular inhibition. Comparing the response to simultaneous vs. staggered stimulation of the two nerves revealed a dorso-ventral strip of glomeruli down the middle of the AL that experiences greater inhibition (magenta region, Fig. 6B). Medial and lateral glomeruli, including DA1, received relatively small (but significant) amounts of inhibition (Fig. 6Ci). Blockade of GABA-a receptors further increased the lateral inhibition triggered by maxillary nerve stimulation (consistent with the effect seen in Fig. 5A), but once again, DA1 was among the least inhibited (Suppl. Fig. 9).

To make sure that this pattern of lateral inhibition does not result specifically from the activation of maxillary glomeruli, we measured the inhibition resulting from the direct stimulation of ventromedial glomeruli. Both maxillary nerve stimulation and ventromedial neuropil stimulation revealed similar distributions of lateral inhibition; each protocol evoked the greatest inhibition in dorsal glomeruli but relatively weak inhibition in DA1 (compare Fig. 6Ci and ii). This contrasts with the greater inhibition DA1 experiences upon antennal nerve stimulation (Fig. 6D), indicating that the strong and rapid inhibition of DA1 that we measured previously is largely intra-glomerular.

**DA1 Discriminates Direction of Stimulus Onset**

One cue that enables odor localization in several species is the sequence in which an odor plume comes into contact with spatially separated sensors (Rajan et al., 2006; von Bekesy, 1964). Responding to this cue requires that an animal make a persistent decision that far outlasts a potentially transient difference in sensor activation. We tested the ability of DA1 to report such brief temporal asymmetries in the activation of inputs originating from the left and right antenna. We stimulated each nerve with a 100 Hz train for .3 s (Fig. 7A), a frequency and duration within the range of ORN responses to naturally occuring odor plume filaments (van der Goes van Naters and Carlson, 2007; Justus et al., 2002), and introduced varying delays in the onset of right nerve stimulation. With a relative delay of only 25 ms, less than one tenth of the total stimulus duration, the pattern of activity in left and right DA1's resembled the pattern evoked by stimulating the left nerve alone *(*Fig. 7B). We quantified this with the spatial correlation between the response to paired stimulation and that of stimulating either nerve alone (Fig. 7C). For delays of 25 ms or more, the later stimulus contributed minimally to the final spatial pattern of activity. This can be seen in the time course of activity following dual-nerve stimulation; activation of DA1 by the left nerve strongly and rapidly inhibits the transient evoked by right nerve stimulation (Fig. 7D). This would allow DA1 to  capture relative delays in stimulus onset between the two antennae (Movie S2).

**Discussion**

The anatomy and ethology of pheromonal and generalist subsystems suggest that they process inputs uniquely. However, to our knowledge, their response properties have never been directly compared before. We characterize functional differences among glomeruli of the fruit fly antennal lobe, focusing on the specialization of the pheromonal glomerulus DA1. We find that the organization of inputs and inhibitory interactions in DA1 are distinct from those in other glomeruli. DA1's properties enable it to discriminate the direction of odor onset, suggesting that DA1 is specialized to localize odor sources.

Most glomeruli in the *Drosophila* AL are generalists that are strongly coupled via a network of lateral excitatory (Olsen et al., 2007; Shang et al., 2007) and inhibitory connections (Olsen and Wilson, 2008). These glomeruli appear to function as an ensemble that increases the contrast between responses to chemically distinct odorants (Bhandawat et al., 2007), a property that may assist odor classification. DA1, on the other hand, exhibits no excitatory coupling to other glomeruli (Schlief and Wilson, 2007) and minimal inhibitory coupling, as we show here (Fig. 6). Instead, DA1 discriminates fine-scale spatial features of a single odorant, cVA.

We find different zones of activity within DA1 corresponding to ipsilateral and contralateral inputs. Can different spatial patterns within DA1 be discriminated by downstream circuits and ultimately inform behavior? Glomeruli are commonly treated as a monolithic unit of olfactory input (Wachowiak et al., 2004). Indeed, the organization of many *Drosophila* glomeruli prevents them from discriminating the spatial identity of activated ORNs (Gouwens and Wilson, 2009; Kazama and Wilson, 2008). Nonetheless, for several insect species, pheromonal ORNs (Christensen et al., 1995) and PNs (Hösl, 1990) restrict their processes to subregions of the glomerulus in a manner that corresponds to their spatial receptive fields along the antenna. Unlike other *Drosophila* glomeruli, DA1 is non-uniformly innervated by several types of PNs with unique arborizations (Marin et al., 2002). In light of this, our findings suggest that the activation of ipsilateral and contralateral ORNs induces unique patterns of activity across the PN population innervating DA1.

Sensing variations in the activity of spatially separated ORNs may help insects to localize pheromone sources. However, it is unclear how the structure and salience of the fruit fly pheromonal plume compare to those of much larger pheromonal models, such as moth. While fruit flies use bilateral information to orient towards an odor source (Duistermars et al., 2009; Borst and Heisenberg, 1982), the small separation of their antennae (~.2 mm) may not accommodate the long-range navigational cues available to more widespread sensors (Webster et al., 2001). For DA1 to discriminate the directionality of an odor plume, the plume's lateral velocity relative to the fly's head would need to be less than ~1 cm/s (.2 mm inter-antennal spacing $\div$ 25 ms inter-antennal delay detectable by DA1), more than an order of magnitude slower than the velocities encountered in anemotactic orientation during *Drosophila* free flight (Budick and Dickinson, 2006). One possibility is that spatiotemporal variations in cVA concentration are useful in orienting the fly to short-range mating cues. DA1 activation stimulates mating in females but suppresses it in males (Kurtovic et al., 2007). The sexual dimorphism we see in DA1's response to contralateral stimuli may support differences in how males and females orient to cVA-emitting sources.

We found that DA1's responsivity and spatial spread of the response through the PN dendrites

36

were strongly suppressed within 25 ms of initial activation due to fast GABA-a mediated inhibition. A previous study found relatively high expression of GABA-b receptors in DA1 (Root et al., 2008); our findings suggest that fast inhibition can limit the extent to which these receptors are activated. We found that a relatively small part of DA1's inhibition is inter-glomerular. This is consistent with the observation that many of the inhibitory local neurons that interconnect the AL avoid pheromonal glomeruli (Wilson and Laurent, 2005). While we did not comprehensively assess DA1's interactions with all other glomeruli, lateral inhibition appears to largely reflect the cumulative activation of ORNs, independent of their glomerular identity (Olsen and Wilson, 2008). Given the significance of pheromonal blends in *Drosophila* (Griffith and Ejima, 2009) and other species (Christensen and Hildebrand, 1997), (Anton and Hansson, 1996), it will be important in future work to probe interactions between DA1 and its neighboring pheromonal glomeruli.

Mutual inhibition between pairs of glomeruli with identical odor tuning is widespread, from precisely connected maps in the olfactory bulb (Lodovichi et al., 2003; Yan et al., 2008), to antiphasic 'flip-flop' activity in the left and right pheromonal centers in moths (Mishima and Kanzaki, 1999). The strong mutual inhibition of ipsi- and contralateral ORNs we see within DA1 allows the discrimination of slight differences in onset of activity across inputs. This is even true for prolonged inputs: an activated input simultaneously establishes a spatial pattern of activity and minimizes the impact of future inputs on DA1, preventing the modification of the initial pattern. This behavior is characteristic of winner-take-all networks (Coultrip et al., 1992), which settle on one of several possible activity patterns based on an initial asymmetry. Thus, a transient difference in activity between the two antennae could serve as a persistent orientation cue (Movie S2).

In conclusion, we propose a dual relationship between DA1 and other glomeruli. DA1 exhibits specializations in spatial and temporal processing of inputs that distinguish it from other glomeruli in the *Drosophila* AL. These specializations indicate that DA1 shares organizing principles with pheromonal glomeruli in other insect species. It remains to be seen how these specializations are adapted to meet the challenges specific to the fly's pheromonal environment. An understanding of DA1's computations will benefit from exploiting the analytic power of the fruit fly genetic model in the context of the rich methodologies developed to explore the structures, functions, and behaviors in classical models of pheromone perception.

## References

Ai H, Kanzaki R  (2004)  Modular organization of the silkmoth antennal lobe macroglomerular complex revealed by voltage-sensitive dye imaging. J. Exp. Biol 207:633-644

von Bekesy G  (1964)  Olfactory analogue to directional hearing. J Appl Physiol 19:369-373

Benton R  (2007)  Sensitivity and specificity in Drosophila pheromone perception. Trends Neurosci 30:512-519

Bhandawat V, Olsen SR, Gouwens NW, Schlief ML, Wilson RI  (2007)  Sensory processing in the Drosophila antennal lobe increases reliability and separability of ensemble odor representations. Nat. Neurosci 10:1474-1482

Borst A, Heisenberg M  (1982)  Osmotropotaxis in Drosophila melanogaster. Journal of Comparative Physiology A: Neuroethology, Sensory, Neural, and Behavioral Physiology 147:479-484

Brody CD, Hopfield JJ  (2003)  Simple networks for spike-timing-based computation, with application to olfactory processing. Neuron 37:843-852

Budick SA, Dickinson MH  (2006)  Free-flight responses of Drosophila melanogaster to attractive odors. J. Exp. Biol 209:3001-3017

Christensen TA, Harrow ID, Cuzzocrea C, Randolph PW, Hildebrand JG  (1995)  Distinct projections of two populations of olfactory receptor axons in the antennal lobe of the sphinx moth Manduca sexta. Chem. Senses 20:313-323

Christensen TA, Hildebrand JG  (2002)  Pheromonal and host-odor processing in the insect antennal lobe: how different? Curr. Opin. Neurobiol 12:393-399

Coultrip R, Granger R, Lynch G  (1992)  A cortical model of winner-take-all competition via lateral inhibition. Neural Networks 5:47   54

Datta SR, Vasconcelos ML, Ruta V, Luo S, Wong A, Demir E, Flores J, Balonze K, Dickson BJ, Axel R  (2008)  The Drosophila pheromone cVA activates a sexually dimorphic neural circuit. Nature 452:473-477

Duistermars BJ, Chow DM, Frye MA (2009) Flies require bilateral sensory input to track odor gradients in flight. Curr. Biol 19:1301-1307

van der Goes van Naters W, Carlson JR (2007) Receptors and neurons for fly odors in Drosophila. Curr. Biol 17:606-612

Gouwens NW, Wilson RI (2009) Signal propagation in Drosophila central neurons. J. Neurosci 29:6239-6249

Ha TS, Smith DP (2006) A Pheromone Receptor Mediates 11-cis-Vaccenyl Acetate-Induced Responses in Drosophila. J. Neurosci. 26:8727-8733

Heinbockel T, Hildebrand JG (1998) Antennal receptive fields of pheromone-responsive projection neurons in the antennal lobes of the male sphinx moth Manduca sexta. J. Comp. Physiol. A 183:121-133

Hösl M (1990) Pheromone-sensitive neurons in the deutocerebrum of Periplaneta americana: receptive fields on the antenna. Journal of Comparative Physiology A: Neuroethology, Sensory, Neural, and Behavioral Physiology 167:321-327

Justus KA, Murlis J, Jones C, Cardé RT (2002) Measurement of Odor-Plume Structure in a Wind Tunnel Using a Photoionization Detector and a Tracer Gas. Environmental Fluid Mechanics 2:115-142

Kazama H, Wilson RI (2008) Homeostatic matching and nonlinear amplification at identified central synapses. Neuron 58:401-413

Kurtovic A, Widmer A, Dickson BJ (2007) A single class of olfactory neurons mediates behavioural responses to a Drosophila sex pheromone. Nature 446:542-546

Lei H, Riffell JA, Gage SL, Hildebrand JG (2009) Contrast enhancement of stimulus intermittency in a primary olfactory network and its behavioral significance. J. Biol 8:21

Lodovichi C, Belluscio L, Katz LC (2003) Functional topography of connections linking mirror-symmetric maps in the mouse olfactory bulb. Neuron 38:265-276

Marin EC, Jefferis GSXE, Komiyama T, Zhu H, Luo L (2002) Representation of the glomerular olfactory map in the Drosophila brain. Cell 109:243-255

Mishima T, Kanzaki R  (1999)  Physiological and morphological characterization of olfactory descending interneurons of the male silkworm moth, Bombyx mori. Journal of Comparative Physiology A: Neuroethology, Sensory, Neural, and Behavioral Physiology 184:143-160

Olsen SR, Bhandawat V, Wilson RI  (2007)  Excitatory interactions between olfactory processing channels in the Drosophila antennal lobe. Neuron 54:89-103

Olsen SR, Wilson RI  (2008)  Lateral presynaptic inhibition mediates gain control in an olfactory circuit. Nature 452:956-960

Porter J, Craven B, Khan RM, Chang S, Kang I, Judkewitz B, Judkewicz B, Volpe J, Settles G, Sobel N  (2007)  Mechanisms of scent-tracking in humans. Nat. Neurosci 10:27-29

Rajan R, Clement JP, Bhalla US  (2006)  Rats Smell in Stereo. Science 311:666-670

van der Goes van Naters W, Carlson JR  (2007)  Receptors and neurons for fly odors in Drosophila. Curr. Biol 17:606-612

Rajashekar KP, Shamprasad VR  (2004)  Maxillary palp glomeruli and ipsilateral projections in the antennal lobe of Drosophila melanogaster. J. Biosci 29:423-429

Reiff DF, Ihring A, Guerrero G, Isacoff EY, Joesch M, Nakai J, Borst A  (2005)  In vivo performance of genetically encoded indicators of neural activity in flies. J. Neurosci 25:4766-4778

Root CM, Masuyama K, Green DS, Enell LE, Nässel DR, Lee C, Wang JW  (2008)  A presynaptic gain control mechanism fine-tunes olfactory behavior. Neuron 59:311-321

Schlief ML, Wilson RI  (2007)  Olfactory processing and behavior downstream from highly selective receptor neurons. Nat. Neurosci 10:623-630

Shang Y, Claridge-Chang A, Sjulson L, Pypaert M, Miesenböck G  (2007)  Excitatory local circuits and their implications for olfactory processing in the fly antennal lobe. Cell 128:601-612

Silbering AF, Galizia CG  (2007)  Processing of odor mixtures in the Drosophila antennal lobe reveals both global inhibition and glomerulus-specific interactions. J. Neurosci 27:11966-11977

Stocker RF, Lienhard MC, Borst A, Fischbach KF  (1990)  Neuronal architecture of the antennal

lobe in Drosophila melanogaster. Cell Tissue Res 262:9-34

Stopfer M, Jayaraman V, Laurent G  (2003)  Intensity versus identity coding in an olfactory system. Neuron 39:991-1004

Suh GSB, Wong AM, Hergarden AC, Wang JW, Simon AF, Benzer S, Axel R, Anderson DJ (2004)  A single population of olfactory sensory neurons mediates an innate avoidance behaviour in Drosophila. Nature 431:854-859

Vickers NJ, Christensen TA, Baker TC, Hildebrand JG  (2001)  Odour-plume dynamics influence the brain's olfactory code. Nature 410:466-470

Wachowiak M, Denk W, Friedrich RW  (2004)  Functional organization of sensory input to the olfactory bulb glomerulus analyzed by two-photon calcium imaging. Proc. Natl. Acad. Sci. U.S.A 101:9097-9102

Wang JW, Wong AM, Flores J, Vosshall LB, Axel R  (2003)  Two-photon calcium imaging reveals an odor-evoked map of activity in the fly brain. Cell 112:271-282

Webster DR, Rahman S, Dasi LP  (2001)  On the Usefulness of Bilateral Comparison to Tracking Turbulent Chemical Odor Plumes. Limnology and Oceanography 46:1048-1053

Wilson RI, Laurent G  (2005)  Role of GABAergic inhibition in shaping odor-evoked spatiotemporal patterns in the Drosophila antennal lobe. J. Neurosci 25:9069-9079

Yan Z, Tan J, Qin C, Lu Y, Ding C, Luo M  (2008)  Precise circuitry links bilaterally symmetric olfactory maps. Neuron 58:613-624

## Figures

**Figure 1. Recording maps of activity in the antennal lobe.**

**Figure 2. Spatial distribution of responses to left or right antennal nerve stimulation.**

**Figure 3. Sexual dimorphism in DA1 PN response.**

**Figure 4. Time dependence of response to bilateral inputs.**

**Figure 5. Complementary effects of fast and slow inhibition.**

**Figure 6. Mapping of inter-glomerular inhibition.**

**Figure 7. DA1 reports inter-antennal difference in stimulus onset.**

**Figure 1**
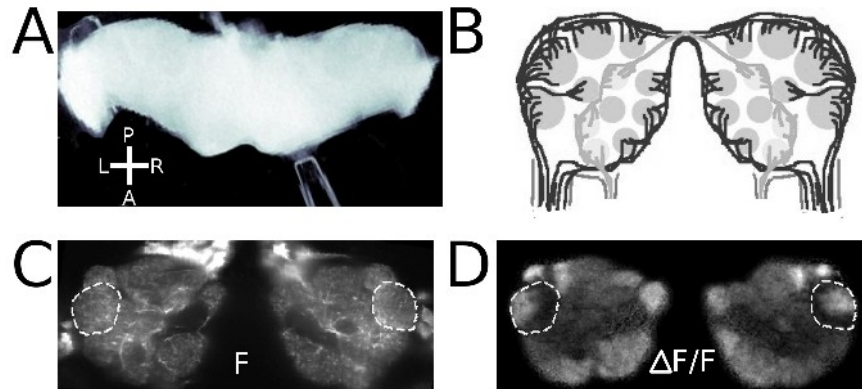


**Figure 1. Recording maps of activity in the antennal lobe. A)** Isolated Brain Preparation, dorsal view. Antennal nerve is sucked into a glass pipette and electrically stimulated. **B)** The antennal lobe receives input from two pairs of nerves innervating bilateral pairs of glomeruli. **C)** Expression of Ca-sensor G-CaMP1.6 in projection neurons, the outputs of the antennal lobe. Resting fluorescence is visible in cell bodies and dendrites. Viewed from the anterior side. **D)** Normalized change in fluorescence ($\Delta F/F$) upon stimulation of antennal nerves reveals an increase of calcium levels in projection neuron dendrites. In panels **C** and **D**, dashed line demarcates DA1 border.
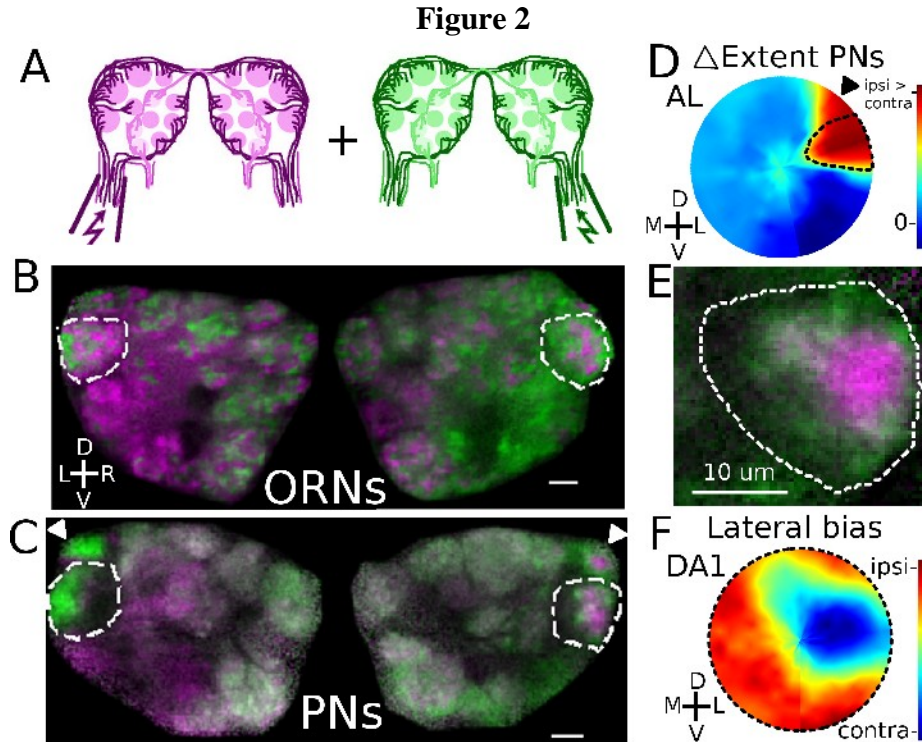
**Figure 2. Spatial distribution of responses to left or right antennal nerve stimulation. A)** Schematic of color-coded responses to left or right nerve stimulation, depicted in magenta or green, respectively, for panels B, C, and E. **B)** Olfactory receptor neuron (ORN) responses to left (magenta) or right (green) nerve stimulation. Cholinergic transmission is blocked. Scale bar = 10 μm. **C)** Projection neuron (PN) responses. Regions that respond to both left and right nerve stimulation are white. **D)** Difference in spatial extent of PN responses to ipsilateral vs. contralateral stimulation in the antennal lobe (AL). Warm regions indicate glomeruli with a more widespread response to ipsilateral stimulation. Average map of 8 antennal lobes. **E)** Closeup of DA1 PNs showing regions activated by ipsilateral or contralateral stimuli. **F)** Regional variation within DA1 of relative response to ipsilateral or contralateral stimulation. In panels **B** through **F**, dashed line demarcates border of DA1. In panels **C** and **D**, arrowhead points to DL3. Panels **B**, **C**, and **E** are from females and their color contrast is enhanced (Suppl. Fig. 2).
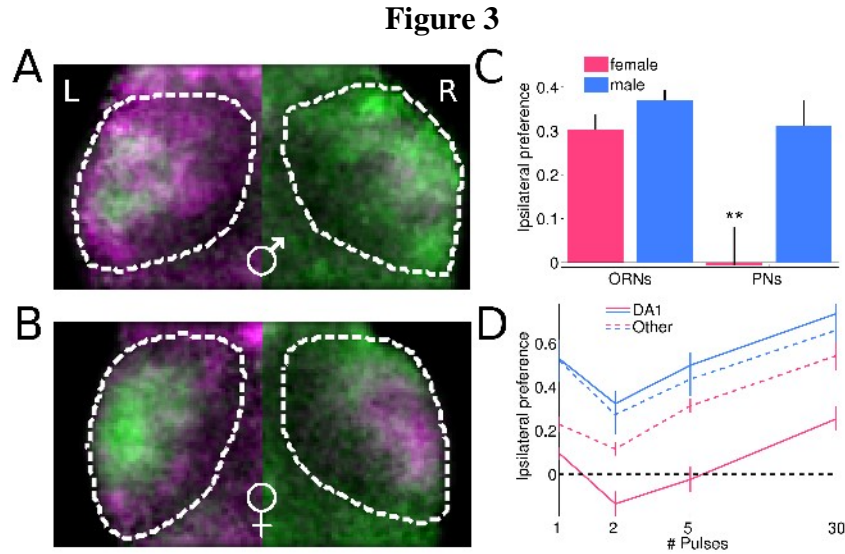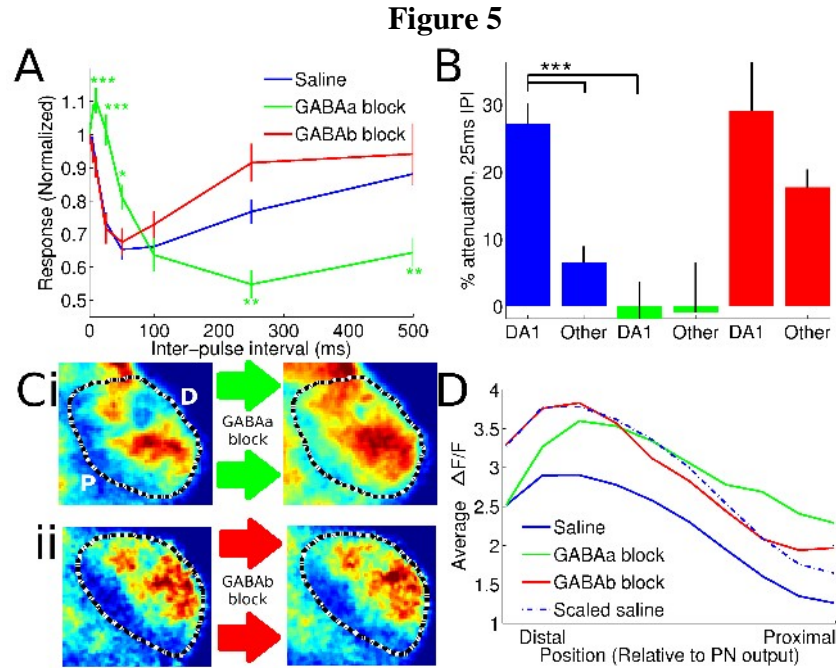
**Figure 3**



**Figure 3. Sexual dimorphism in DA1 PN response. A-B)** Close-ups of left and right DA1. Responses to left and right nerve stimulation are colored purple and green, respectively. **A)** Male, **B)** Female. **C)** Preference for ipsilateral over contralateral stimuli in DA1 for males and females. Sexual dimorphism in preference is only seen postsynaptically. Ipsilateral preference in female PNs differs from that of ORNs and males (n = 8 for each). ** p < .01 **D)** Dependence of preference of PNs on number of pulses, for DA1 and other glomeruli in males and females. The DA1 bias in females is significantly lower than that of males for all pulse numbers, p < .001. Ipsilateral preference = $\log(\Delta F_{ipsi} / \Delta F_{contra})$. A value greater than 0 indicates that glomerulus responds more to stimulation of the ipsilateral nerve than to stimulation of the contralateral nerve. All responses are integrated over the 0.5 s period following start of stimulation.

**Figure 4**
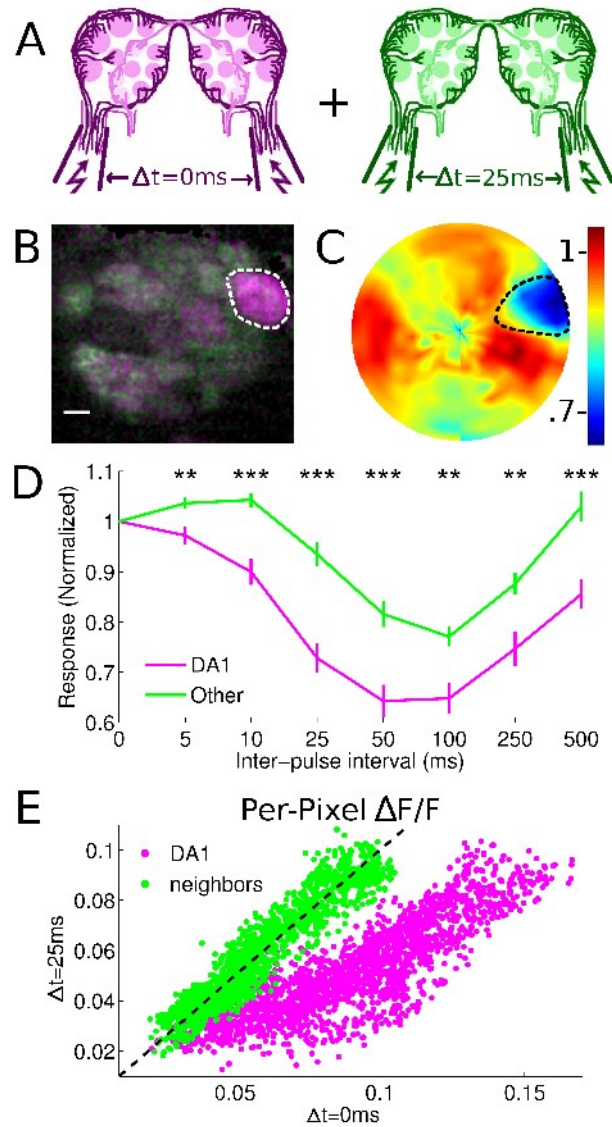
**Figure 4. Time dependence of response to bilateral inputs. A)** Response to stimulation of each nerve with a single pulse, either simultaneously or with a 25 ms inter-pulse interval (IPI), represented as purple or green, respectively. **B)** Map of relative response to simultaneous vs. staggered inputs. Scale, 10 μm  **C)** Averaged map of response attenuation, ratio of ΔF/F at 0 vs. 25 ms. (26 ALs)  Cold regions show greater attenuation. **D)** Average responses (n=13) in DA1 and other glomeruli to IPI's  ranging from 0 to 500ms. *** $p < .001$, ** $p < .01$. In panels **B** and **C**, dashed line demarcates DA1 border. **E)** Representative example of response attenuation of points in a contiguous region. Each point represents a pixel's ΔF/F at 0 ms vs. 25 ms IPI. Pixels within DA1 are purple. Dashed black line represents 0 attenuation.

**Figure 5**



**Figure 5. Complementary effects of fast and slow inhibition. A)** Dependence of DA1 PN responses on IPI shifts with blockade of fast or slow inhibition. Normalized to 0ms IPI. Green asterisks mark time points where GABAa block significantly differs from saline condition. **B)** Larger attenuation in DA1's response at 25 ms IPI is eliminated by blocking fast inhibition. Blue, saline; green, GABAa blocked; blue, GABAb blocked. **C)** Normalized close-ups of DA1 response at 0ms IPI, before vs. after GABAa or b block. Dashed line demarcates DA1 border. In top right panel, 'P' and 'D' indicate proximal and distal regions of PN dendrites, relative to PN output. **D)** Average ΔF/F in DA1 as a function of position along the proximal-distal (relative to PN output) axis, in response to stimulation of one antennal nerve with a single pulse (n = 16, average of ipsilateral and contralateral responses). Blocking fast inhibition preferentially increases activity in the proximal part of PN dendrites, while blocking slow inhibition scales activity up approximately linearly. For **A** and **B**, * p < .05, ** p < .01, *** p < .001.

**Figure 6**
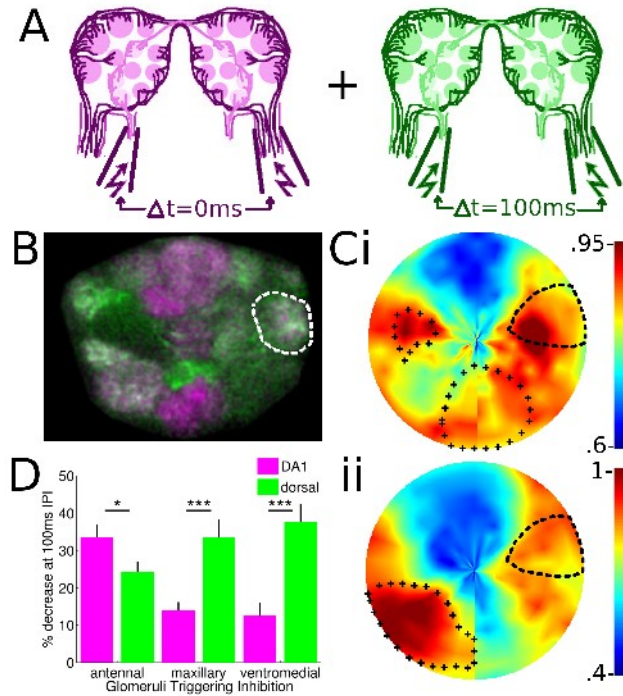


**Figure 6. Mapping of inter-glomerular inhibition. A)** Schematic of color-coded responses to stimulation of maxillary and antennal nerve with a single pulse, either simultaneously or with 100ms inter-pulse interval (IPI), represented as magenta or green, respectively. **B)** Responses to 0 (magenta) or 100 ms (green) IPI. Color contrast is enhanced. **C)** Averaged ratio of the two delays, **Ci)** with maxillary nerve stimulation, 28 antennal lobes; **Cii)** with ventro-medial neuropil stimulation, 16 antennal lobes. Cold regions show greater decrease at 100ms. '+' outlines indicate regions activated in order to trigger inhibition. **D)** % decrease of response at 100ms IPI vs. 0ms IPI, in DA1 and dorsal glomeruli. When compared to dorsal glomeruli, DA1 experiences greater overall inhibition but weaker interglomerular inhibition. * p < .05, ** p < .01, *** p < .001. In panels **B** and **C**, DA1 is demarcated with a dashed line.
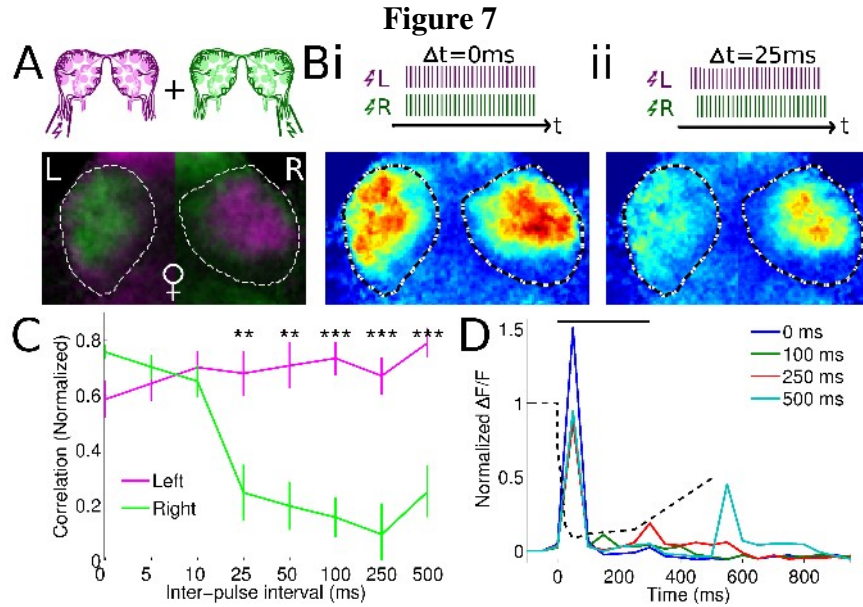
**Figure 7. DA1 reports inter-antennal difference in stimulus onset. A)** Close-up of left and right DA1 from a female. Purple and green depict regions activated by ipsilateral or contralateral stimuli. Color contrast is enhanced. **B)** Response to sustained stimuli (30 pulses at 100Hz) **i,** simultaneous, **ii,** offset by 25 ms. **C)** For onset delays of 25ms or longer, the spatial pattern of response correlates much more strongly to the response to left nerve stimulation alone than the response to right nerve stimulation alone. ** p < .01, *** p < .001, n = 14. **D)** Temporal profile of average (n = 14) DA1 response at different onset delays, indicated in legend. Traces are corrected for slow decay of G-CaMP response. Solid black bar indicates time when left nerve is stimulated. Dashed line indicates timecourse of delay-dependent inhibition of transient response to right nerve stimulation. Normalized to peak response to right-nerve only stimulation.

49

## Supplementary Information

**Supplementary Figure 1.  Conversion of maps into polar coordinates for averaging.**

**Supplementary Figure 2.  Increasing Color Contrast in Two-Color Image.**

**Supplementary Figure 3.  Concordance of pre- and postsynaptic lateralized response properties.**

**Supplementary Figure 4.  Differences in correlation of ipsilateral and contralateral responses within glomeruli pre- and postsynaptically.**

**Supplementary Figure 5.  Three measures of regional variation in DA1's preference for ipsilateral or contralateral inputs.**

**Supplementary Figure 6.  Timecourses of response to ipsilateral and contralateral stimulation.**

**Supplementary Figure 7.  Sexual Dimorphism in Lateral Bias.**

**Supplementary Figure 8.  Capturing subthreshold variations in glomerular excitability.**

**Supplementary Figure 9.  Blocking GABAa increases lateral inhibition at certain time intervals.**

**Supplementary Movie 1.  Temporal evolution of PN excitability.**

**Supplementary Movie 2.  Model of plume direction discrimination by DA1.**
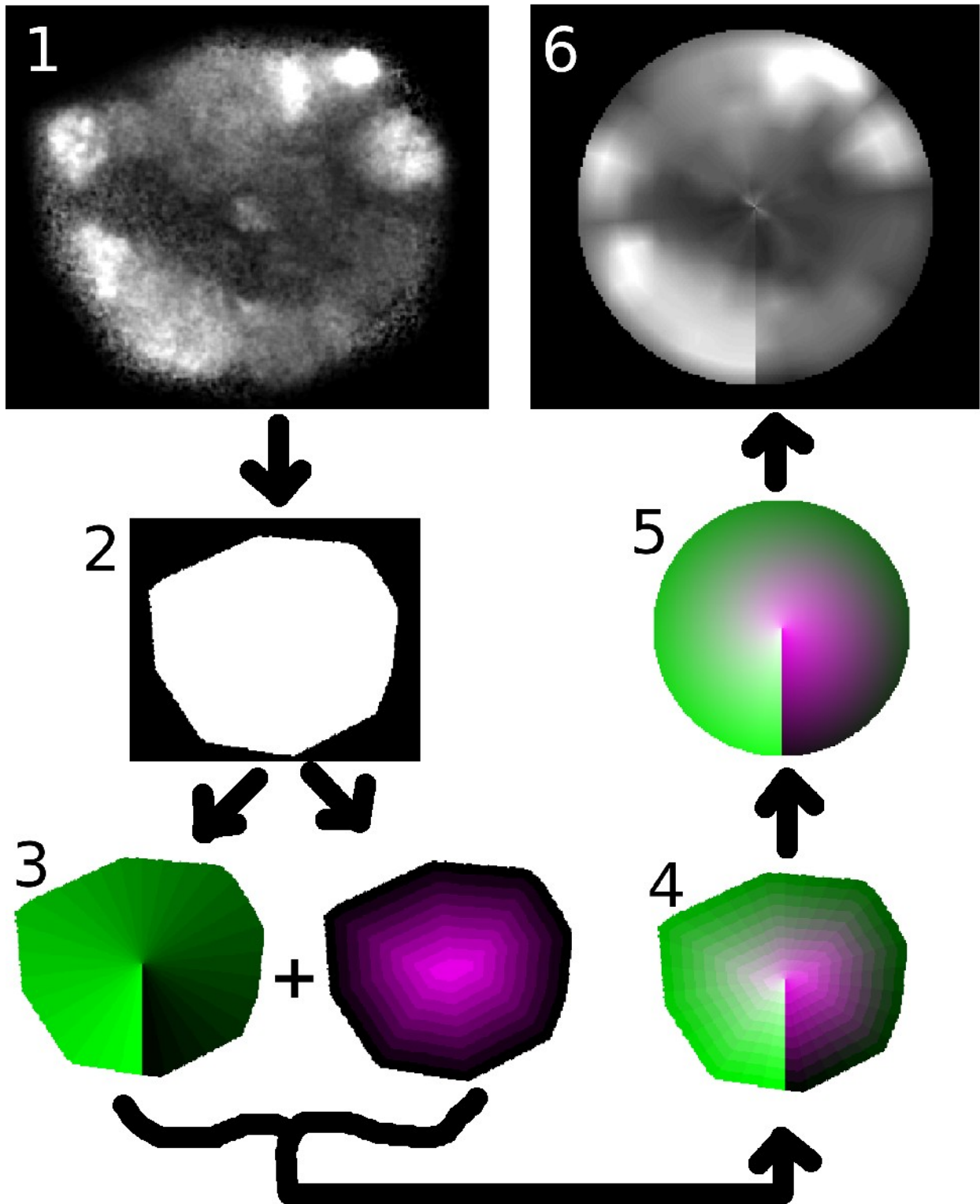
**Supplementary Figure 1. Conversion of maps into polar coordinates for averaging. 1)** Map of evoked response. **2)** Convex region of interest (ROI) is manually drawn that surrounds antennal lobe neuropil. **3)** Each pixel within ROI is assigned a bin with respect to its angle from the center of the antennal lobe, as well as its distance from the periphery of the antennal lobe. In this case, there are 10 radial bins (color-coded in green) and 30 angular bins (color-coded magenta). **4)** This produces 300 unique bins that are addressed by radial and angular position; the $\Delta$F/F of all pixels within each bin are averaged to determine its mean response. **5)** Using script PolarToIm, the map is transformed into a circle. **6)** The 300 mean values are assigned to their respective bins, producing a standard map that allows multiple preparations to be averaged.

**Supplementary Figure 2**



# Original

## A

# Color Enhanced

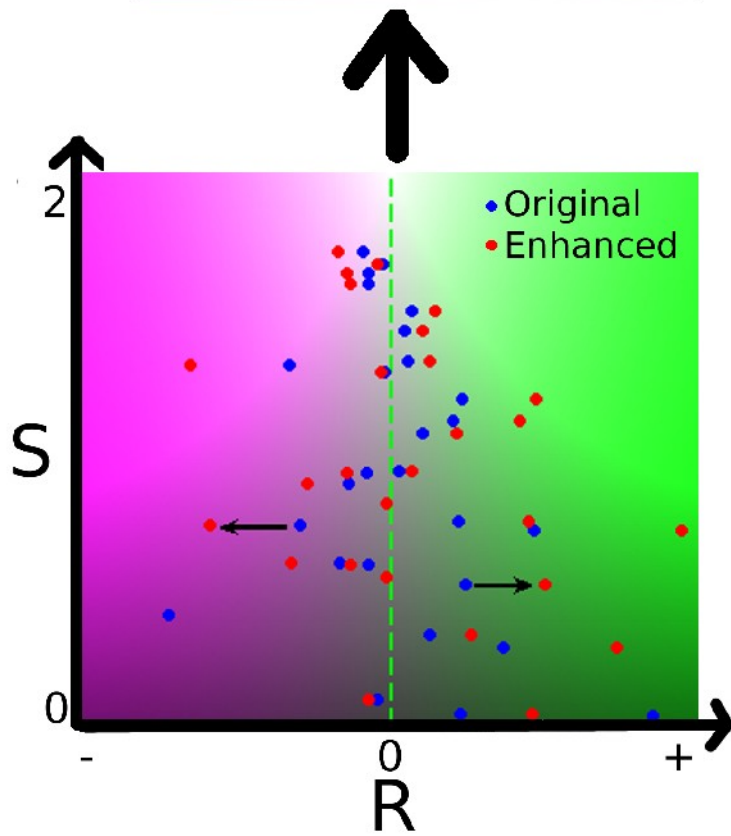## C

## B
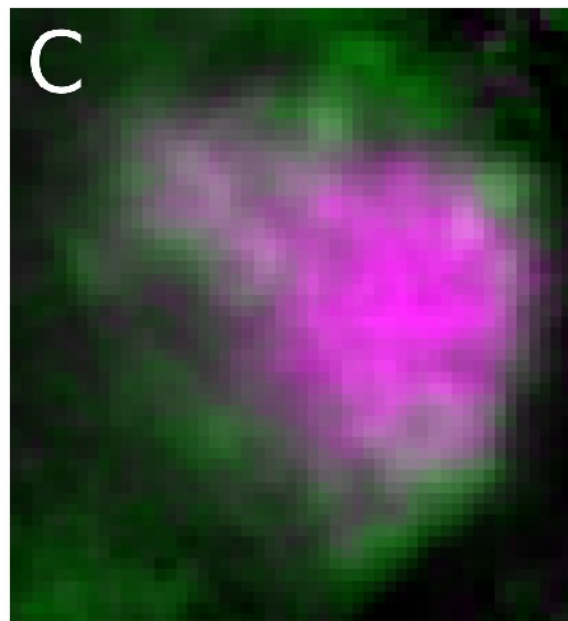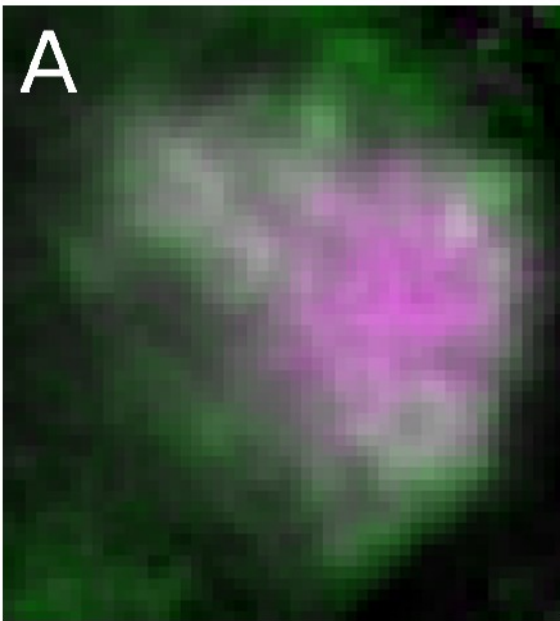
S = G+M
R = log(G/M)
G1 = S*(1+tanh(αR))/2
M1 = S*(1-tanh(αR))/2

where

G = green intensity
M = magenta intensity
S = sum
R = log ratio
α = color factor
tanh = hyperbolic tangent
G1 = new green
M1 = new magenta

**Supplementary Figure 2. Increasing Color Contrast in Two-Color Image. A)** Original image showing close up of DA1 (from Fig. 2E), with ipsilateral response color-coded in green and contralateral response color-coded in magenta. **B)** Left: Algorithm to change each pixel's color value. The transform takes as inputs each pixel's intensity in the two channels (G and M), and a factor that determines how much the contrast between channels is enhanced ($\alpha$). Its output is new intensity values for each pixel in the two channels (G1 and M1). Right: Schematic of pixel value modification. Each point represents a pixel, its position determined by the sum (y axis) and log ratio (x axis) of intensities in its two channels. Upon applying the transform, pixels shift away from the midline (dashed green line, equal intensity in two channels), without any vertical displacement. This indicates an increase in contrast without any shift in the total intensity. Background indicates color corresponding to pixel position. Arrows indicate shift of color for two pixels, one more green and the other more magenta. **C)** Color-contrast enhanced image, $\alpha = 1$. Image is renormalized to ensure no intensities exceed 1 in either channel.
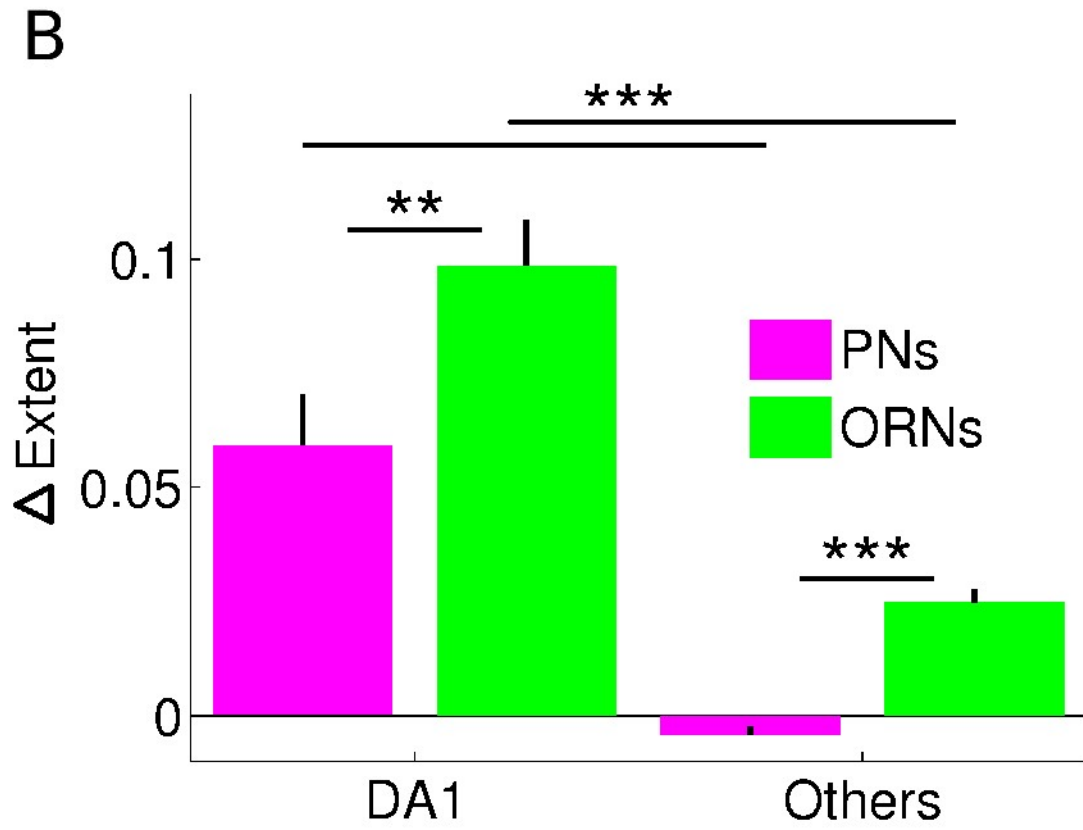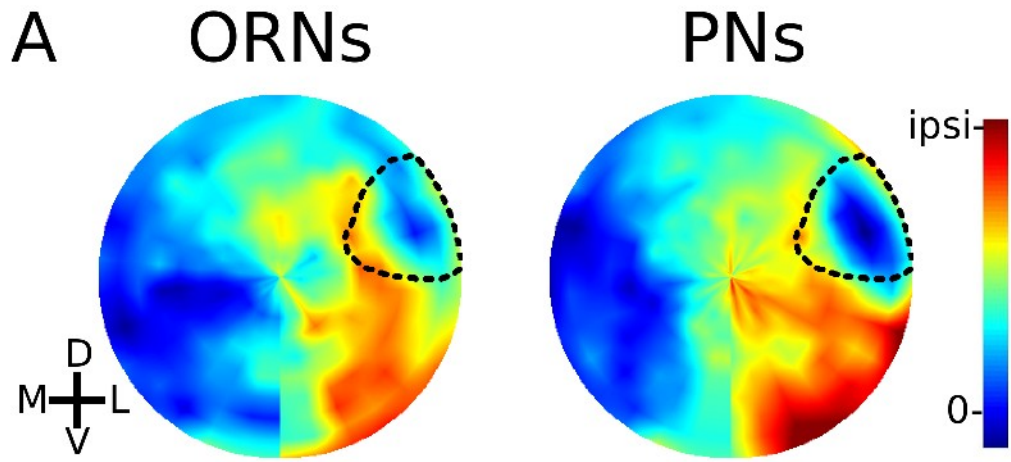
**Supplementary Figure 3. Concordance of pre- and postsynaptic lateralized response properties.** Data was collected using flies expressing GcaMP in both ORNs and PNs (See methods for description of how pre- and postsynaptic responses were isolated). **A)** Average maps of response preference to ipsilateral vs. contralateral stimulation. Warm regions respond more to ipsilateral stimulation. 0 indicates equal preference to ipsilateral or contralateral stimulation. n = 16 for each map. B) Ipsilateral stimulation activates a larger region within DA1 than contralateral stimulation, both in PNs and in ORNs. In PNs of non-DA1 glomeruli there is no difference between the area activated by ipsi- and contralateral stimulation. Ipsilateral stimulation activates a significantly larger region in ORNs than in corresponding PNs. *** $p < .001$, ** $p < .01$.
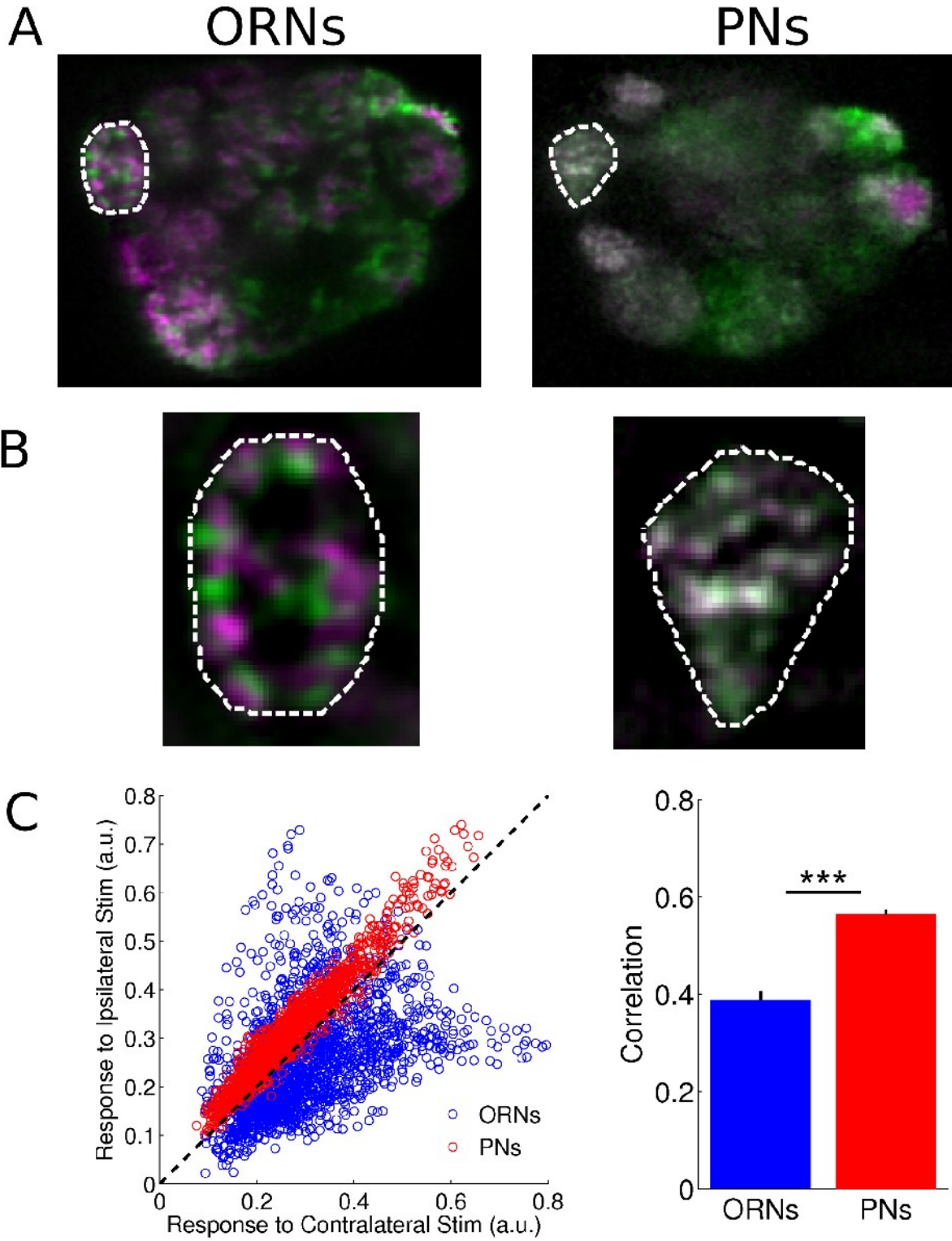
**Supplementary Figure 4.  Differences in correlation of ipsilateral and contralateral responses within glomeruli pre- and postsynaptically.**  **A)** Representative antennal lobe responses in ORNs (left) and PNs (right).  Responses to contralateral stimulation are in magenta, ipsilateral stimulation in green.  **B)** Close-ups of medial glomeruli circled in panel A.  To highlight spatial variation between responses, each channel was bandpass filtered by subtracting from the original image a smoothed image produced using a gaussian with $\sigma = 10$ pixels.  **C)** Left: A scatter plot depicting similarity between responses to ipsilateral and contralateral stimulation for regions circled in A.  Each point represents a pixel's $\Delta F/F$ in arbitrary units to ipsilateral vs. contralateral stimulation.  Dashed black line indicates pixels that respond equally to the stimulation of either nerve; PNs fall closer to this line.  Right: Average correlation between glomerular response to ipsilateral vs. contralateral glomeruli for ORNs and PNs.  n = 227 glomeruli from 8 preparations.  Pre- and postsynaptic activity was isolated from flies expressing G-CaMP both pre- and postsynaptically (see methods).

**Supplementary Figure 5**
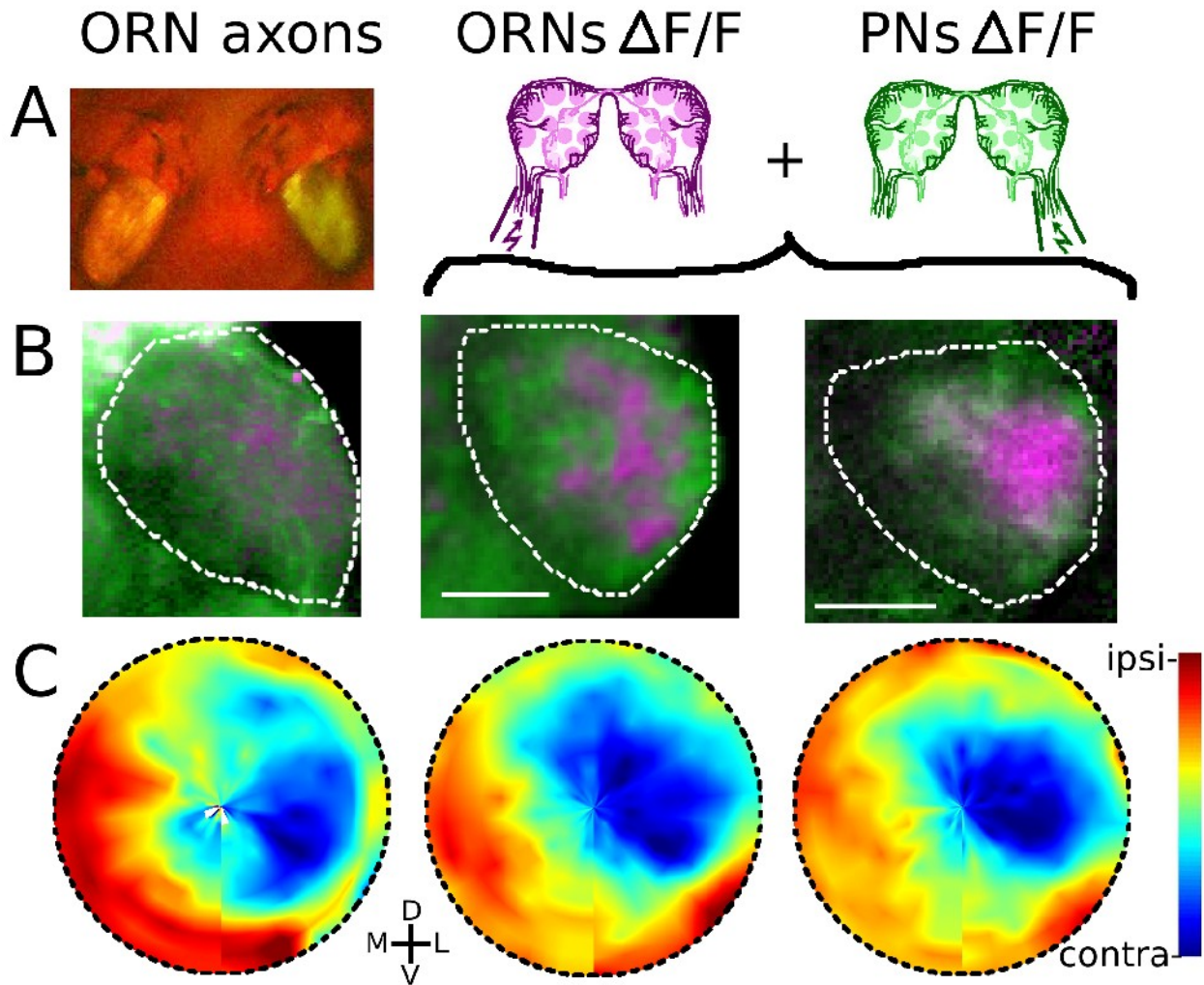
**ORN axons**   **ORNs ΔF/F**   **PNs ΔF/F**

**Supplementary Figure 5.  Three measures of regional variation in DA1's preference for ipsilateral or contralateral inputs.** Left column   ORN axons; middle column -ΔF/F in ORN terminals; right column   ΔF/F in PN dendrites. **A)** Left panel: UAS-Kaede was expressed in ORN's.  UV was shined on left antenna (for 6 minutes, twice, at 4-hour interval, followed by 4 hour wait) to photoconvert its Kaede from green to red.  Middle and right panels: left or right nerve was stimulated, as in Fig. 2.  **B)** Close-ups of single DA1's for each preparation.  Green ipsilateral, magenta   contralateral.  Color contrast is enhanced. **C)** Average maps for each preparation.  For middle and right maps, data was collected using flies expressing GCaMP in both ORNs and PNs (See methods for description of how pre- and postsynaptic activity was isolated).  Left: n = 8.  Middle and right: n = 16.
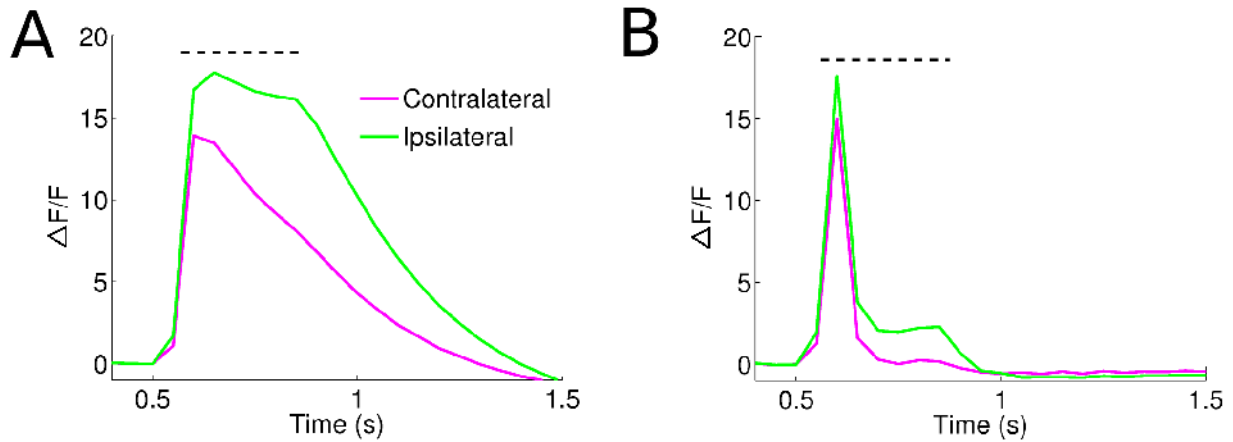
**Supplementary Figure 6.** **Timecourses of response to ipsilateral and contralateral stimulation.** **A)** Mean responses, n = 362 glomeruli from 7 preparations. Dashed line indicates time of stimulus (30 pulses at 100 Hz). **B)** Responses after deconvolving the slow exponential decay of G-CaMP 1.6, estimated to be ~350 ms. Note persistent response only present in ipsilateral activation.
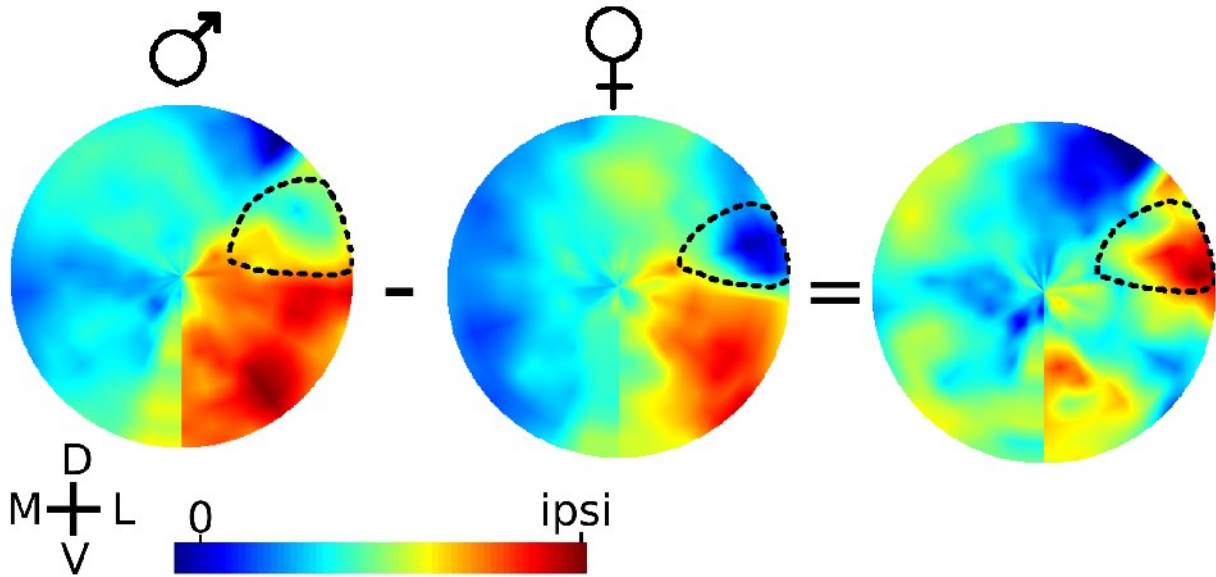
**Supplementary Figure 7. Sexual Dimorphism in Lateral Bias.** Average maps of lateral preference in males (left) and females (middle). Preference was calculated as the log ratio of ipsilateral to contralateral response; warmer colors represent greater preference for ipsilateral stimuli. The difference of these maps yields the right panel, which shows DA1 has a disproportionately ipsilateral preference in males. n = 8 antennal lobes for both males and females. Note the slight difference in DA1's size and position in males and females; this leads to a slight offset in the difference image to the right. Maps shown here represent the result of 30-pulse trains.
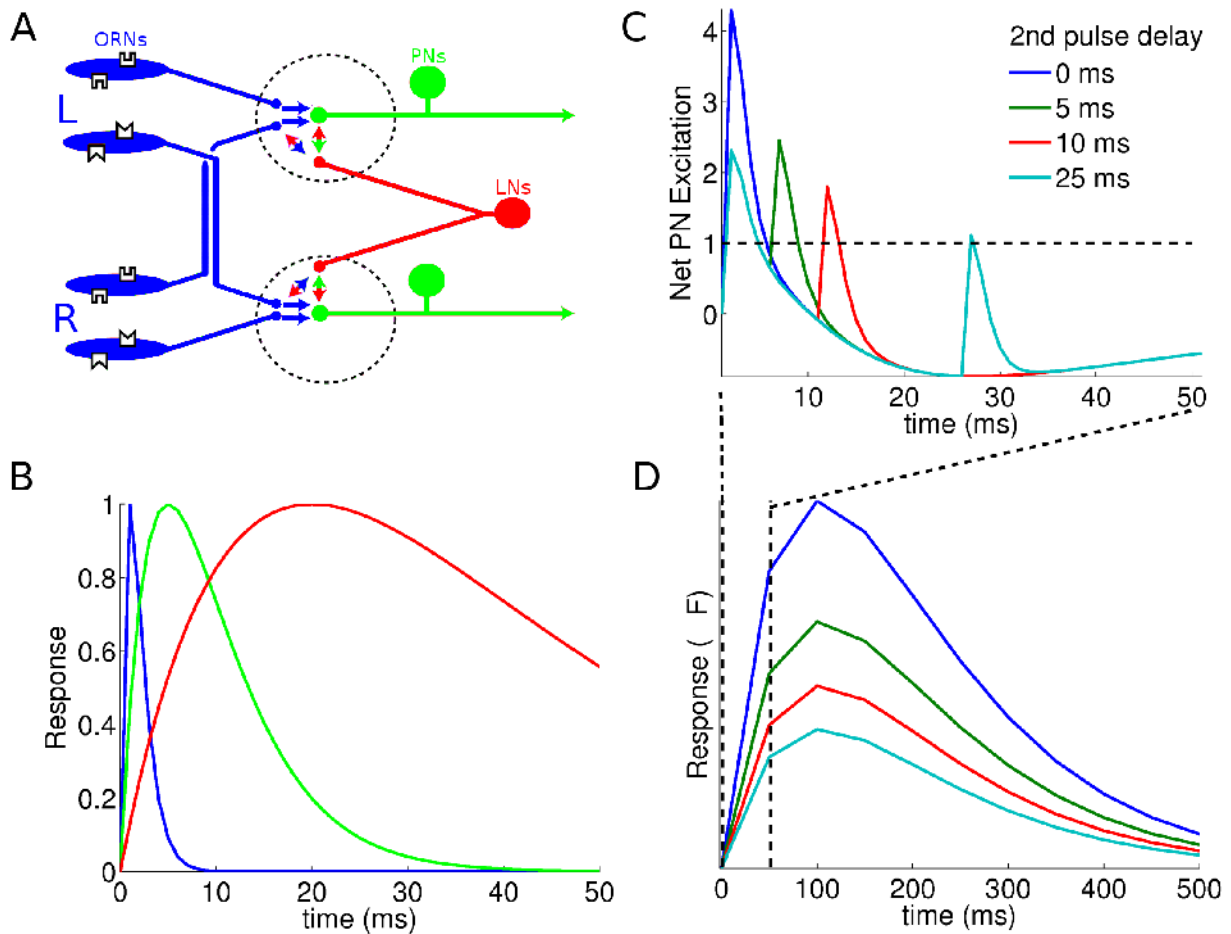
**Supplementary Figure 8. Capturing subthreshold variations in glomerular excitability. A)** Schematic of antennal lobe showing ORNs in blue, PNs in green, and LNs in red (adapted from Wilson and Mainen 2006). **B)** Hypothetical depiction of normalized timecourses of activity modulation in PNs by activation of ORNs, PNs, and LNs. **C)** Hypothetical timecourse of glomerular excitation evoked by stimulating left and right nerves with inter-pulse intervals ranging from 0 to 25 ms. Dashed black line indicates hypothetical threshold of activation of a calcium indicator G-CaMP1.6. **D)** Resultant response of G-CaMP1.6 evoked by different IPI's. The total magnitude of response can be used to infer the state of excitability at different intervals after initial activation of the glomerulus.
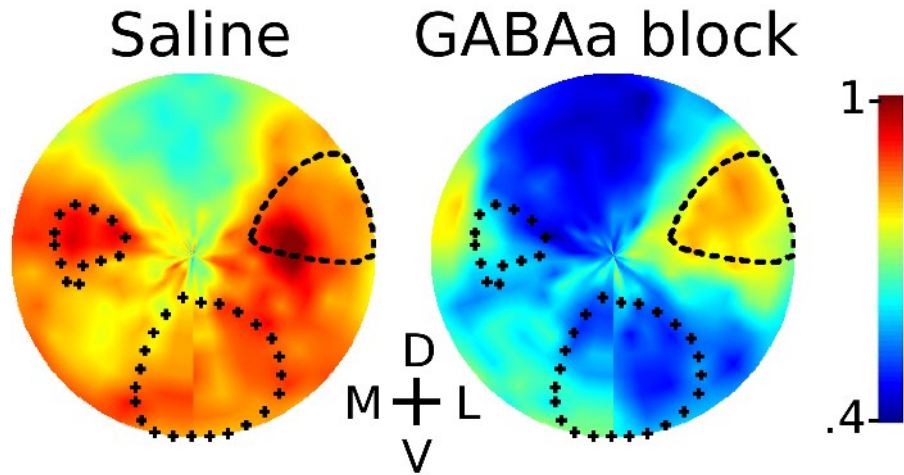
**Supplementary Figure 9. Blocking GABAa increases lateral inhibition at certain time intervals.** The antennal and maxillary nerves are stimulated, either simultaneously or with a 100 ms delay in antennal nerve stimulation. The ratio of the two delays is mapped, in saline (left map) and with GABAa blocked (right map). Delaying antennal nerve stimulation causes a decrease in response in both cases, but this decrease is greater when GABAa is blocked. Colder colors indicate greater decrease. Maxillary glomeruli outlined in pluses, DA1 outlined with a dashed line.

## Supplementary Movies
(Submitted as separate files)

**Supplementary Movie 1.  Temporal evolution of PN excitability.**  Average map of antennal lobe depicting change in excitability upon antennal nerve stimulation.  Time, indicated in each frame, progresses logarithmically to convey the rapid changes that happen in the first 25 ms. Cool regions depict greater inhibition; dashed black line outlines DA1.  Frames between tested time points (0, 5, 10, 25, 50, 100, 250, and 500 ms) are linearly interpolated.

**Supplementary Movie 2.  Model of plume direction discrimination by DA1.**  **(Left)** A virtual pheromonal plume (white bar) engulfs a fly head from the left, right, and front.  Image of fly head courtesy of Flybase, provided by Rudy Turner.  **(Top right)** Close-up of antennae, depicting activation of DA1-innervating ORNs upon contact with plume.  Magenta and green represent activation of ORNs on the left and right antennae respectively.  Distribution of DA1-innervating ORNs based on data from Fishilevich and Vosshall, *Current Biology* 2005. **(Bottom right)** Close-up of left and right DA1s, depicting activation of DA1 PNs in response to plume.  Magenta and green represent spatial patterns activated by stimulation of left or right antenna alone. Unlike ORNs, directional contact with odor plume elicits transient, selective activation of the spatial pattern corresponding to the antenna that was first activated.

# Appendix 1

## Closing In on the Resting State of the Shaker K$^+$ Channel

## Summary

Membrane depolarization causes voltage-gated ion channels to transition from a resting/closed conformation to an activated/open conformation. We used voltage-clamp fluorometry to measure protein motion at specific regions of the Shaker Kv channel. This enabled us to construct new structural models of the resting/closed and activated/open states based on the Kv1.2 crystal structure using the Rosetta-Membrane method and molecular dynamics simulations. Our models account for the measured gating charge displacement and suggest a molecular mechanism of activation in which the primary voltage sensors, S4s, rotate by ~180° as they move outward by 6 8 Å. A subsequent tilting motion of the S4s and the pore domain helices, S5s, of all four subunits induces a concerted movement of the channel's S4-S5 linkers and S6 helices, allowing ion conduction. Our models are compatible with a wide body of data and resolve apparent contradictions that previously led to several distinct models of voltage sensing.

## Introduction

Voltage-gated ion channels open and close in response to changes in membrane potential and rapidly and selectively conduct ions across cell membranes. Their ability to sense the membrane potential is conferred via a voltage-sensing domain (VSD, transmembrane segments S1-S4), which regulates the conformation of molecular gates located in the pore domain (PD, transmembrane segments S5-S6). Detailed structural information at atomic resolution is needed to understand the mechanism underlying voltage gating. The recent structure of the mammalian

Kv1.2 voltage-gated K$^+$ channel, though partially incomplete, revealed the general organization of the VSD in what appears to be the activated and open state (Long et al., 2005a). The earlier high-resolution crystal structure of the bacterial voltage-gated channel KvAP (Jiang et al., 2003a and Jiang et al., 2003b) captured the protein in a nonnative conformation (Lee et al., 2005), with the VSDs separated from the PD, suggesting that the interactions between the VSD and PD are weak and that large relative movements could occur between these two domains during gating.

To understand the voltage-sensing motion, recent studies tried to elucidate the resting/closed conformation by measuring voltage-dependent changes in internal and external accessibility of VSD segments (Gandhi et al., 2003, Phillips et al., 2005 and Ruta et al., 2005), changes in the location of the charged S4 relative to either a pore blocker or to lipid-soluble probes (Chanda et al., 2005 and Posson et al., 2005), and the distance needed to move an S4 charge through the membrane electric field (Ahern and Horn, 2005). These studies arrived at widely different models of the voltage-sensing motion (Tombola et al., 2005a). Two more recent studies    one that mapped the omega current pathway that ions take through the VSD in the resting state (Tombola et al., 2007) and the other which probed suppressor interactions between mutations in S4 and neighboring helices (Grabe et al., 2007)  arrived at more compatible results, but still lacked sufficient constraint for a complete model.

In order to fill in this gap, we performed a scan for protein motion on the externally accessible portion of the Shaker $K^+$ channel using voltage-clamp fluorometry (VCF). VCF is a time-resolved method that provides information about local protein motion associated with specific gating steps. The structural rearrangement is reported by a fluorophore attached in a site-directed manner to one of a large series of individual positions from which one can reconstruct global motions. The VCF experiments provide new information on the VSD motion associated with activation, enabling us to construct new structural models of the resting and open state of the Kv1.2 channel. The models are generated by a combination of Rosetta-Membrane modeling and molecular dynamics simulations. The structural models are consistent with a number of key experimental observations and for the first time reconcile seemingly disparate data that have led to considerable debate in the field. Therefore, the findings provide new insight into the molecular mechanism of voltage-dependent gating.

## Results

### Fluorescence Scan of the Voltage-Sensing Domain and the Pore Domain

We examined a large portion of the extracellular region of the Shaker channel and created rearrangement maps for the VSD and PD. Single amino acids were substituted with cysteine at 82 positions in the external portion of the channel (Figure 1 and Table 1). Of these cysteine mutants, 73 expressed functional channels and were studied further. Oocytes expressing each cysteine mutant were covalently labeled with the environment-sensitive fluorophore tetramethylrhodamine-6-maleimide (TMRM), which attached to the engineered cysteine. A single depolarizing voltage step from a holding potential of −80 mV to a positive voltage was

used to activate and open the channel. The step was long enough to induce activation, opening and slow inactivation, resulting in a transient ionic current (Figure 1B). In parallel to measuring ionic current, we measured fluorescence from ~15% of the surface of the oocyte. A change in fluorescence (ΔF) was detected at 56 attachment positions, indicating that they are exposed enough to the external solution to permit conjugation by the charged extracellular TMRM and that a protein motion occurs in the labeled segment, or its surround, resulting in a change in the environment of the fluorophore. An examination of the ΔFs from all of the sites shows that they have unique fluorescence signatures, even in adjacent amino acid positions (Figure 1C and Table 1). This indicates that TMRM senses a small region of space in the vicinity of the side chain to which it is attached and that moving the attachment site by only one amino acid means pointing in a different direction where distinct interactions occur with the surrounding environment. In other words, VCF provides information about protein motion at a single amino acid resolution.

The ΔFs detected from different attachment sites varied in magnitude and polarity and tracked distinct subsets of functional transitions, such as activation, opening, inactivation, and recovery from inactivation. The ΔF measured during a depolarizing step could be divided into fast and slow components (Figure 1C). The slow component tracked the process of slow inactivation of the ionic current (data not shown, see Gandhi et al., 2000). In this study, we focus on the fast component, which took place during the rise of the ionic current and which we found to correspond to channel activation.

**Detection of Protein Motion Associated with Voltage Sensing**

Sites with a fast ΔF could experience an environment change during either the voltage-sensing steps of activation or during opening. We identified the positions that report on the voltage-sensing steps of activation by examining the ΔF elicited in response to a voltage step that changes the activation state but does not open the channel. For example, channels were given hyperpolarizing steps and depolarizing steps that were too small to open the channel, from a holding potential of −80 mV (Figure 2A). We observed ΔFs in response to these nonopening voltage steps for all of the sites in the VSD. Previous studies showed that the ΔF of TMRM at sites in or near the Shaker S4 segment tracks the channel's gating charge movement, i.e., the voltage-sensing steps of activation (Baker et al., 1998, Cha and Bezanilla, 1997, Gandhi et al., 2000, Mannuzzu and Isacoff, 2000 and Mannuzzu et al., 1996). We found the same to be true for other sites in the VSD outside of S4. An example of this is shown for site 275 in S2, for which we compared the gating charge displaced to the ΔF (Figures 2B and 2C). We found that the kinetics of the ΔF tracked the ON and OFF gating current. Moreover, the steady-state voltage dependence of fluorescence closely overlapped with the voltage dependence of the gating charge movement. This analysis provides a clear demonstration that TMRM at this position experiences a local

protein motion during voltage sensing.

We also observed fast ΔFs at some sites in the PD (Figure 1 and Table 1). The fast ΔFs in this region appear to primarily track the conformational changes of channel opening, rather than voltage sensing (see Figure S1A). These sites mapped to the tops of the turret and the S5-P loop of the PD (Figure S1B), rather than peripheral regions located closer to the VSD, which could potentially feel the voltage-sensing motion of S4. Taken together, these observations suggest that voltage-sensing motions do not propagate extensively into the extracellular portion of the PD but that opening rearrangements of the PD involve a conformational change that extends from the inner surface to the outer surface of the PD.

## Magnitude of Protein Motion

Earlier evidence indicates that S4 substantially changes internal and external exposure during voltage sensing and carries most, if not all, of the gating charge (Gandhi and Isacoff, 2002), suggesting that it undergoes a large conformational change. In contrast, accessibility assays on S1 and S2 suggested that they do not posses a significant transmembrane motion (Gandhi et al., 2003 and Ruta et al., 2005), although one charged residue on S2 has been suggested to move gating charge (Seoh et al., 1996). The evidence has also been split as regards S3, with biotin trapping by Avidin in KvAP suggesting a large motion (Jiang et al., 2003b) but not in Shaker (Darman et al., 2006), and MTS reagent accessibility in Shaker (Gandhi et al., 2003 and Gonzalez et al., 2005) and hanatoxin accessibility in Kv2.1 showing little change (Phillips et al., 2005).

We asked how we could extract information regarding the magnitude of protein motion from our fluorescence data set. The fluorescence changes we measure are due to changes in local environment experienced by the fluorophore during a conformational change in the protein. Any changes in local environment due to thermal fluctuations are averaged in the fluorescence signal, which arises from fluorophores attached to millions of channels at the plasma membrane of the cell. A ΔF in response to a voltage step means that the environment surrounding the fluorophore has changed beyond the average thermal fluctuations, due to a net rearrangement in the protein induced by voltage change. In other words, the conformational change in the protein must connect energetically separated states in order for us to see a fluorescence change. Large environmental transitions that would generate ΔFs of large magnitudes are possible with small protein movements. However, given side chain vibrations and the flexibility of some of the bonds in the TMRM linker, which will permit the TMRM to explore a cone of space, it is more likely that a larger motion will make for a larger environmental transition. In addition, very small

protein movements connecting states that are energetically well separated (not visited by the protein just by simple thermal fluctuations) are possible but uncommon. Finally, in the event that a small motion causes a large environmental transition at one residue because it happens to carry that residue across a sharp structural boundary, we would observe a ΔF of large magnitude only at an isolated site, not at neighboring positions in the helix. Thus it is reasonable to assume that ΔFs of larger magnitudes observed at *several* residues in a helical segment are indicative of larger conformational changes of that segment. We reasoned that small motions of a helix would be expected to produce ΔFs of small magnitudes, perhaps only in a short segment of the helix at its edge of exposure, while large motions would produce large environment changes and ΔFs of large magnitudes that would be observed over a longer segment of the helix.

Starting with the outer end of each helical region of the Kv1.2 crystal structure, we counted the number of residues in each VSD helix that had a detectable ΔF. We found that the number of residues was smallest in S1 (with none of the residues showing detectable ΔFs falling within the helical region resolved in the Kv1.2 crystal structure), larger in S2, and largest in S3 and S4 (Figure 3A). We examined the ΔF amplitudes for each of the VSD helices (Figure 3B). The average fluorescence change progressively increased in magnitude from S1 to S4. The data are consistent with the notion that S3 and S4 undergo greater voltage-sensing motions than S1 and S2 (see Figure 6D below). Our results are consistent with an earlier perturbation scan of Kv2.1, which found a trend in perturbation energies across the VSD, with the smallest effects occurring in S1 and the largest effects occurring in S4 (Li-Smerin et al., 2000).

**Nature of Voltage-Sensing Rearrangement of VSD**

The large-magnitude ΔFs in S4 are consistent with the large changes in accessibility of S4 residues to MTS reagents (for review see Gandhi and Isacoff, 2002). However, the large magnitude of ΔFs in S3 were unexpected given the lack of change in accessibility of S3 residues to MTS reagents in Shaker (Darman et al., 2006 and Gandhi et al., 2003). Could the ΔFs in S3 mean that S3 also undergoes a large motion? In principle, large ΔFs in S3 could arise either from a motion of S3 itself or from the rearrangement of another part of the protein near S3, for example from the motion of S4. This would be predicted to occur only for attachment sites on the side of S3 that faces S4. However, the large ΔFs mapped to all sides of S3 (Figure 3C), suggesting that S3 moves relative to its entire surrounding environment during voltage sensing. These results are consistent with the biotin-trapping experiments in KvAP that showed a voltage-dependent change in both S3 and S4 access to a large avidin (Jiang et al., 2003b). In addition, the results suggest that the reason that S3 motion was not detected with MTS probing in Shaker (Gandhi et al., 2003) is that in the resting state of the VSD S3 is in a more external and exposed position compared to S4, perhaps at the outer end of the omega pathway (Tombola et al., 2007),

and thus within reach of small MTS reagents. While S3 and S4 appear to move together, the large ΔFs seen along the interface between them (Figure 3C) suggest that they also experience a relative displacement.

**Modeling of the Resting Conformation of the Kv1.2**

We used the patterns of S3 and S4 motion observed in the fluorescence scan along with information about the resting-state conformation of the VSD gathered from a structure-driven perturbation scan of the omega current (Tombola et al., 2007) and accessibility of S6 residues (del Camino et al., 2005 and del Camino and Yellen, 2001) to model the resting-state structure of Kv1.2 as described below. As a starting model, we used the previously developed Rosetta-Membrane model of Kv1.2 (Yarov-Yarovoy et al., 2006a).

**Pore-Forming Domain and the S4-S5 Linker Modeling in the Resting State**

To generate a model of the resting channel, we made a model of the closed state of the PD of the Kv1.2 channel that satisfies the data from Yellen and coworkers regarding the closed conformation of the intracellular gate (del Camino et al., 2005 and del Camino and Yellen, 2001) (see Supplemental Experimental Procedures). Figure 4 shows our best model of the PD of Kv1.2 in the resting state. The pore is closed tightly by V410 (V478 in Shaker) side chains in the PD tetramer, and the V410 side chain is exposed to the water-accessible intracellular environment (Figures 4A and 4B). The S6 segment stays kinked at the conserved PVP-motif region in the resting state (Figures 4C and 4D). Comparison of our resting-state PD model with the Kv1.2 open-state structure (Long et al., 2005a) shows that the S6 closing movement involves a side movement of its intracellular part, which puts V410 and S6 residues downstream closer to the channel pore axis, so that the Cα atom of V410 moves ~5 Å between the open and closed states (Figures 4C and 4D).

We next modeled the resting-state position of the S4-S5 linker. The S4-S5 linker is proposed to interact specifically with S6 and to couple the voltage-dependent VSD movement to PD opening and closing (Lu et al., 2001 and Lu et al., 2002). Maintaining the Kv1.2 open-state structure location of S4-S5 relative to S6 (Long et al., 2005a) (see Supplemental Experimental Procedures) and closing the gate, as we modeled above, results in a radial whole-body movement of S4-S5 by about 5  6 Å, which preserves its location between the hydrophobic and polar layers of the membrane. This movement of S4-S5 parallel to the plane of the membrane is significantly different from ~10 Å downward movement of the N-terminal end of the S4-S5 linker proposed earlier based on a KcsA-derived PD model of the closed state (Long et al., 2005b). To complete

the resting-state PD model, we modeled the S5 region between S324 (S392 in Shaker) and V339 (V407 in Shaker) de novo using the Rosetta-Membrane method (Yarov-Yarovoy et al., 2006b). The model predicts that the intracellular part of S5 moves between the resting and open states, so that the N-terminal residue of S5 (M325 in Kv1.2; M393 in Shaker) is displaced by ~8 Å.

## Voltage-Sensing Domain Modeling in the Resting State

We used the Rosetta-Membrane domain assembly method to build a resting-state model of the Kv1.2 VSD around our new resting-state model of the Kv1.2 PD (see Supplemental Experimental Procedures). The modeling was constrained by our fluorescence scan data in one way only. The fluorescence scan indicates that the outer half of S3 (S3b), S4, and the S3-S4 loop go through significant motion during voltage sensing. We therefore modeled these segments de novo in order to allow them to reorganize from their positions in the open state. Based on the omega current data (Tombola et al., 2007), we constrained the position of the extracellular end of S4 to be near the extracellular end of S5 and S6 from the adjacent subunit and placed R1 in S4 (R294 in Kv1.2) close to E1 in S2 (E226 in Kv1.2).

We examined the ten largest clusters of models generated by the Rosetta-Membrane method, and the center model from the fourth largest cluster was selected as the best coarse-grained model based on the available experimental data (see Supplemental Experimental Procedures). An all-atom version of that model was subsequently generated with the high-resolution Rosetta-Membrane method (Barth et al., 2007) (see Supplemental Experimental Procedures). Figures 5A and 5B show our refined model of the Kv1.2 in the resting state. The model bears resemblance to earlier models (Chanda et al., 2005, Durell et al., 1998 and Yarov-Yarovoy et al., 2006a), although the detailed positions of the VSD and PD segments differ (see Discussion). The S4 is tilted and positioned 3 5 Å further down, and the extracellular part of S3 is moved away from S1 and S2 compared to the earlier Kv1.2 resting-state model (Yarov-Yarovoy et al., 2006a). The first gating-charge-carrying arginine in S4 (R1), constrained to be near E1 in S2, forms a salt bridge with it (Figures 5C and 5D), placing R1 at the bottom of the extracellular water-accessible vestibule in the VSD, in agreement with data suggesting that this residue is accessible to external MTS reagents in the resting state (Larsson et al., 1996). The third gating-charge-carrying arginine (R3) and S308 in S4 (S376 in Shaker) face the intracellular water-accessible vestibule in the VSD (Figures 5C and D), in agreement with data suggesting that they are accessible to internal MTS reagents in the resting state (Larsson et al., 1996). The resting-state model accounts well for the omega scan data (Tombola et al., 2007): residues that had a steric effect on the amplitude of the omega current form a cluster in the core of the VSD, with A291 (A359 in Shaker) and R294 (R362 in Shaker) in S4 facing S1 and S2, while residues that had an electrostatic effect form a cluster near the extracellular end of S4 (Figure 6A).

Our open and closed models are in good agreement with experiments on the KvAP channel (Ruta et al., 2005). Mapping biotin-avidin accessibility data from KvAP onto our models shows that the location of the residues fits within 2 4 Å (FigureS2). The exception to this match is for the resting state at the intracellular end of S4, most likely due to a different tilt of the S4-S5 linker. In our resting-state model, it is positioned parallel to the plane of the membrane (see Results), while in KvAP there may be more of a tilt (for discussion see Supplemental Text). In addition, our resting-state model is compatible with recently reported disulfide bonding results (Campos et al., 2007), which suggested close proximity between Shaker's R1 (R362 in Shaker; R294 in Kv1.2) and one residue in S1 (I241 in Shaker; l177 in Kv1.2) and another in S2 (I287 in Shaker; l230 in Kv1.2). Our resting-state model shows that the homologous residues in Kv1.2 are within Cβ-Cβ distances observed between cysteines that are able to form disulfide bonds in flexible proteins (Careaga and Falke, 1992): with a distance from the Kv1.2 homolog of R1 (R294) of ~7 Å to I177 in S1 and ~11 Å to I230 in S2. Finally, our resting-state model is also compatible with the recent experimental analysis of the down state of KAT1 (Grabe et al., 2007) (though using a different sequence alignment than the one proposed by those authors, see Supplemental Text and Figure S3).

**Agreement of the Resting-State Model with Fluorescence Data**

A comparison between the open- and resting-state models shows significant difference between conformations of the extracellular part of S3 and S4, with a relative motion between the helices, consistent with the detection of ΔFs at the interface between them (Figures 3C and 6B). The averaged global movement for segments S1, S2, S3, and S4 was calculated from the displacement between the resting- and open-state models for every residue with a ΔF and was plotted in Figure 6D. The extent of global movement for each segment is strikingly similar to the patterns of fluorescence data reported for that segment (compare Figure 6D with Figures 3A and 3B).

Mapping the ΔF data onto the models (Figures 6B and 6C) reveals that in the open state the majority of positions with a large ΔF are exposed to the extracellular side of the membrane, while positions with small ΔFs are buried within the protein or lipid environment. For most residues in S3 and S4, the sign and amplitude of the ΔF correlates well with the sign and amplitude of the change in solvent-accessible surface area of the residue between the resting and open states (ΔSASA) (Figure 6E, red symbols). Negative ΔFs correlate with an increase in residue solvent-accessible surface area, and positive ΔFs correlate with a decrease in residue solvent-accessible surface area when Shaker Kv channel goes from the resting to open state. A few residues fell into a parallel outlying distribution (Figure 6E, gray symbols). Half of these

residues are at the boundary between S3 and the S3-S4 linker, where the ΔF could be affected by a loop-to-helix transition from the resting-state model to the open-state model. The other half of the residues lie at the interface between S3 and S4, where the ΔF could be affected by rotation of S4 relative to S3.

## Discussion

### Conformational Changes in the VSD during Gating

While X-ray crystal structures of the open state of the Kv channels have been obtained (Jiang et al., 2003a and Long et al., 2005a), the resting-state structure of these channels remains unknown. Several models have been proposed for the mechanism of voltage-dependent gating that drives channels between the resting/closed and activated/open states (Tombola et al., 2006). The paddle model suggests that S4 coupled to S3 moves 15 20 Å across the lipid bilayer (Jiang et al., 2003b and Ruta et al., 2005). The helical screw model suggests that S4 rotates and moves 3 13 Å across the lipid bilayer and that gating-charge-carrying arginines make sequential interactions with the negatively charged residues in the VSD during the transition (Catterall, 1986, Gandhi and Isacoff, 2002, Guy and Seetharamulu, 1986, Lecar et al., 2003 and Yarov-Yarovoy et al., 2006a). The transporter model suggests that S4 moves 2 4 Å across the lipid bilayer and that gating-charge-carrying arginines sense a transmembrane field focused by high dielectric aqueous crevices resulting from other conformational changes in the VSD (Chanda et al., 2005). Here, we use a combination of real-time fluorescence measurements of conformational changes and a variety of modeling approaches to build structural models of the resting/closed and activated/open states of the Kv1.2 channel. Our models are compatible with many of the prior results and provide plausible explanations for the conformational changes underlying voltage sensing and for the mechanism by which changes in the VSD are propagated to the PD.

We carried out a large-scale fluorescence scan of the outer surface of the Shaker channel that revealed patterns of protein motion during the voltage-sensing transition. Large ΔFs observed along substantial lengths of S3 and S4 suggest a major coordinated rearrangement, as proposed in the paddle model. However, the environment changes detected at the interface between S3 and S4 indicate that these helices also move relative to one another, and not as a rigid body. Importantly, the majority of the S3 and S4 positions that were studied reported a very good correlation between the magnitude of the ΔF and magnitude of the change in residue environment (ΔSASA) (Figure 6E). This is especially striking because per residue information from the fluorescence scan was not used to constrain the modeling.

73

The pattern of ΔFs observed for residues on S1 and S2 suggests that these segments do not substantially change their environment during activation. For example, if S3 and S4 moved as proposed in the original paddle model, they would lie flush against S1 and S2 in the open state, but pivot/tilt down in the resting state. From the perspective of S1 and S2 there would be a transition on one surface of each helix from a proteinaceous environment to a lipid environment. In the transporter model, residues in S1 and S2 would be expected to face a protein-packed environment in one state and a large aqueous lake in the other. In both of these scenarios, residues on S1 and S2 would undergo a large environment change. In our models, the majority of the extracellularly accessible residues in S1 and S2 are separated from S3 and S4 by an aqueous environment in both the activated/open and resting/closed states, meaning that there is no great environment change. This is consistent with the small ΔFs observed at a small number of positions in S1 and S2. This is the first structural model that can explain the heterogeneity of ΔFs observed in the VSD.

Comparison of our refined Kv1.2 resting- and open-state models provides a view of the dominant conformational changes occurring in the voltage sensor upon gating (Figure 7A and Supplemental Movies). S4 moves as a tilting screw, rotating ~180° clockwise (when viewed from the extracellular side of the membrane), moving up vertically by 6 8 Å, and changing tilt angle from ~60° to ~35° in response to depolarization. The magnitude of the vertical motion in S4 varies from ~0 Å for S308 (S376 in Shaker) to ~14 Å for S289 (S357 in Shaker) and is estimated to be ~8 Å for R1 (R294 in Kv1.2; R362 in Shaker), ~10 Å for R2 (R297 in Kv1.2; R365 in Shaker), ~10 Å for R3 (R300 in Kv1.2; R368 in Shaker), and ~7 Å for R4 (R371 in Shaker) (see Table S1). Though this was not imposed as a constraint in the modeling, symmetry arises naturally concerning the position of the gating-charge-carrying arginines in the open and resting states with respect to the extracellular and intracellular edges of the membrane. In the open state, the distances from the extracellular edge of the 30 Å thick membrane are ~6 Å for R1, ~8 Å for R2, ~11 Å for R3, and ~16 Å for R4, while in the resting state the distances from the intracellular edge to the membrane are ~6 Å for R4, ~8 Å for R3, ~11 Å for R2, and ~15 Å for R1. This symmetry suggests that the most energetically optimal position of the S4 arginines in the open and resting state of the VSD is within the same distance from the extracellular and intracellular side of the membrane. S1, S2, and S3 move around S4 in a clockwise direction (viewed from the extracellular side of the membrane), as proposed earlier (Yarov-Yarovoy et al., 2006a). The screw motion of S4 agrees with earlier energy-transfer data on Shaker (Cha et al., 1999 and Glauner et al., 1999) and prior sliding helix and helical screw models (Catterall, 1986, Durell et al., 1998 and Guy and Seetharamulu, 1986). The magnitude of the vertical movement of S4 is compatible with how hanatoxin appears to partition into the membrane to bind the resting state of the VSD (Phillips et al., 2005) and with the estimate of the movement of the first gating-charge-carrying arginine through the membrane electric field (Ahern and Horn, 2005). Importantly, the

magnitude of S4 movement is also compatible with previous data that appeared to be inconsistent. For instance, though the vertical translocation of S4 is larger than earlier distance estimates from energy transfer between donor-acceptor pairs of fluorophores (Chanda et al., 2005 and Posson et al., 2005), the data is consistent once one takes into account the length and flexibility of linkers via which the fluorophores were attached (Tombola et al., 2006). Similarly, while the vertical movement in the current model is smaller than the 15  20 Å that was proposed based on the biotin-avidin accessibility data in KvAP (Jiang et al., 2003b and Ruta et al., 2005), a closer look indicates that the KvAP accessibility data maps well onto our open- and resting-state models of Kv1.2 (Figure S2), except at the inner end of S4, which may be less tilted in KvAP (Tombola et al., 2005a and Yarov-Yarovoy et al., 2006a).


The cumulative gating charge that is moved across the membrane electric field in the transition between our models of the resting and activated states is estimated to be ~14 elementary charges per channel (Figure 7B), close to the ~13 elementary charges estimated experimentally in Shaker (Aggarwal and MacKinnon, 1996 and Seoh et al., 1996). The first four arginines in S4 contribute the most to the cumulative gating charge (Figure 7B), with the per subunit contribution being as follows: R1, 0.23e; R2, 0.61e; R3, 0.65e; and R4, 0.33e. This general conclusion agrees with earlier experimental work, although the values do not match the experimental values (Aggarwal and MacKinnon, 1996 and Seoh et al., 1996) precisely. It should be noted that the contribution of R1 to the gating charge has not been clearly defined experimentally. Measurements of gating charge in neutralizing mutations led to estimates ranging from 0 and 1e, which were uncertain because of possible indirect effects on other gating charges and complexities of more than one possible conducting state (Aggarwal and MacKinnon, 1996, Gandhi and Isacoff, 2002 and Seoh et al., 1996). MTS accessibility analysis has suggested that R1 goes from being fully exposed to the extracellular environment in activated state to being in between the intracellular and extracellular environment in the resting state (Baker et al., 1998, Larsson et al., 1996 and Yang et al., 1996), an interpretation supported by the observation that omega current flows in the resting state when R1 is substituted with a smaller uncharged side chain (Tombola et al., 2005b and Tombola et al., 2007), suggesting transfer of ~0.5e. Given this broad range of experimental interpretations it is difficult to assess the validity of our estimate of ~0.25e gating charge contribution of R1 from our Kv1.2 channel models. This value was arrived at by simply turning off the R1 charge in the PB continuum electrostatic calculations without relaxing the atomic coordinates of the closed and open states. A more realistic approach would allow the structure to readjust following this change, as a real site-directed charge-neutralizing mutation affects not only the charge at that site but also the distribution of neighboring charges if they are mobile. The quantitative differences may also arise from inaccuracies in side chain packing by the structural modeling method (Yarov-Yarovoy et al., 2006a and Yarov-Yarovoy et al., 2006b).

It is particularly noteworthy that, without a focused transmembrane field, a much larger translocation of S4 would be required to account for the gating charge. High dielectric aqueous regions contribute to focus the transmembrane field in both the open and closed conformation, thereby controlling the magnitude of the gating charge. In the open state, the field is focused toward the extracellular half of the membrane by the large central vestibule at the intracellular pore entrance. In the closed state, the field is again focused toward the extracellular half of the membrane, this time by the wide aqueous crevice that opens up at the center of the VSD under the tilted S4 helix. The existence of the latter had been deduced indirectly from experiments (Ahern and Horn, 2005, Chanda et al., 2005, Islas and Sigworth, 2001, Starace and Bezanilla, 2004 and Tombola et al., 2007).

**Molecular Model of the Voltage-Dependent Gating of Kv Channels**

Comparison of our resting-state model to the Kv1.2 open-state model (Long et al., 2005a) suggest a molecular mechanism of the voltage-dependent gating of Kv channels. The data available to date suggest that voltage-dependent gating involves two major sets of conformational change during the transition between the resting/closed and activated/open state: independent motions of the VSDs with transfer of most of the gating charge between the resting state and an activated-not-open state that keeps the intracellular PD gate closed (Bezanilla et al., 1994, del Camino et al., 2005, Horn et al., 2000, Ledwell and Aldrich, 1999, Pathak et al., 2005, Perozo et al., 1994, Schoppa and Sigworth, 1998 and Soler-Llavina et al., 2006), and a concerted opening transition of the VSD and PD, which transfers a minor component of the gating charge between the activated-not-open state and the state that opens the intracellular PD gate for ion conduction (del Camino et al., 2005, Mannuzzu and Isacoff, 2000, Pathak et al., 2005, Schoppa and Sigworth, 1998, Smith-Maxwell et al., 1998a, Smith-Maxwell et al., 1998b, Soler-Llavina et al., 2006 and Zagotta et al., 1994). The activated-not-open state is stabilized by S4's ILT residues (V369I, I372L, and S376T in Shaker; V301I, I304L, and S308T in Kv1.2) (Ledwell and Aldrich, 1999, Smith-Maxwell et al., 1998a and Smith-Maxwell et al., 1998b), which map on to one face of the S4 helix and have been proposed to face the neighboring subunit's S5 (Pathak et al., 2005). Complementary to this, a cluster of residues on the intracellular half of S5, which plays a role in the concerted gating transition, has been proposed to interact with the ILT residues (Soler-Llavina et al., 2006).

In our resting-state model, the ILT residues point from S4 into the intracellular water-accessible vestibule within the VSD and away from the S5 cluster (Figure 7C). The 180° turn and upward displacement of S4 would bring the ILT residues into contact with the S5 cluster if there were little or no motion in the PD. We propose this to represent the independent transition in the VSD from the resting to the active-not-open state. In our model, for the intracellular half of S6 to swing and open the gate, S5 must first tilt its intracellular end by ~7 Å tangentially around the

PD. Thus, we propose that the second major activation rearrangement involves tilting of S4 coupled to tilting of the intracellular half of the adjacent S5. This counterclockwise movement (viewed from the extracellular side of the membrane) would enable the S4-S5 linker and S6 in all four subunits to move together and open the intracellular gate of the pore.

Recent studies suggested a role of lipid phosphate groups in Kv channel gating, including interaction with S4 arginines (Ramu et al., 2006 and Schmidt et al., 2006). Our resting-state model, in which the arginines are shielded from the hydrocarbon core of the membrane by S1, S2, and S3, does not suggest interaction of the S4 arginines with lipid phosphate groups. Furthermore, during the rotational and translational movement of S4 between the resting and active-not-open conformations, the S4 arginines would still be oriented toward S1, S2, and S3 and away from the membrane (see Figure 7A and the Supplemental Movies). However, the final opening transition may place the first two arginines in contact with the extracellular lipid phosphate groups (Long et al., 2005b). This is consistent with the observation that KvAP cannot be activated in the absence of the negatively charged phospholipids (Schmidt et al., 2006), perhaps because lacking the stabilization provided by the interaction of the arginines with the lipid phosphate groups in the open state, it remains stuck in the activated-not-open conformation. Further experiments are necessary to test this hypothesis and to try to understand whether interactions between S4 arginines and lipid phosphate groups drive S4 tilt, and thus lead to the concerted opening transition of the PD.

**Comparison to Other Structural Models of Kv Channels**

Recently, several structural models of the open and resting state of the Kv channels have been proposed (Chanda et al., 2005, Durell et al., 2004, Grabe et al., 2007, Tombola et al., 2007 and Yarov-Yarovoy et al., 2006a). In addition, a conceptual model of the KvAP resting state was proposed in the paddle model of gating (Jiang et al., 2003b and Ruta et al., 2005). Our open- and resting-state Kv channel models suggest the following new details of the molecular mechanism of the voltage-dependent gating: (1) S4 moves vertically by about 6  8 Å (see Figure7A and the Supplemental Movies). Previously published complete structural models of the transmembrane region of the VSD in the open and/or closed states suggested significantly different magnitudes of the S4 vertical movement: ~2  4 Å (Chanda etal., 2005), 3 Å (Yarov-Yarovoy et al., 2006a), and 10  13 Å (Durell etal., 2004, Grabe et al., 2007 and Tombola et al., 2007). The previously published conceptual model of the KvAP resting state (Jiang et al., 2003b and Ruta et al., 2005) suggested ~15  20 Å vertical movement of the S4; (2) S3 moves relative to S1, S2, and S4 (Figure 7A and the Supplemental Movies). None of the previously published complete structural models suggested significant movement of the S3 relative to all the other VSD segments; (3) concerted movement of the S4, S5, S4-S5 linker, and S6 of all four subunits in the opening transition (see Discussion and the Supplemental Movies). None of the previously published

complete structural models of Kv channels suggested such a mechanism of the concerted opening transition. Despite the differences with the earlier models, we have shown that our models can account for much of the seemingly disparate earlier data that led to those divergent models, that it can uniquely account for our new fluorescence data, that it agrees, grosso modo, with what is known about gating charge contribution, and that it leads to a coherent mechanism by which voltage sensing is coupled to gating.

In conclusion, the movement underlying the gating mechanism emerging from the present analysis retains features of the three principal models proposed previously. The magnitude of S4 vertical movement is compatible with the earlier data and is ~6   8 Å larger than in the transporter model (2   4 Å), but smaller than in the paddle model (15   20 Å). As pictured in the helical screw model (Catterall, 1986 and Guy and Seetharamulu, 1986), the predominant movement is an axial rotation of S4 by ~180°. As in the transporter model (Chanda et al., 2005), high dielectric crevices contribute to focus the transmembrane field, thus increasing the gating charge that couples energetically the VSD to the membrane voltage. As emphasized in the paddle model (Jiang et al., 2003b), the S4 segment is partially exposed to the lipid environment; however, the S4 gating charges move through a   virtual gating pore   within the VSD, without being exposed directly to the nonpolar hydrocarbon core of the membrane. The compatibility of our Kv channel models with a wide body of data, a good deal of which had been previously thought to be contradictory, appears to resolve the controversy about the magnitude and character of the movement underlying voltage gating.


## Experimental Procedures

For detailed Experimental Procedures, please refer to the Supplemental Data.


### Fluorescence Recordings

Procedures for site-directed mutagenesis, in vitro transcriptions, RNA injections, oocyte preparation and injections, and labeling by TMRM were performed as described previously (Gandhi et al., 2000 and Pathak et al., 2005). Two-electrode voltage-clamp fluorometry was performed 1   2 days after oocyte injection as described in Mannuzzu etal. (1996), in bath solution composed of (in mM): 110 NaMES, 2 KMES, 2 CaMES2, and 10 HEPES (pH 7.5) or 20 NaMES, 90 KMES, 2 CaMES$_2$, and 10 HEPES (pH 7.5).


### Data Analysis

Data analysis was done with the Axon Laboratory programs pClamp8 and Clampfit 9.2 (Axon Instruments) and custom-prepared Matlab programs as described in the Supplemental

Experimental Procedures. Each fluorescence trace was baseline subtracted and bleach corrected. The fluorescence response to the depolarizing step was fit by a double-exponential function. The two components of the fit correspond to channel activation and slow inactivation (see Results). The amplitude of the fit to the activation component (represented as $\Delta F$) was averaged across cells for a given site. $\Delta F$ values correspond to the conventionally used representation $\Delta F/F$ and are expressed as percent changes (Table 1).

**Modeling of the Kv1.2 Channel**

The Rosetta-Membrane method (Yarov-Yarovoy et al., 2006b and Barth et al., 2007) and the CHARMM program (Brooks et al., 1983) were used to model the Kv1.2 channel in the resting and activated-open states as described in the Supplemental Experimental Procedures. Coordinates of the Kv1.2 channel models are available in the Supplemental Data.

## Supporting Information

Supporting information is available at

http://www.cell.com/neuron/supplemental/S0896-6273(07)00720-9

## References

S.K. Aggarwal and R. MacKinnon, Contribution of the S4 segment to gating charge in the Shaker K+ channel, *Neuron* **16** (1996), pp. 1169 1177.

C.A. Ahern and R. Horn, Focused electric field across the voltage sensor of potassium channels, *Neuron* **48** (2005), pp. 25 29.

O.S. Baker, H.P. Larsson, L.M. Mannuzzu and E.Y. Isacoff, Three transmembrane conformations

and sequence-dependent displacement of the S4 domain in shaker K+ channel gating, *Neuron* **20** (1998), pp. 1283   1294.

P. Barth, J. Schonbrun and D. Baker, Efficient all-atom modeling of interactions, structural specificities and helical distortions in membrane proteins, *Proc. Natl. Acad. Sci. USA* (2007) in press.

F. Bezanilla, E. Perozo and E. Stefani, Gating of Shaker K+ channels: II. The components of gating currents and a model of channel activation, *Biophys. J.* **66** (1994), pp. 1011   1021.

B.R. Brooks, R.E. Bruccoleri, B.D. Olafson, D.J. States, S. Swaminathan and M. Karplus, CHARMM: A program for macromolecular energy minimization and dynamics calculations, *J. Comp. Chem.* **4** (1983), pp. 187   217.

F.V. Campos, B. Chanda, B. Roux and F. Bezanilla, Two atomic constraints unambiguously position the S4 segment relative to S1 and S2 segments in the closed state of Shaker K channel, *Proc. Natl. Acad. Sci. USA* **104** (2007), pp. 7904   7909.

C.L. Careaga and J.J. Falke, Thermal motions of surface alpha-helices in the D-galactose chemosensory receptor. Detection by disulfide trapping, *J. Mol. Biol.* **226** (1992), pp. 1219   1235.

W.A. Catterall, Voltage-dependent gating of sodium channels: Correlating structure and function, *Trends Neurosci.* **9** (1986), pp. 7   10.

A. Cha and F. Bezanilla, Characterizing voltage-dependent conformational changes in the Shaker K+ channel with fluorescence, *Neuron* **19** (1997), pp. 1127   1140.

A. Cha, G.E. Snyder, P.R. Selvin and F. Bezanilla, Atomic scale movement of the voltage-sensing region in a potassium channel measured via spectroscopy, *Nature* **402** (1999), pp. 809   813.

B. Chanda, O.K. Asamoah, R. Blunck, B. Roux and F. Bezanilla, Gating charge displacement in voltage-gated ion channels involves limited transmembrane movement, *Nature* **436** (2005), pp. 852   856.

R.B. Darman, A.A. Ivy, V. Ketty and R.O. Blaustein, Constraints on voltage sensor movement in the shaker K+ channel, *J. Gen. Physiol.* **128** (2006), pp. 687   699.

D. del Camino and G. Yellen, Tight steric closure at the intracellular activation gate of a voltage-gated K(+) channel, *Neuron* **32** (2001), pp. 649   656.

D. del Camino, M. Kanevsky and G. Yellen, Status of the intracellular gate in the activated-not-open state of shaker K+ channels, *J. Gen. Physiol.* **126** (2005), pp. 419   428.

S.R. Durell, Y. Hao and H.R. Guy, Structural models of the transmembrane region of voltage-gated and other K+ channels in open, closed, and inactivated conformations, *J. Struct. Biol.* **121** (1998), pp. 263   284.

S.R. Durell, I.H. Shrivastava and H.R. Guy, Models of the structure and voltage-gating mechanism of the shaker K+ channel, *Biophys. J.* **87** (2004), pp. 2116 2130.

C.S. Gandhi and E.Y. Isacoff, Molecular models of voltage sensing, *J. Gen. Physiol.* **120** (2002), pp. 455 463.

C.S. Gandhi, E. Loots and E.Y. Isacoff, Reconstructing voltage sensor-pore interaction from a fluorescence scan of a voltage-gated K+ channel, *Neuron* **27** (2000), pp. 585 595.

C.S. Gandhi, E. Clark, E. Loots, A. Pralle and E.Y. Isacoff, The orientation and molecular movement of a k(+) channel voltage-sensing domain, *Neuron* **40** (2003), pp. 515 525.

K.S. Glauner, L.M. Mannuzzu, C.S. Gandhi and E.Y. Isacoff, Spectroscopic mapping of voltage sensor movement in the Shaker potassium channel, *Nature* **402** (1999), pp. 813 817.

C. Gonzalez, F.J. Morera, E. Rosenmann, O. Alvarez and R. Latorre, S3b amino acid residues do not shuttle across the bilayer in voltage-dependent Shaker K+ channels, *Proc. Natl. Acad. Sci. USA* **102** (2005), pp. 5020 5025.

M. Grabe, H.C. Lai, M. Jain, Y. Nung Jan and L. Yeh Jan, Structure prediction for the down state of a potassium channel voltage sensor, *Nature* **445** (2007), pp. 550 553.

H.R. Guy and P. Seetharamulu, Molecular model of the action potential sodium channel, *Proc. Natl. Acad. Sci. USA* **83** (1986), pp. 508 512.

R. Horn, S. Ding and H.J. Gruber, Immobilizing the moving parts of voltage-gated ion channels, *J. Gen. Physiol.* **116** (2000), pp. 461 476.

L.D. Islas and F.J. Sigworth, Electrostatics and the gating pore of Shaker potassium channels, *J. Gen. Physiol.* **117** (2001), pp. 69 89.

Y. Jiang, A. Lee, J. Chen, V. Ruta, M. Cadene, B.T. Chait and R. MacKinnon, X-ray structure of a voltage-dependent K+ channel, *Nature* **423** (2003), pp. 33 41.

Y. Jiang, V. Ruta, J. Chen, A. Lee and R. MacKinnon, The principle of gating charge movement in a voltage-dependent K+ channel, *Nature* **423** (2003), pp. 42 48.

P.J. Kraulis, MOLSCRIPT: a program to produce both detailed and schematic plots of protein structures, *J. Appl. Cryst.* **24** (1991), pp. 946 950.

H.P. Larsson, O.S. Baker, D.S. Dhillon and E.Y. Isacoff, Transmembrane movement of the shaker K+ channel S4, *Neuron* **16** (1996), pp. 387 397.

H. Lecar, H.P. Larsson and M. Grabe, Electrostatic model of S4 motion in voltage-gated ion channels, *Biophys. J.* **85** (2003), pp. 2854 2864.

J.L. Ledwell and R.W. Aldrich, Mutations in the S4 region isolate the final voltage-dependent

cooperative step in potassium channel activation, *J. Gen. Physiol.* **113** (1999), pp. 389   414.

S.Y. Lee, A. Lee, J. Chen and R. MacKinnon, Structure of the KvAP voltage-dependent K+ channel and its dependence on the lipid membrane, *Proc. Natl. Acad. Sci. USA* **102** (2005), pp. 15441   15446.

Y. Li-Smerin, D.H. Hackos and K.J. Swartz, α-helical structural elements within the voltage-sensing domains of a K(+) channel, *J. Gen. Physiol.* **115** (2000), pp. 33   50.

S.B. Long, E.B. Campbell and R. Mackinnon, Crystal structure of a mammalian voltage-dependent Shaker family K+ channel, *Science* **309** (2005), pp. 897   903.

S.B. Long, E.B. Campbell and R. Mackinnon, Voltage sensor of Kv1.2: structural basis of electromechanical coupling, *Science* **309** (2005), pp. 903   908.

Z. Lu, A.M. Klem and Y. Ramu, Ion conduction pore is conserved among potassium channels, *Nature* **413** (2001), pp. 809   813.

Z. Lu, A.M. Klem and Y. Ramu, Coupling between voltage sensors and activation gate in voltage-gated K+ channels, *J. Gen. Physiol.* **120** (2002), pp. 663   676.

L.M. Mannuzzu and E.Y. Isacoff, Independence and cooperativity in rearrangements of a potassium channel voltage sensor revealed by single subunit fluorescence, *J. Gen. Physiol.* **115** (2000), pp. 257   268.

L.M. Mannuzzu, M.M. Moronne and E.Y. Isacoff, Direct physical measure of conformational rearrangement underlying potassium channel gating, *Science* **271** (1996), pp. 213   216.

E.A. Merritt and D.J. Bacon, Raster3D: Photorealistic molecular graphics, *Methods Enzymol.* **277** (1997), pp. 505   524.

M. Pathak, L. Kurtz, F. Tombola and E. Isacoff, The cooperative voltage sensor motion that gates a potassium channel, *J. Gen. Physiol.* **125** (2005), pp. 57   69.

E. Perozo, L. Santacruz-Toloza, E. Stefani, F. Bezanilla and D.M. Papazian, S4 mutations alter gating currents of Shaker K channels, *Biophys. J.* **66** (1994), pp. 345   354.

E.F. Pettersen, T.D. Goddard, C.C. Huang, G.S. Couch, D.M. Greenblatt, E.C. Meng and T.E. Ferrin, UCSF Chimera    a visualization system for exploratory research and analysis, *J. Comput. Chem.* **25** (2004), pp. 1605   1612.

L.R. Phillips, M. Milescu, Y. Li-Smerin, J.A. Mindell, J.I. Kim and K.J. Swartz, Voltage-sensor activation with a tarantula toxin as cargo, *Nature* **436** (2005), pp. 857   860.

D.J. Posson, P. Ge, C. Miller, F. Bezanilla and P.R. Selvin, Small vertical movement of a K+ channel voltage sensor measured with luminescence energy transfer, *Nature* **436** (2005), pp. 848

851.

Y. Ramu, Y. Xu and Z. Lu, Enzymatic activation of voltage-gated potassium channels, *Nature* **442** (2006), pp. 696  699.

V. Ruta, J. Chen and R. MacKinnon, Calibrated measurement of gating-charge arginine displacement in the KvAP voltage-dependent K+ channel, *Cell* **123** (2005), pp. 463  475.

M.F. Sanner, A.J. Olson and J.C. Spehner, Reduced surface: an efficient way to compute molecular surfaces, *Biopolymers* **38** (1996), pp. 305  320.

D. Schmidt, Q.X. Jiang and R. MacKinnon, Phospholipids and the origin of cationic gating charges in voltage sensors, *Nature* **444** (2006), pp. 775  779.

N.E. Schoppa and F.J. Sigworth, Activation of Shaker potassium channels. III. An activation gating model for wild-type and V2 mutant channels, *J. Gen. Physiol.* **111** (1998), pp. 313  342.

S.A. Seoh, D. Sigg, D.M. Papazian and F. Bezanilla, Voltage-sensing residues in the S2 and S4 segments of the Shaker K+ channel, *Neuron* **16** (1996), pp. 1159  1167.

C.J. Smith-Maxwell, J.L. Ledwell and R.W. Aldrich, Role of the S4 in cooperativity of voltage-dependent potassium channel activation, *J. Gen. Physiol.* **111** (1998), pp. 399  420.

C.J. Smith-Maxwell, J.L. Ledwell and R.W. Aldrich, Uncharged S4 residues and cooperativity in voltage-dependent potassium channel activation, *J. Gen. Physiol.* **111** (1998), pp. 421  439.

G.J. Soler-Llavina, T.H. Chang and K.J. Swartz, Functional interactions at the interface between voltage-sensing and pore domains in the Shaker K(v) channel, *Neuron* **52** (2006), pp. 623  634.

D.M. Starace and F. Bezanilla, A proton pore in a potassium channel voltage sensor reveals a focused electric field, *Nature* **427** (2004), pp. 548  553.

F. Tombola, M.M. Pathak and E.Y. Isacoff, How far will you go to sense voltage?, *Neuron* **48** (2005), pp. 719  725.

F. Tombola, M.M. Pathak and E.Y. Isacoff, Voltage-sensing arginines in a potassium channel permeate and occlude cation-selective pores, *Neuron* **45** (2005), pp. 379  388.

F. Tombola, M.M. Pathak and E.Y. Isacoff, How does voltage open an ion channel?, *Annu. Rev. Cell Dev. Biol.* **22** (2006), pp. 23  52.

F. Tombola, M.M. Pathak, P. Gorostiza and E.Y. Isacoff, The twisted ion-permeation pathway of a resting voltage-sensing domain, *Nature* **445** (2007), pp. 546  549.

N. Yang, A.L. George Jr. and R. Horn, Molecular basis of charge movement in voltage-gated sodium channels, *Neuron* **16** (1996), pp. 113  122.

V. Yarov-Yarovoy, D. Baker and W.A. Catterall, Voltage sensor conformations in the open and closed states in ROSETTA structural models of K(+) channels, *Proc. Natl. Acad. Sci. USA* **103** (2006), pp. 7292 7297.

V. Yarov-Yarovoy, J. Schonbrun and D. Baker, Multipass membrane protein structure prediction using Rosetta, *Proteins* **62** (2006), pp. 1010 1025.

W.N. Zagotta, T. Hoshi and R.W. Aldrich, Shaker potassium channel gating. III: Evaluation of kinetic models for activation, *J. Gen. Physiol.* **103** (1994), pp. 321 362.

## Figures and Table

**Figure 1. Fluorescence Scan Data Set**

**Figure 2. Fast ΔF in VSD Reports on Activation**

**Figure 3. Pattern of ΔFs in the Voltage-Sensing Domain**

**Figure 4. Resting-State Model of the PD and the S4-S5 Linker of the Kv1.2 Channel**
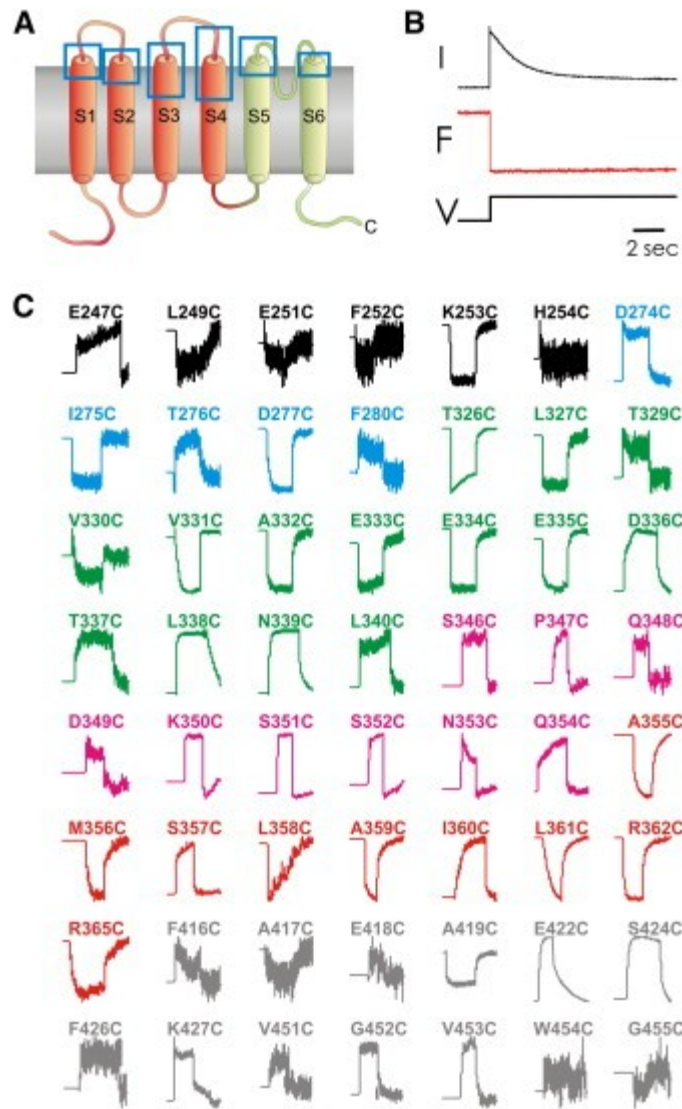
**Figure 5. Resting-State Model of the VSD of the Kv1.2**

**Figure 6. Experimental Data on Shaker Kv Channel Mapped onto the Refined Kv1.2 Resting-State Model**

**Figure 7. Comparison of the Kv1.2 Models of the Activated (Open) and Resting (Closed) States**

**Table 1. Fluorescence Data Set**

**Figure 1**

**Figure 1. Fluorescence Scan Data Set**

**(A)** Schematic diagram marking the regions of the Shaker channel included in the fluorescence scan. One subunit of the channel is shown, with the VSD in orange and the PD in green. Blue boxes mark the regions included in the fluorescence scan.

**(B)** Voltage step from a holding potential of −80 mV to a voltage between 0 and 50 mV for several seconds (V) opens the channel and slow inactivates it (I) while eliciting a fluorescence change from TMRM attached to the channel (F). At the site shown, TMRM fluorescence only tracks activation, not the process of slow inactivation.

**(C)** Fluorescence reports from the 56 positions at which ΔFs were detected. Each trace represents the mean of traces from three cells. The position of attachment of the fluorophore is indicated by a label on the top of each trace, with the following color scheme for labels: black, S1; blue, S2; green, S3; magenta, S3-S4; red, S4; gray, pore domain. The pre-step duration shown for each trace is 4 s and serves as the scale bar.
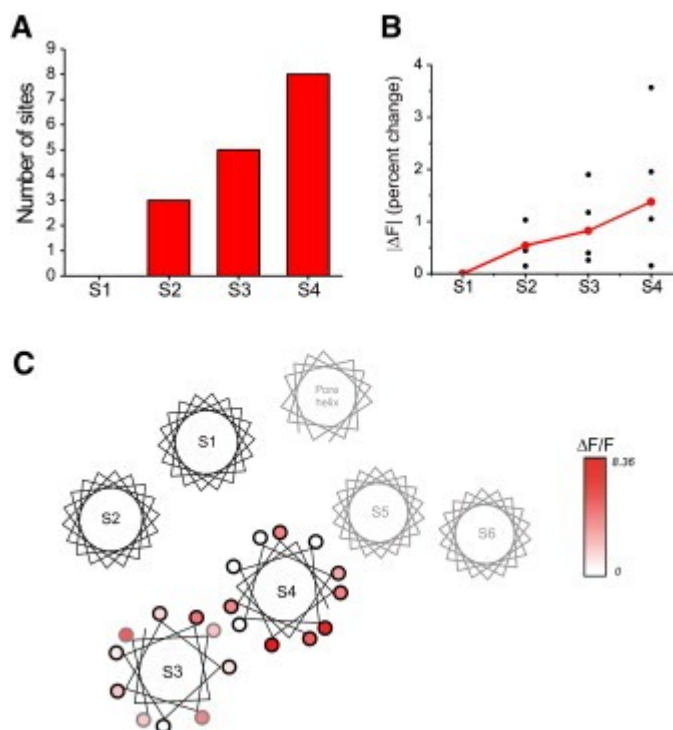
**Figure 2**
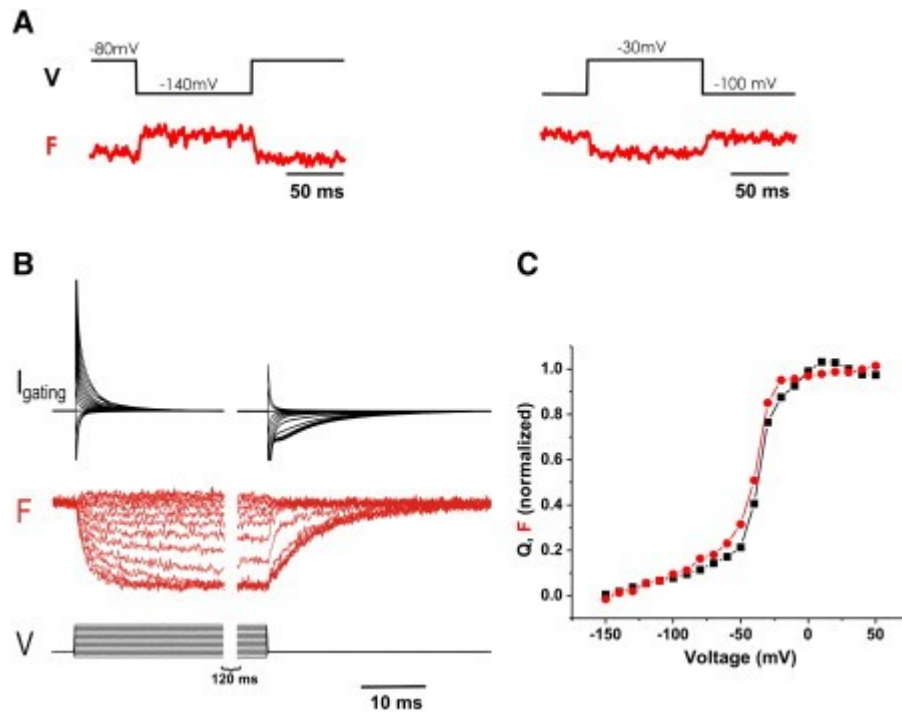
**Figure 2. Fast ΔF in VSD Reports on Activation**

**(A)** Fluorescence signals in response to a hyperpolarizing step (left) and a depolarizing step that does not open the channels (right) from TMRM attached to T276C. These channels open at ~−10 mV (data not shown).

**(B)** Gating currents (top) and fluorescence changes (middle) elicited from a site (I275C) that exhibits fast fluorescence changes in response to a family of voltage pulses (bottom). Holding potential is −80 mV, and the voltages steps range from −150 mV to +50 mV. Note the similarity in time course of gating currents and fluorescence changes.

**(C)** Normalized gating charge movement (black) and normalized steady-state fluorescence changes (red) show similar voltage-dependence properties. Points plotted are from data shown in part (B).

**Figure 3**



**Figure 3. Pattern of ΔFs in the Voltage-Sensing Domain**

**(A)** Number of fluorophore attachment positions from each helical region of the VSD of the Kv1.2 structure with a detectable ΔF. See Figure S6 for the sequence alignment used for S1 and S3 helices.

**(B)** Magnitude of the fast fluorescence components (ΔF) for the four helical segments of the voltage-sensing domain. The definition of helical segments is based on the crystal structure of the Kv1.2 channel, and alignments as discussed in Supplemental Experimental Procedures and shown in Figure S6. ΔF was computed as described in the Data Analysis section of Supplemental Experimental Procedures. Each black point represents a different site, and its value is the median ΔF of all cells tested for that site. The red points denote the mean of all sites for a given segment.

**(C)** Magnitude of fluorescence changes from S3 and S4 color coded according to the scale shown on the right and mapped onto a helical net diagram corresponding to a view of the channel's open-state model from the extracellular side of the membrane. Only the VSD of one subunit and the PD of its adjacent subunit are shown for clarity. S3 sites outlined in gray indicate sites that are not resolved in the Kv1.2 crystal structure but that are modeled as helical in the Rosetta-Membrane open-state model.

89
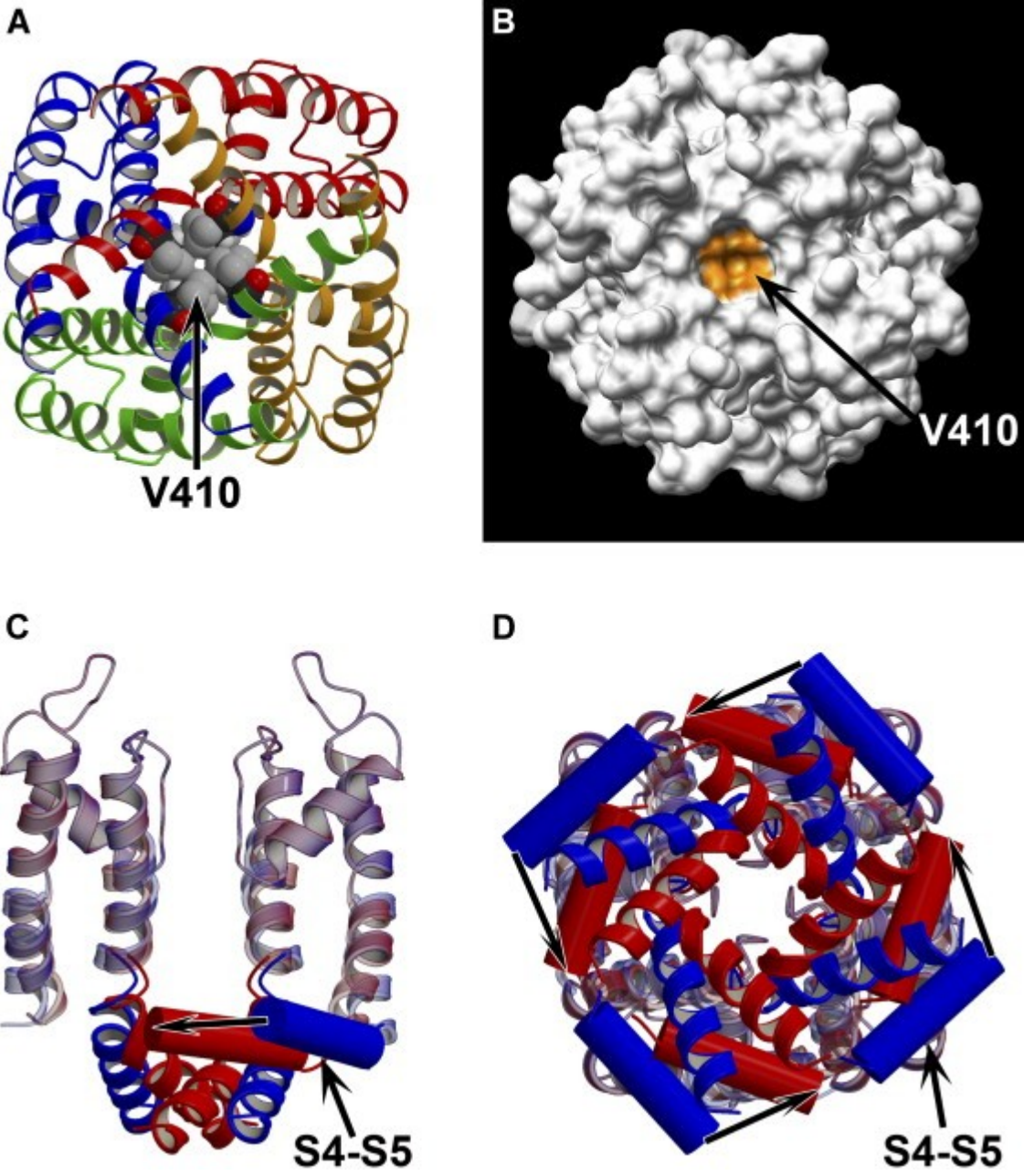
**Figure 4**

**Figure 4. Resting-State Model of the PD and the S4-S5 Linker of the Kv1.2 Channel**
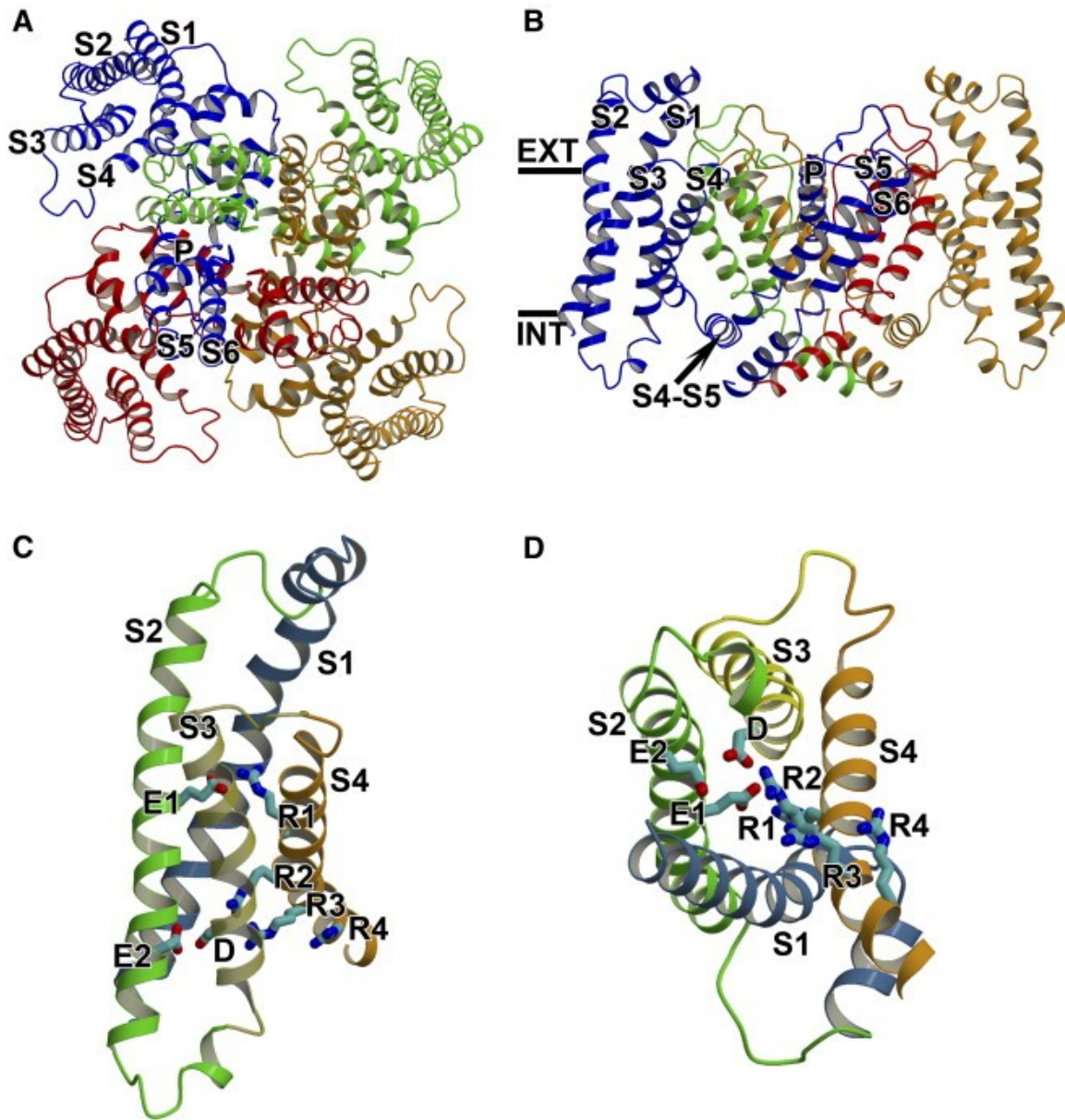
**(A)** View from the intracellular side of the membrane of the ribbon representation of the PD model of Kv1.2 in the resting state. Side chains of V410 (V478 in Shaker) in S6 are shown in space-filling representation.

**(B)** View from the intracellular side of the membrane of the molecular surface representation of the PD of Kv1.2 in the resting state. Side chains of V410 are colored in orange.

**(C)** Side view of the cylinder representation of the S4-S5 linker and ribbon representation of the PD of the Kv1.2 in the resting (shown in red) and open (shown in blue) state superimposed over the selectivity filter residues. Only two opposing subunits forming the PD are shown for clarity.

**(D)** View of the models shown in (C) from the intracellular side of the membrane. All four subunits are shown. Panels (A), (C), and (D) were generated using Molscript (Kraulis, 1991) and Raster3D (Merritt and Bacon, 1997). Panel (B) was generated using Chimera (Pettersen et al., 2004 and Sanner et al., 1996).

**Figure 5**

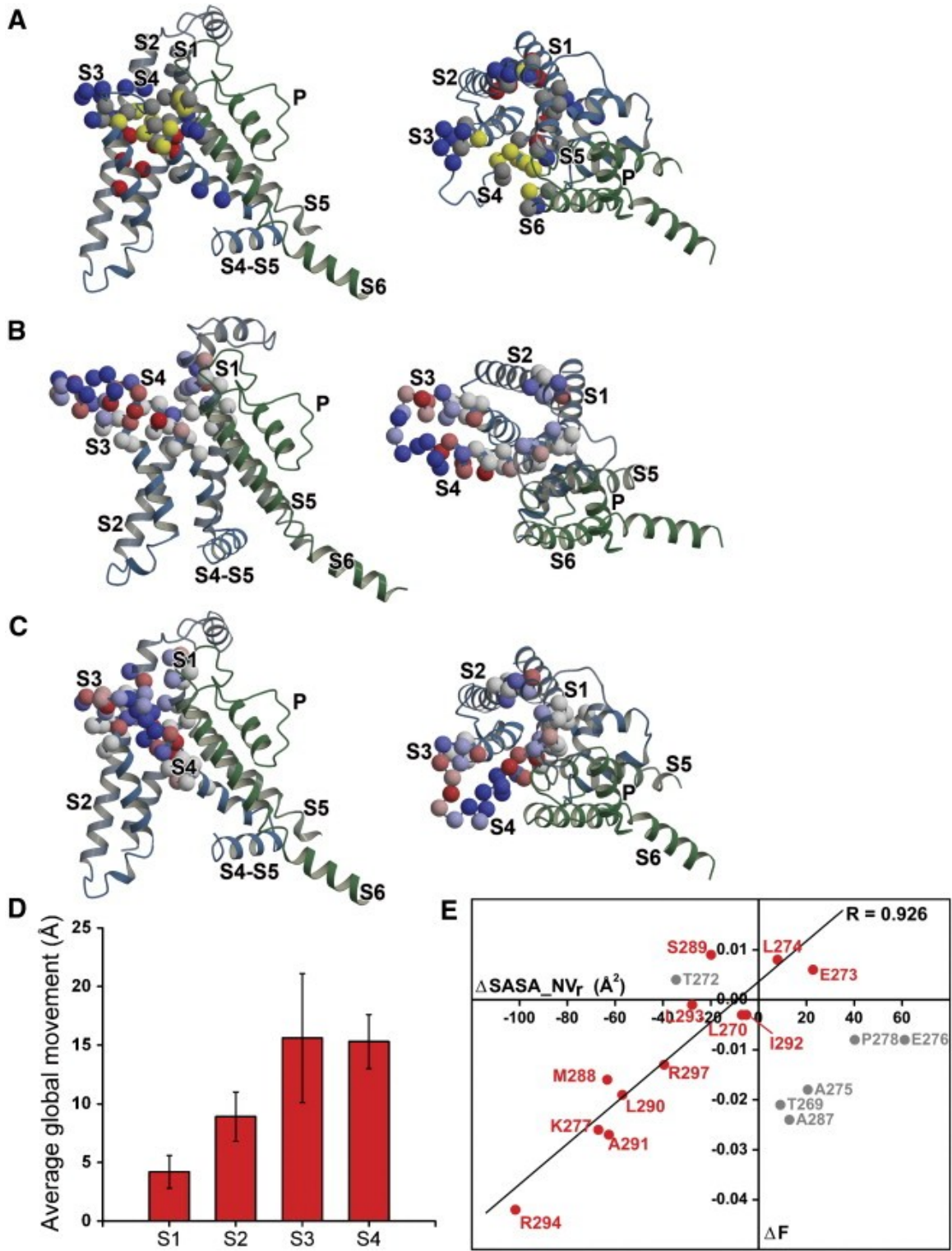**Figure 5. Resting-State Model of the VSD of the Kv1.2**

**(A)** View of the ribbon representation of the Kv1.2 resting-state model from the extracellular side of the membrane. All four subunits are colored individually. Segments S1-S6 for blue colored subunit are labeled accordingly.

**(B)** View of the model shown in (A) from the side of the membrane. The VSD is shown only for blue and orange colored subunits for clarity. Segments S1-S6 and S4-S5 linker for blue colored subunit are labeled accordingly. Extracellular and intracellular edges of the membrane are marked by solid bars and labeled  EXT  and  INT,  respectively.

**(C)** Side view of the VSD segments S1 through S4 only (colored individually) of the model shown in (A). Side chains of gating-charge-carrying arginines in S4 (labeled R1 through R4), E226 (E283 in Shaker, labeled E1) and E236 (E293 in Shaker, labeled E2) in S2, and D259 (D316 in Shaker, labeled D) in S3 shown in stick representation. Blue, red, and cyan colored atoms in the side chains shown represent nitrogen, oxygen, and carbon atoms, respectively.

**(D)** View of the model shown in (C) from the intracellular side of the membrane. The figure was generated using Molscript (Kraulis, 1991) and Raster3D (Merritt and Bacon, 1997).

**Figure 6**

**Figure 6. Experimental Data on Shaker Kv Channel Mapped onto the Refined Kv1.2 Resting-State Model**

(**A**) Positions in the VSD and PD of the Shaker Kv channel studied by Tombola et al. (Tombola et al., 2007) mapped onto the ribbon representation of the Kv1.2 resting-state model. Only a single VSD from one subunit and PD from the adjacent subunit are shown from the side of the membrane (left panel) and extracellular side of the membrane (right panel). Segments S1-S6 and S4-S5 linker are labeled accordingly. Cα carbon atoms of the Kv1.2 residues corresponding to the Shaker Kv residues studied are shown as spheres and are colored based on their effect on the amplitude of the omega current as reported by Tombola et al. (Tombola et al., 2007) according to the following scheme: red, positions that had steric effect; yellow, positions that had electrostatic effect; blue, positions that had null effect; gray, positions that had indirect effect.

(**B and C**) Positions in the VSD and PD of the Shaker Kv channel studied in the fluorescence scan (Table 1) mapped onto the ribbon representation of the Kv1.2 open-state (B) and resting-state (C) models. Only a single VSD from one subunit and PD from the adjacent subunit are shown from the side of the membrane (left panel) and extracellular side of the membrane (right panel). Segments S1-S6 and S4-S5 linker are labeled accordingly. Cα carbon atoms of the Kv1.2 residues corresponding to the Shaker Kv residues studied are shown as spheres and are colored based on a sign of fluorescence change (ΔF) reported in Table 1 according to the following scheme: red, positions that reported $\Delta F < -0.03$; red to white, positions that reported $-0.03 < \Delta F < 0$; white, positions that reported $\Delta F = 0$; white to blue, positions that reported $0 < \Delta F < 0.03$; blue, positions that reported $\Delta F > 0.03$.

(**D**) Amplitude of average global movement between the resting and open states of the VSD residues studied for each VSD segment. Global movement of each VSD segment was calculated from an average difference in position of Cα atoms of VSD residues studied in the Kv1.2 between the resting (closed) and activated (open) state models superimposed over Cα atom positions of GYG residues in the selectivity filter (G376, Y377, and G378 in the Kv1.2; G444, Y445, and G446 in Shaker). Error bars represent standard deviation.

(**E**) Change in the amplitude of the fast fluorescence (ΔF) for the S3 and S4 residues only plotted versus change in residue solvent-accessible surface area between the resting and open states normalized to the ratio of TMRM volume to residue side chain volume at each position studied (ΔSASA_NV$_r$) (see Supplemental Experimental Procedures). The red points represent the S3 and S4 residues that are not forming a part of the S3-S4 loop and are not at the interface between the S3 and S4 in either the resting or closed state. The gray points represent the S3 and S4 residues that are forming a part of the S3-S4 loop or are at the interface between the S3 and S4 in either resting or closed state. The linear regression fit is plotted for the red points only.

**Figure 7**
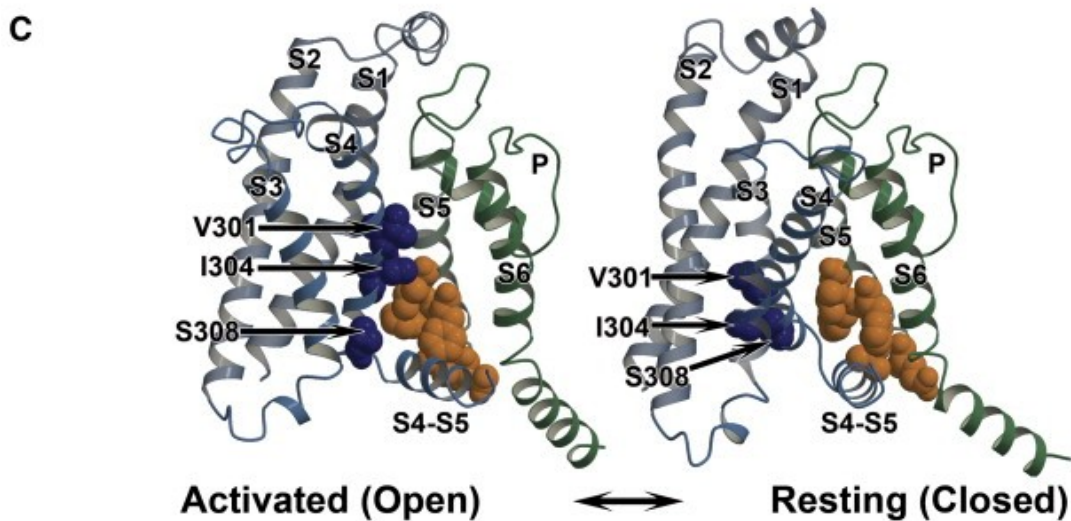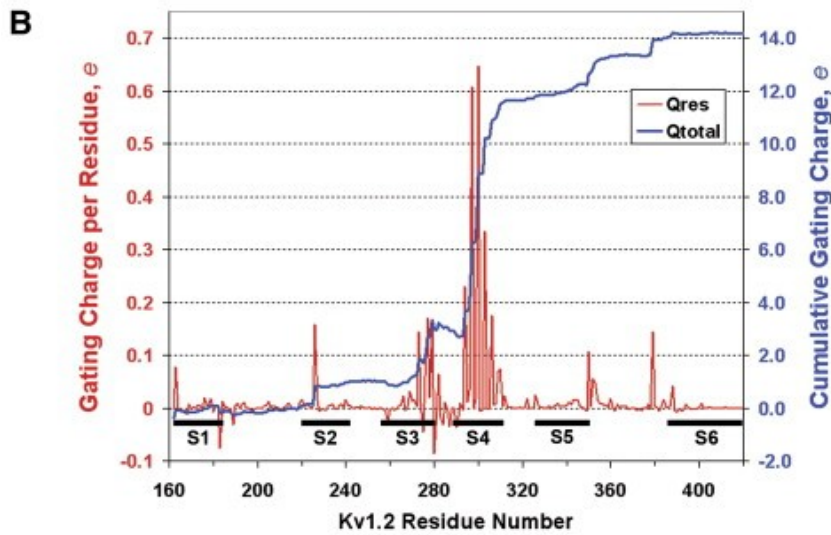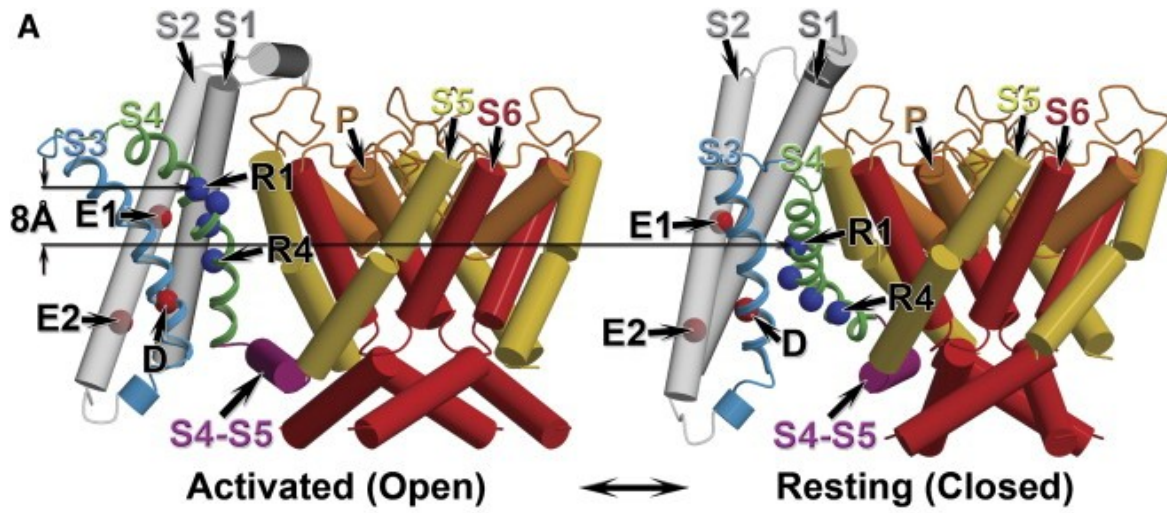
**Figure 7. Comparison of the Kv1.2 Models of the Activated (Open) and Resting (Closed) States**

**(A)** View of the cylinder representation of the Kv1.2 open-state (left panel) and resting-state (right panel) models. Only a single VSD is shown attached to a tetramer of the PD for clarity. Transmembrane segments S1 and S2 are colored gray, and segments S3 through S6 and the P loop are colored by a rainbow scheme from blue to red. The S4-S5 linker is colored purple. Positions of C$\alpha$ carbon atoms of the gating-charge-carrying arginines in S4 (labeled as R1 and R4 and colored in blue), E226 in S2 (E283 in Shaker; labeled as E1 and colored in red) and E236 in S2 (E293 in Shaker; labeled as E2 and colored in red), and D259 in S3 (D316 in Shaker; labeled D and colored red) are shown in sphere representation. Vertical translation of the first gating-charge-carrying arginine (R1) between the activated (open) and resting (closed) states along the membrane normal vector is indicated by arrows. The S3 and S4 are shown in ribbon representation. Segments S1-S6 and the P loop for one subunit are labeled accordingly.

**(B)** Cumulative gating charge in a tetramer (blue) and gating charge per residue in a single subunit (red) transferred across the membrane electric field between the resting to open state plotted as a function of Kv1.2 residue position.

**(C)** View of the ribbon representation of the Kv1.2 open state (left panel) and resting state (right panel) models of the VSD from one subunit and the PD from the adjacent subunit from the side of the membrane. Segments S1-S6 and the S4-S5 linker are labeled accordingly. Positions in the Shaker Kv channel studied by Soler-Llavina et al. (Soler-Llavina et al., 2006) mapped onto the Kv1.2 open-state structure (Long et al., 2005a) and Kv1.2 resting-state model. The Kv1.2 residues corresponding to the ILT triple mutant (Ledwell and Aldrich, 1999, Smith-Maxwell et al., 1998a, and Smith-Maxwell et al., 1998b) (colored in dark blue) and intracellular cluster of the S5 residues studied by Soler-Llavina et al. (Soler-Llavina et al., 2006) (colored in orange) are shown in space-filling representation. Residue numbers in the ILT triple mutant positions correspond to the Kv1.2 channel sequence. The figure was generated using Molscript (Kraulis, 1991) and Raster3D (Merritt and Bacon, 1997).

**Table 1. Fluorescence Data Set**

| | Region | Shaker Residue | Kv1.2 Residue | Mean ΔF | Standard Deviation | Standard Error | n | Max ΔF |
|---|---|---|---|---|---|---|---|---|
| 1 | S1 | E247 | E183 | 0.00164 | 0.00067 | 0.00038 | 3 | 0.00241 |
| 2 | S1 | L249 | L185 | −0.00178 | 0.00089 | 0.00031 | 8 | −0.00311 |
| 3 | S1 | E251 | I187 | 0.00423 | 0.0053 | 0.002 | 7 | 0.01584 |
| 4 | S1 | F252 | F188 | −0.00127 | 0.00107 | 0.00038 | 8 | 0.00288 |
| 5 | S1 | K253 | R189 | −0.01351 | 0.00833 | 0.00315 | 7 | −0.02918 |
| 6 | S1 | H254 | D190 | 0.0037 | 0.00248 | 0.00111 | 5 | 0.00692 |
| 7 | S2 | D274 | S217 | 0.00935 | 0.00566 | 0.00214 | 7 | 0.02172 |
| 8 | S2 | I275 | F218 | −0.01685 | 0.01039 | 0.00465 | 5 | −0.03017 |
| 9 | S2 | T276 | T219 | 0.00142 | 0.00071 | 0.00036 | 4 | 0.00222 |
| 10 | S2 | D277 | D220 | −0.00355 | 0.00164 | 0.00062 | 7 | −0.00505 |
| 11 | S2 | F280 | F223 | 0.0148 | 0.01648 | 0.00521 | 10 | 0.05425 |
| 12 | S3 | T326 | T269 | −0.02076 | 0.01267 | 0.00448 | 8 | −0.04094 |
| 13 | S3 | L327 | L270 | −0.00265 | 0.00109 | 0.00044 | 6 | −0.00386 |
| 14 | S3 | T329 | T272 | 0.00388 | 0.00024 | 0.00012 | 4 | 0.00411 |
| 15 | S3 | V330 | E273 | 0.00579 | 0.00489 | 0.00219 | 5 | 0.01423 |
| 16 | S3 | V331 | L274 | 0.00807 | 0.00572 | 0.00256 | 5 | 0.01248 |
| 17 | S3 | A332 | A275 | −0.01797 | 0.01107 | 0.00418 | 7 | −0.03487 |
| 18 | S3 | E333 | E276 | −0.00814 | 0.00837 | 0.00342 | 6 | −0.02489 |
| 19 | S3 | E334 | K277 | −0.0258 | 0.0194 | 0.00792 | 6 | −0.06302 |
| 20 | S3 | E335 | P278 | −0.00767 | 0.00358 | 0.00207 | 3 | −0.01033 |
| 21 | S3-S4 | D336 | | 0.00696 | 0.00586 | 0.00339 | 3 | 0.01272 |
| 22 | S3-S4 | T337 | | 0.02245 | 0.02109 | 0.01055 | 4 | 0.04326 |
| 23 | S3-S4 | L338 | | 0.02325 | 0.01153 | 0.00471 | 6 | 0.04184 |
| 24 | S3-S4 | N339 | | 0.04264 | 0.02223 | 0.01112 | 4 | 0.07384 |
| 25 | S3-S4 | L340 | | 0.00453 | 0.0011 | 0.00064 | 3 | 0.00579 |
| 26 | S3-S4 | S346* | | 0.01239 | 0.00615 | 0.00275 | 5 | 0.02 |
| 27 | S3-S4 | P347* | E279 | 0.00679 | 0.00434 | 0.00194 | 5 | 0.01044 |
| 28 | S3-S4 | Q348* | D280 | 0.0234 | 0.01207 | 0.00493 | 6 | 0.04108 |
| 29 | S3-S4 | D349* | A281 | 0.00546 | 0.00228 | 0.00114 | 4 | 0.00809 |
| 30 | S3-S4 | K350* | Q282 | 0.01705 | 0.00775 | 0.00258 | 9 | 0.02829 |
| 31 | S3-S4 | S351* | Q283 | 0.0703 | 0.02181 | 0.0069 | 10 | 0.1154 |
| 32 | S3-S4 | S352* | G284 | 0.02089 | 0.0088 | 0.00359 | 6 | 0.03135 |
| 33 | S3-S4 | N353* | Q285 | 0.04482 | 0.02435 | 0.00921 | 7 | 0.07764 |
| 34 | S3-S4 | Q354 | Q286 | 0.03495 | 0.02354 | 0.00832 | 8 | 0.08101 |
| 35 | S4 | A355* | A287 | −0.02414 | 0.01365 | 0.00483 | 8 | −0.04552 |
| 36 | S4 | M356* | M288 | −0.0161 | 0.0079 | 0.00354 | 5 | −0.02187 |
| 37 | S4 | S357 | S289 | 0.00918 | 0.00751 | 0.00306 | 6 | 0.02067 |
| 38 | S4 | L358* | L290 | −0.01899 | 0.00616 | 0.00252 | 6 | −0.02892 |
| 39 | S4 | A359* | A291 | −0.02654 | 0.01974 | 0.00547 | 13 | −0.06753 |
| 40 | S4 | I360* | I292 | −0.003 | 0.00626 | 0.00313 | 4 | −0.01114 |
| 41 | S4 | L361* | L293 | −0.00075 | 0.00355 | 0.00145 | 6 | −0.00458 |

**Table 1.** *Continued*

| | Region | Shaker Residue | Kv1.2 Residue | Mean ΔF | Standard Deviation | Standard Error | n | Max ΔF |
|---|---|---|---|---|---|---|---|---|
| 42 | S4 | R362* | R294 | −0.04178 | 0.01476 | 0.0066 | 5 | −0.0658 |
| 43 | S4 | R365* | R297 | −0.01287 | 0.01037 | 0.00464 | 5 | −0.03082 |
| 44 | S5 | F416 | F348 | 0.00157 | 0.00044 | 0.00018 | 6 | 0.00214 |
| 45 | S5 | A417* | A349 | −0.00229 | 0.00235 | 0.00118 | 4 | −0.00572 |
| 46 | S5 | E418* | E350 | 0.0414 | 0.02247 | 0.00917 | 6 | 0.06231 |
| 47 | P | A419* | A351 | −0.06475 | 0.07468 | 0.04312 | 3 | −0.1508 |
| 48 | P | E422* | R354 | 0.08361 | 0.04435 | 0.01676 | 7 | 0.1359 |
| 49 | P | S424* | S356 | 0.03267 | 0.02596 | 0.01161 | 5 | 0.07009 |
| 50 | P | F426* | F358 | 0.00582 | 0.00245 | 0.00173 | 2 | 0.00756 |
| 51 | P | K427 | P359 | 0.01724 | 0.01064 | 0.00284 | 14 | 0.03765 |
| 52 | P | V451 | T383 | 0.0007 | 0.00075 | 0.00027 | 8 | 0.00168 |
| 53 | P | G452 | T384 | 0.01661 | 0.01129 | 0.00292 | 15 | 0.03591 |
| 54 | S6 | V453 | I385 | 0.00434 | 0.00394 | 0.00149 | 7 | 0.00998 |
| 55 | S6 | W454 | 386 | 0.00071 | 0.0004 | 0.00023 | 3 | 0.00117 |
| 56 | S6 | G455* | G387 | −0.00366 | 0.00242 | 0.0014 | 3 | −0.00581 |

We did not observe fluorescence changes at positions F244 (F180), C245 (C181), or L246 (L182) in S1; F279 (F222), L281 (I224), or I282 (V225) in S2; F324 (F267), I325 (I268), or A328 (G271) in S3; V363 (V295), I364 (I296), L366 (L298), V367 (V299), or V369 (V301) in S4; F425 (Q357), S428 (S360), or A432 (A364) in the pore loop regions. We did not obtain expression of the cysteine mutants at T248 (T184) or P250 (P186) in S1; P278 (P221) or E283 (E226) in S2; G420 (D352), N423 (D355), P430 (P362), K456 (K388), or I457 (I389) in the pore domain. For sites marked with * the data were taken from experiments reported in Gandhi et al. (2000). For details on how the ΔF values were computed, please see Supplemental Experimental Procedures, section Data Analysis, Evaluating parameters for sites.

# Appendix 2
## A New Sensor for Detecting Postsynaptic Calcium

GCaMP 1.6 had proven to be superior in signal fidelity to GCaMP 1.3 and Cameleon for detecting responses in the antennal lobe. In 2006, the improved GCaMP 2 was announced, reported to be 5 times brighter than GCaMP 1.6 (Tallini et al., 2006). Transgenic flies of GCaMP 2, as well as a membrane-bound version, CD8 GCaMP 2, were made. The latter was developed with the reasoning that having the sensor close to the membrane would put it directly in contact with the large changes of calcium that occur at the membrane.

Contrary to expectations, GCaMP 2 was no brighter than GCaMP 1.6. Many lines containing independent UAS insertions were tested; most failed to produce homozygous flies, potentially an indication of GCaMP 2 toxicity. Of the lines that produced homozygous flies, their responses to calcium transients appeared similar to GCaMP 1.6. Projection neurons expressing the membrane-bound version did not visibly differ in their response characteristics from those expressing the cytosolic version. This is possibly because the dendrites of projection neurons in the antennal lobe are so thin that the two versions are similarly exposed to calcium influxes when the neuron is excited. Nonetheless, the distribution of the sensor was different. The dendrites of projection neurons expressing the membrane-bound version appeared more like neuropil, whereas those of neurons with the cytosolic version had more processes visible (Fig. 1). Additionally, CD8-GCaMP 2 was not expressed within the axons of projection neurons. Interestingly, CD8-GFP, which contains two of the three subdomains found within CD8-GCaMP 2, brightly labels axons in antennal lobe projection neurons (Jefferis et al., 2001).

Dr. Einat Peled expressed the membrane-bound version of the sensor in fly muscle, where studies on the postsynaptic response of the neuromuscular junction were taking place. Compared to the sensor being used at the time, Synapcam, CD8-GCaMP 2 exhibited much larger responses. However, muscles expressing this sensor appeared unhealthy. Dr. Peled attached a Shaker C-terminal domain to the construct so that it would localize specifically to the post-synaptic density, as was the case for Synapcam. Flies expressing this construct appeared much healthier. Subsequent work by Dr. Peled indicates that this reporter is capable of reporting single synaptic events with high fidelity, something Synapcam was incapable of (Fig. 2). As part of the original screening of potential postsynaptic reporters years earlier, Dr. Giovanna Guerrero had tested CD8-GCaMP-Sh. However, this reporter had minimal fluorescence so was discarded at the time.

In conclusion, while targeting GCaMP 2 to the membrane did not improve signal quality within the CNS, it led to the development of a new sensor that could report single synaptic events at the neuromuscular junction.

# References

Jefferis GSXE, Marin EC, Stocker RF, Luo L  (2001)  Target neuron prespecification in the olfactory map of Drosophila. Nature 414:204-208

Tallini YN, Ohkura M, Choi B, Ji G, Imoto K, Doran R, Lee J, Plan P, Wilson J, Xin H, Sanbe A, Gulick J, Mathai J, Robbins J, Salama G, Nakai J, Kotlikoff MI  (2006)  Imaging cellular signals in the heart in vivo: Cardiac expression of the high-signal Ca2+ indicator GCaMP2. Proceedings of the National Academy of Sciences of the United States of America 103:4753-4758
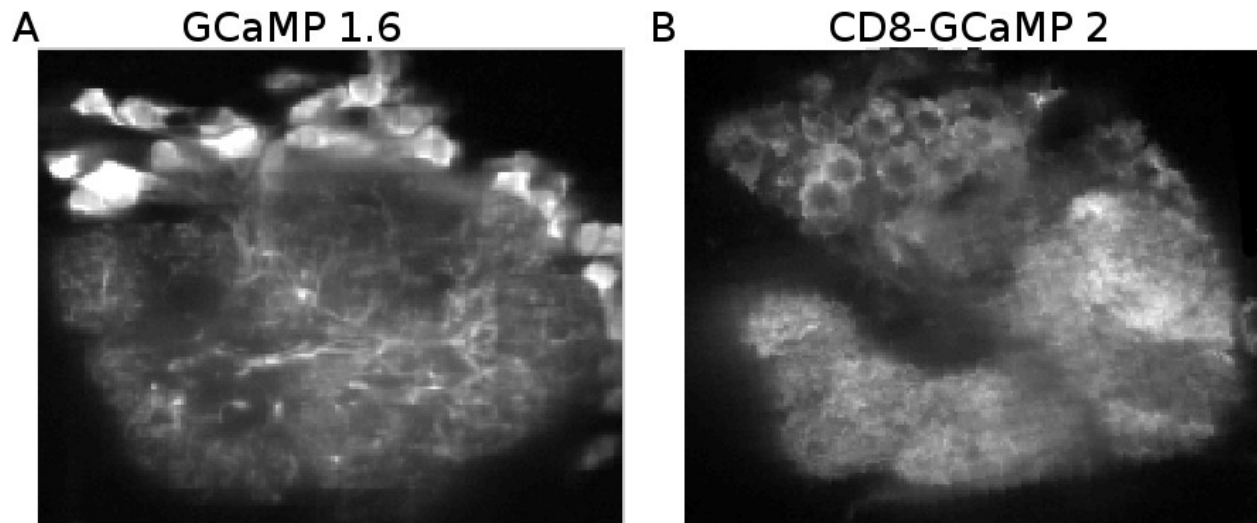
# Figures

**Figure 1. Distribution of cytosolic and membrane-bound versions of calcium reporters**

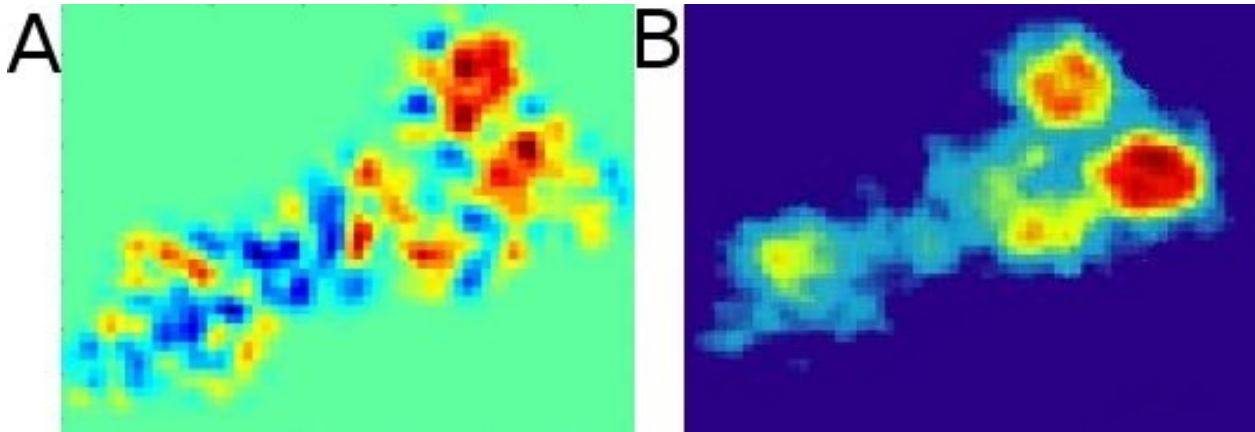**Figure 2. Responses of the originally used postsynaptic calcium sensor, Synapcam.**

**Figure 3. Responses of the improved postsynaptic calcium sensor based on GCaMP 2.**
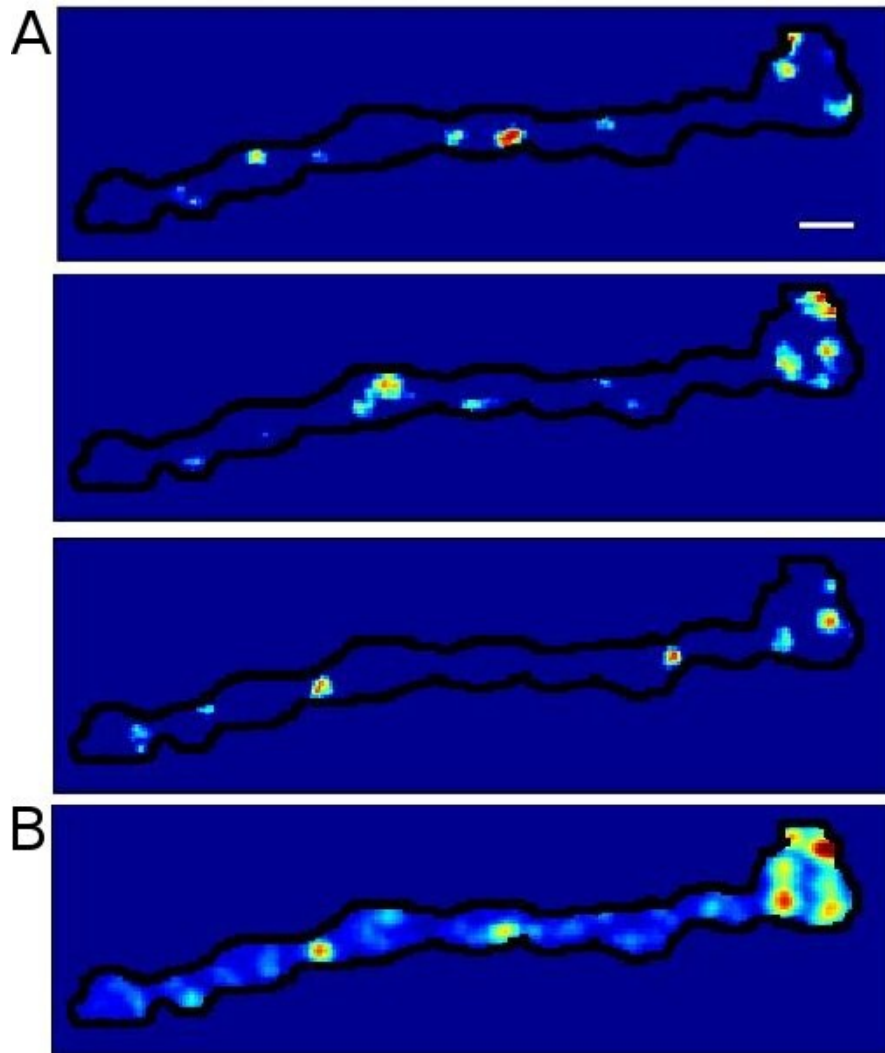
Figure 1



**Figure 1. Distribution of cytosolic and membrane-bound versions of calcium reporters. A)** Expression of GCaMP 1.6 in projection neurons. Note the relatively bright cell bodies (lining the upper part of the antennal lobe) and the visibility of dendritic processes. This pattern is similar to the expression pattern of GCaMP 2. **B)** Expression of CD8-GCaMP 2 in projection neurons. Note the relatively dim cell bodies. Levels of fluorescence were relatively homogeneous within glomeruli, but appeared somewhat variable among glomeruli.

**Figure 2**



**Figure 2. Responses of the originally used postsynaptic calcium sensor, Synapcam. A)** ΔF/F map of sensor response to single stimulation of motor neuron. Mottled appearance results from high image noise. Contiguous red regions in upper right represent activated regions. **B)** ΔF/F map for the same neuromuscular junction, averaged over 100 stimulations. Increased signal-to-noise ratio reveals relatively homogeneous circular zones, corresponding to regions activated by different boutons. Regional variations in intensity reflect variations in release probability and quantal size. Data was acquired on an epifluorescence microscope by Dr. Giovanna Guerrero.

**Figure 3**



**Figure 3. Responses of the improved postsynaptic calcium sensor based on GCaMP 2. A)**
ΔF/F maps of sensor responses to single stimulation of motor neuron, three trials. Warm-colored
punctate regions are thought to be responses to release from single active zones. Note variability
of release sites from trial to trial. Scale bar, 5 microns. **B)** ΔF/F map for the same neuromuscular
junction, averaged over 105 stimulations. Punctate regions are still visible within regions
postsynaptic to single boutons. Variations in spot intensity reflect variations in release probability
and quantal size, each of which can be quantified by analyzing responses over multiple trials.
Images were acquired on a confocal microscope and were generated by Dr. Einat Peled.

# Appendix 3
# Strategies for Handling Digital Data

Computers are becoming indispensable for all stages of scientific investigation, from data acquisition, to analysis, to presentation. Developing an integrated organizational framework for handling data can greatly streamline this process. Here I present some principles that I found most useful for this framework. I provide specific examples within the context of interpreting the response properties of glomeruli in the antennal lobe (Chapter 2).

**Digitize the lab notebook**

Every piece of data is associated with two forms of information. The first is a raw record of the system's behavior, captured by a scientific apparatus and typically stored as a file on a computer. The second is a description of the experimental conditions that correspond to the data collected. These descriptors, known as metadata, are typically recorded in a laboratory notebook. By digitizing these metadata and associating them with their corresponding raw collected data, one can automate and expedite the process of analysis. This is because one can then write computer programs that scan these metadata tags and pool information from data files that match specified criteria. While this process introduces the overhead of transcribing metadata and writing computer programs, it is very useful when processing very large data sets that can benefit from exploratory data analysis.

By organizing metadata into the appropriate hierarchy, data entry is minimized. Furthermore, any functions that scan the resultant data structure are often simpler and more elegant. Figure 1 shows the organization and content of one such data hierarchy for data collected from the antennal lobe.

**Process data in multiple stages**

Advances in data collection have led to the generation of very large data files. Fluorescence image stacks collected from the antennal lobe could be more than 50 megabytes in size. Extracting information from a large number of such files is very demanding on computational resources. It is thus advantageous to pre-process raw data and save it in a separate file that is used for all subsequent analyses (Fig. 2). The goal of such pre-processing is to retain from the original data all of the information that could be important for further analysis. This eliminates the need to repeat many memory- and time-intensive processes, such as motion correction or manual annotation of data. This allows the investigator to rapidly collect statistics and generate visualizations upon this pre-processed data set without having to repeatedly perform the preliminary stage of curation (Fig. 3).

When performing exploratory data analysis, data visualization can facilitate the discovery of patterns. One can subsequently modify experimental protocols that highlight or facilitate the interpretation of these patterns. Analyzing the new data may in turn require the updating of computer programs. Thus the data collection and analysis cycle can be viewed as an iterative process.

**Standardize variable samples**

Pooling data from many preparations can require a method to standardize data. For example, performing spatial analyses on the antennal lobe requires the alignment of multiple antennal lobes of slightly different shapes and sizes (Suppl. Fig. 1 in Chapter 2). Developing a coordinate system to consistently index antennal lobes allows the generation of average maps and the comparison of spatial data collected in different conditions.

**Find suitable metrics**

Finally, one must develop metrics that quantify an effect. Ideally, such metrics would highlight the effect and be interpretable in a biological context. Sometimes, the most obvious metrics do not convey the pattern, requiring the development of alternative quantifiers. For example, glomerulus DA1 responds in a different spatial pattern to ipsilateral and contralateral nerve stimulation, unlike other glomeruli. One would expect that the correlation between the activity patterns to be much lower than that for other glomeruli. However, this was not the case, most likely because the calculated correlation was obscured by pixel noise. However, the observation that the spatial extent of the response to ipsilateral nerve stimulation was larger than that for contralateral nerve stimulation resulted in an alternative metric that was based on the weighted average distance from the center of response (Fig. 4). Using this metric generated a significant difference between DA1 and other glomeruli. This is because this metric took into account the spatial relationship between the pixels within a glomerulus and this resulted in the metric being more resilient to noise.

**Future developments**

The analysis presented in this thesis was implemented in Matlab. However, Python is a free, open-source programming platform for which many analysis and visualization libraries are being developed that rival Matlab. As data acquisition equipment becomes more sophisticated, the magnitude of data to analyze will necessitate the development of an integrated digital platform for data handling. There is also a movement toward online data sharing (e.g. http://crcns.org/). While the standardization of data collected from multiple laboratories will be challenging, it is a necessary step for a holistic understanding of diverse brain processes. Finally, work in the field of machine learning promises to revolutionize the extraction of patterns from the burgeoning data sets being generated in neuroscience.
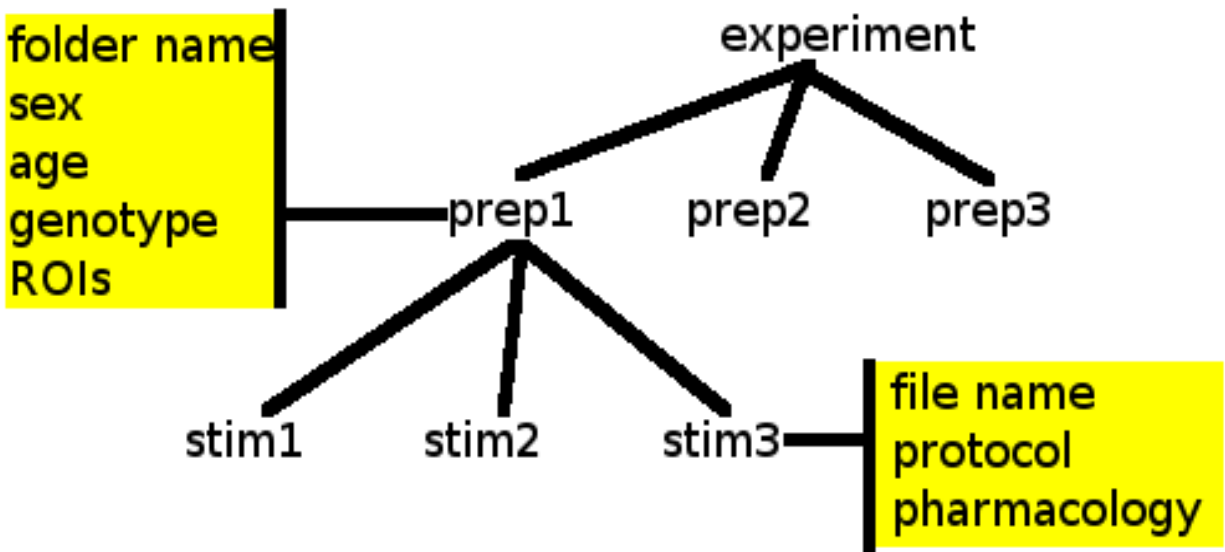
# Figures

**Figure 1. Organizing metadata into a hierarchy.**

**Figure 2. Pre-processing of raw data.**

**Figure 3. Data organization enables rapid and flexible processing.**

**Figure 4. Choosing a metric to quantify an effect.**

Figure 1



**Figure 1. Organizing metadata into a hierarchy.** Metadata is stored within a variable with a tree structure. The structure above represents the specific data structure used for experiments on the antennal lobe. The variable 'experiment' is an array containing information on different preparations. 'Prep1' stores metadata for one preparation, the fields of which are represented in the attached yellow box. In addition, it contains an array of metadata associated with different stimulation epochs for the preparation. The metadata associated with an individual stimulation epoch is indicated in the lower yellow box. Together, the two yellow boxes represent all of the metadata that is needed to interpret a file; however, by organizing it into a hierarchy, it is represented in a more parsimonious fashion. In addition, using a numerical array of subfields for preparations and stimulations allows one to write programs that sequentially iterate through them.
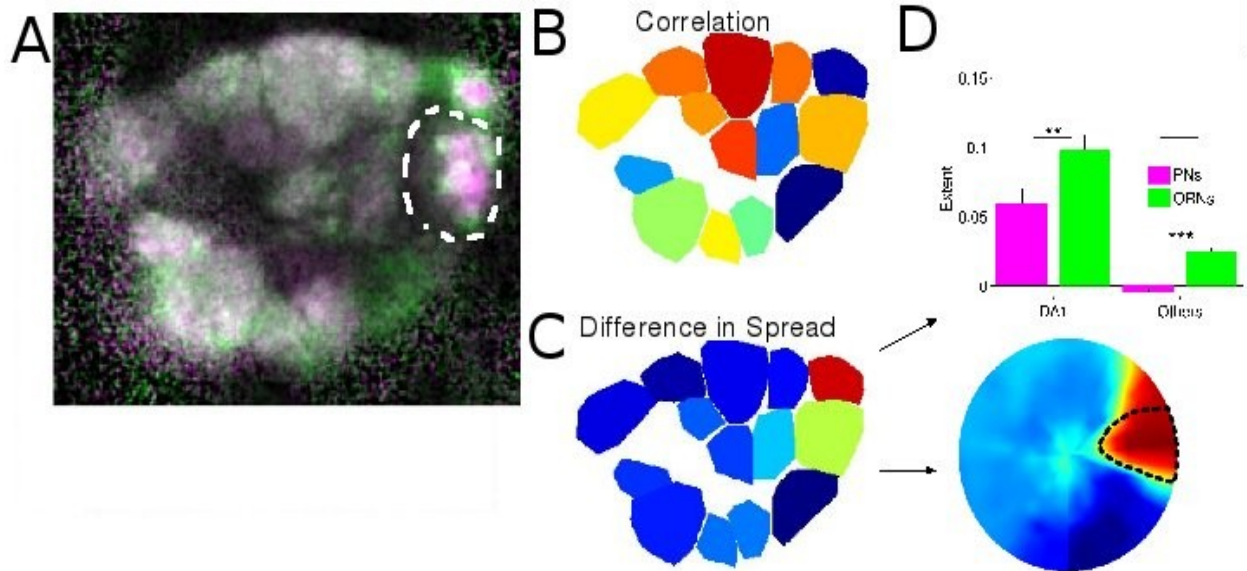
**Figure 2**
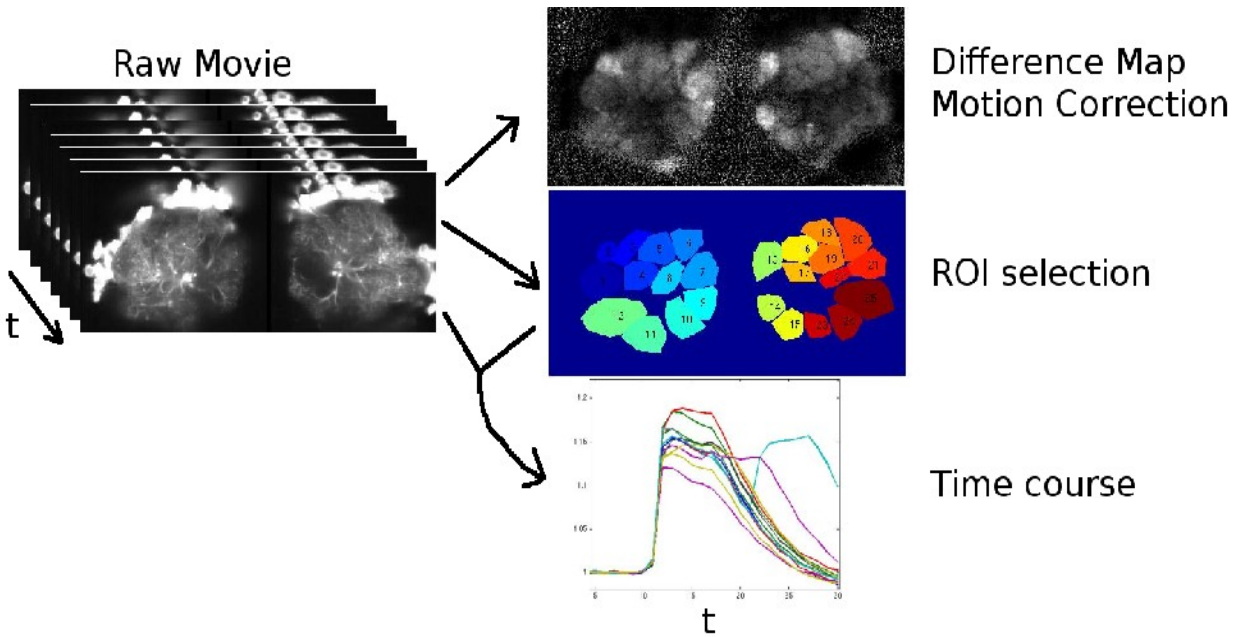


**Figure 2. Pre-processing of raw data.** All of the information that can be relevant for future analyses is extracted and stored within a new file. In the case of the antennal lobe, the original time-series of fluorescence in response to a stimulus was reduced to 1) a motion-corrected map of the response; 2) the boundaries of all glomeruli. This process was best done manually, so storing the location of all ROI's required performing ROI selection only once; 3) the timecourses of responses within each glomerulus. Together, 1) and 3) can be used to approximately reconstruct all of the relevant data within the raw image stack, while tremendously reducing the amount of memory and time required for final data processing.

**Figure 3**
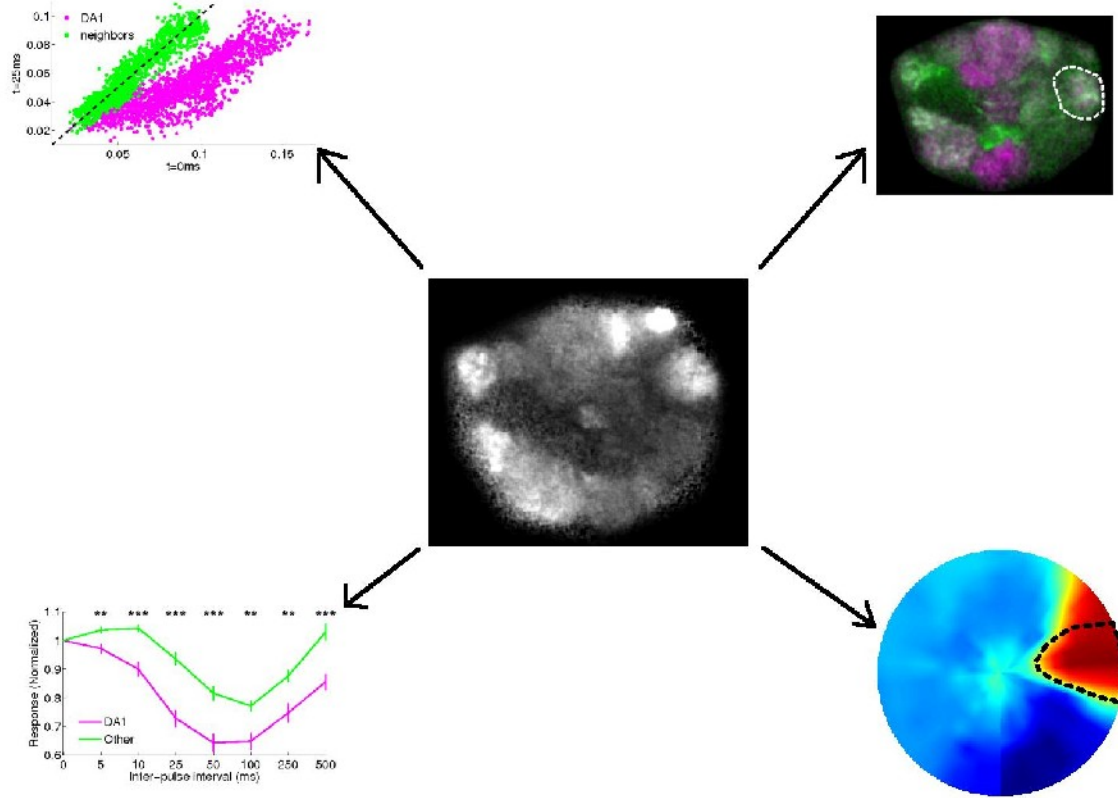


**Figure 3. Data organization enables rapid and flexible processing.** Once data is pre-processed and metatagged, represented in center image, algorithms can be written to rapidly generate new visualizations and test hypotheses about relationships between elements, as represented in the surrounding images.

**Figure 4**



**Figure 4. Choosing a metric to quantify an effect. A)** Responses of the antennal lobe to ipsilateral and contralateral nerve stimulation, colored in green and magenta, respectively. Unlike other glomeruli, DA1, demarcated with a dashed white line, exhibits different spatial response profiles for the two stimuli. **B)** Spatial correlation between the responses to the two stimuli, quantified and color-coded for each glomerulus. Warmer regions represent glomeruli with higher spatial correlation between the two responses. DA1 was expected to show a very low correlation, but did not in actuality. **C)** Difference in spatial extent between ipsilateral and contralateral responses. DA1 and its dorsal neighbor, DL3, show the largest difference, as expected. **D)** This metric was subsequently used in multiple ways to quantify the difference between DA1 and other glomeruli.

# Appendix 4

## Evolution of the Interpretation of Data

Below is a sequence of attempts at organizing the data into a story. The final product is found in Chapter 2.

### October 1, 2007    Cold Spring Harbor poster abstract

The antennal lobe (AL) is a structure that processes odors. It is subdivided into glomeruli, an array of modules tuned to different olfactory features. The receptor identity and odor tuning of its inputs has been characterized. We present a complementary approach to map the functional variation intrinsic to the AL by measuring its responses to uniform, global stimulation. We find spatial gradients in glomerular response properties measured using the calcium indicator G-CaMP 1.6. This variation may reflect the unique statistical and behavioral contingencies of the stimuli that different glomeruli are tuned to.

### October 1, 2008    Preliminary outline for manuscript

Spatiotemporal integration of activation in the AL

1. Rationale for experiments
    A. Electrophysiology reveals input-output nonlinearities in PN response
    B. Imaging shows relatively faithful propagation of olfactory information
    C. Electrical stimulation in isolated brain
            1) Reveals inhomogeneities in spatial Ca response at high resolution
            2) Understand response dependency on
                    i. Strength and location of input
                    ii. Temporal patterning of input
                    iii. Pharmacological perturbation
                    iv. Genetic manipulation of PN properties
2. Input and output have different excitation signatures
    A. temporal difference
            1) ORN Ca increases gradually with stimulation
            2) PN Ca increases abruptly then plateaus
                    a. not due to saturation
                            i. inhibition allow further rise
                            ii. different glomeruli reach different plateaus
    B. Spatial difference
            1) Ipsilateral vs. contralateral stimulation
                    a. ORN terminals segregate by side
                            i. gradient of territory occupied by terminals

112

        b. PN distribution is heterogeneous but stereotyped

              i. gradient of relative (ipsi vs. contra) response magnitude

              ii. exception - 2 dorsolateral glomeruli

      2) Variation of stimulation voltage

          a. varying recruitment of fibers

              i. individual glomeruli retain stereotyped response

              ii. different glomeruli become nonresponsive at different thresholds

              iii. graded decrease of response(?)

              iv. ORN properties?

C. Summation properties

      a. sublinear vs. linear integration of multiple inputs

          i. ORN vs. PN

      b. temporal window of input integration

          i. subthreshold inputs

          ii. suprathreshold inputs

      c. effects of

          i. inhibition blockers

          ii. increasing PN excitability

          iii. camkII activators/inhibitors

          iv. blockers of PN neurotransmission

D. relation to sensory system features

      a. model

**March 15, 2009    Keystone poster abstract**

The antennal lobe (AL) is a structure that processes odors. It is functionally partitioned into glomeruli, each of whose inputs detect unique chemical features. How specialized is the circuitry of each glomerulus to operate on its inputs? We study this at high resolution by using global and uniform stimuli and measurements. We find that glomeruli tuned to detect food and sex odors respond differently. The prominent pheromone processor DA1 highlights this specialization. It minimally interacts with other glomeruli, instead capturing spatiotemporal features of its input. Our results show how homologous circuits reflect the unique contingencies of their inputs.